INFRARED REMOTE SENSING OF VOLATILE COMPONENTS ON THE EARTH AND MOON

By

Casey I. Honniball

a dissertation submitted in partial fulfillment of the requirements for the degree of

DOCTOR OF PHILOSOPHY

in

EARTH AND PLANETARY SCIENCE

at the

UNIVERSITY OF HAWAIʻI AT MĀNOA

October 2019

Dissertation Committee

Paul G. Lucey, Chair

Robert Wright

David Trang

Hope Ishii

Jonathan Williams

Keywords: Volatiles, Infrared, Remote Sensing, Hyperspectral, Volcanism, Moon, Lunar surface

ACKNOWLEDGEMENTS

Throughout my academic life I have struggled with dyslexia. Many people that knew me growing up, including my parents, thought I would run away and join the circus. However, despite my struggles in school, my parents Bruce and Karen Honniball have always stood by my side encouraging and helping me better myself whether it be in the performing arts or in school. The support and love they have provided throughout my life has made me who I am today and I could not have made it this far in school or life without them.

Being a graduate student is hard on its own but adding on top of that being away from family and friends can make life as a graduate student even harder mentally. Without Tiana Hernandez and Zachary Lakey, my graduate career would be vastly different. Tiana would become my first true and best friend in Hawai‘i, coming over to study or hangout together, she helped me through lonely and stressful times. Halfway through my graduate career I met Zac who would become my husband. He has shown me nothing but support and love. He is always encouraging me and supporting me. He has been my rock during the last half of my graduate career.

Above all, I would like to thank my graduate advisors, Dr. Paul G. Lucey and Dr. Robert Wright. Dr. Wright took a chance on me and accepted my application into graduate school. If it were not for him I would not be where I am today. He has shown support in all of my decisions throughout graduate school, form chancing degrees twice, beginning work that was outside the original project I was accepted into graduate school for, and in changing graduate advisors. I will be forever grateful to Dr. Wright. As for Dr. Paul G. Lucey, he helped me find my passion in science. From day one we worked well together tinkering in the lab or covering complex interferometry techniques. He has shown patients and support throughout my graduate career and has helped me shoot for the stars. I will forever be thankful to have met and worked with such a talented and caring advisor. He has become a lifelong friend to me.

I would like to also acknowledge: Qualifying Committee – Paul G. Lucey, Robert Wright, Paul Wessel, Comprehensive Committee – Paul G. Lucey, Robert Wright, Paul Wessel, Patricia Fryer, Jeff Gillis-Davis, Dissertation Committee – Paul G. Lucey (Chair), Robert Wright, Hope Ishii, David Trang, Jonathan Williams (University representative), Instructors – Kathleen Ruttenberg, Patricia Fryer, Scott Rowland, Jeff Taylor, Jasper Konter, Gary Huss, Eric Gaidos,

Paul Wessel, Yuqing Wang, Paul Lucey, Michael Garcia, Collaborators – Alex Parker, Andrew Helton, Ben Bussey, Bobby Bus, Morgen Cable. Josh Cahill, Driss Takir, Shuai Li, Bill Farrell, Ben Greenhagen, John Rayner, Karl Hibbitts, Heather Kaluna, Al Khayat, Mike Connelley, Noah Petro, Andy Rivkin, SERVII RISE - Tim Glotch, Jacob Bleacher, Kelsey Young, Deanne Rogers, Spectrum – Byron Wolfe, Daniel Piquero, Ed Knobbe, Undergraduate – Chris Walker, Craig Kulesa, Ab Young, Brandon Swift, Jenna Kloostermann, Andrew Lincowski, Kristina Davis, Jose Sillas, Gary Varner, Kurtis Nishimura, Matt Andrew, Department of Geology and Geophysics/Earth Sciences, Hawai‘i Institute of Geophysics and Planetology, Technical Support: Eric Pilger, Ethan Kastner, Harold Garbeil, Lance Yoneshige, Mark Wood, HIGP and GG office support, The various graduate students and post-docs within the University of Hawai‘i.

Lastly I would like to acknowledge my funding sources: “Detection of the water molecule on asteroids and the Moon using SOFIA" Universities Space Research Association, P. Lucey PI, "Ground-based Observations of the Moon at 3um" NASA Solar System Observations Program, Heather Kaluna PI, "Miniaturized infrared detector for atmospheric species" NASA EPSCoR, Robert Wright PI.

ABSTRACT

This dissertation is focused on using infrared remote sensing to study volatiles on the Earth and Moon, including a strong hardware development component. The first project was aimed at developing light weight spectrometer for small satellites. In that work we build a 3 – 5 μm imaging interferometer, calibrated it, used it to collected data of the lava lake at Kilauea volcano, and analyzed a portion of the data with a radiative transfer model. We find that for high temperature targets, measurements in the 3 – 5 μm region can be acquired with high signal-to-noise ratios.

The second two projects involve the study of water on the Moon using infrared astronomy. We investigate diurnal variations of hydration that was first detected on the Moon using orbiting infrared spectrometers. Analysis of spacecraft data, however, result in diametrically opposed results. Using new observations of the Moon with the NASA IRTF SpEX instrument we are able to overcome the fundamental limitations in the orbital data allowing us to resolve the diurnal variation controversies. Our improved data showed that the variation in hydration is real. The second astronomical project addresses a second fundamental problem. The spacecraft observations cannot tell the difference between the presence of water or hydroxyl. This has fundamental consequences for the behavior of volatiles on the Moon. However, we developed a new approach to detect the actual water molecule on the Moon using observations at 6 μm, based on how geologists detect H_2O in samples in the lab using infrared spectroscopy. Observations at 6 μm are only possible from an airborne infrared observatory, we were granted time on the Stratospheric Observatory For Infrared Astronomy (SOFIA) to collect data of the Moon. Using data from SOFIA we report the first direct detection of the water molecule on the illuminated lunar surface.

TABLE OF CONTENTS

Acknowledgements iii
Abstract v
List of Tables viii
List of Figures ix
List of Abbreviations and Variables xiv

CHAPTER 1: SPECTROSCOPIC REMOTE SENSING OF VOLATIELS 16
1.1 Fundamentals of Spectroscopy 16
1.2 Importance of Volatiles in the Solar System 17
1.2.1 Carbon Dioxide 17
1.2.2 Molecular Water 18
1.3 Dissertation Goals and Structure 18

CHAPTER 2: EVALUATING THE SPECTRO-RADIOMETRIC PERFORMANCE OF AN UNCOOLED MID-WAVE INFRARED HYPERSPECTRAL INTERFEROMETER USING A MICROBOLOMETER ARRAY DETECTOR 20
Abstract 20
2.1 Introduction 21
2.2 Design and Data Processing of the MIDAS MWIR Hyperspectral Imager 23
2.2.1 Concepts of the Spatial Interferometer 24
2.2.2 Collection of Data and Processing 26
2.2.3 The MIDAS Instrument 26
2.3 Instrument Characterization and Spectro-Radiometric Performance 29
2.3.1 Camera Stability 29
2.3.2 Wavelength calibration 30
2.3.3 Spectral Response of the Individual Cameras 30
2.3.4 Sensitivity Tests 32
2.4 Volcanic Gas Observations Using MIDAS 34
2.4.1 In Field Radiance Calibration 34
2.4.2 Radiative Transfer Modeling 35
2.5 Results of Volcanic Gas Measurements 37
2.6 Conclusions 39
Acknowledgements 40

CHAPTER 3. GROUND-BASED OBSERVATIONS OF LUNAR SURFACE WATER DIURNAL VARIATIONS 41
Abstract 41

3.1 Introduction 43
3.2 Background 45
3.3 Contribution of Groundbased Astronomical Observations 48
3.4 Lunar Observations with the IRTF 49
3.5 Data reduction 51
3.6 Removal of Thermal Emission 55
3.7 Estimating the Abundance of Total Water 59
3.8 Results 63
3.9 Discussion 68
3.10 Conclusions 72

CHAPTER 4: DETECTION OF MOLECULAR WATER ON THE ILLUMINATED MOON WITH SOFIA 74
Abstract 74
4.1 Introduction 75
4.2 Background 76
4.3 6 μm Observations in Samples and on Planetary Bodies 80
4.4 Lunar Observations with SOFIA FORCAST 82
4.5 Data Processing 84
4.6 Methods 85
4.6.1 Removal of Instrument Artifact 85
4.7 Detection of a 6 μm Emission Band 88
4.7.1 Assigning 6 μm Emission to H_2O 89
4.8 Deriving Abundances 91
4.8.1 H_2O Abundance with Latitude 94
4.9 Discussion 95
4.9.1 Estimating Surface Temperature 95
4.9.2 Estimating the Abundance of H_2O Available to Migrate 97
4.10 Conclusions 99

CHAPTER 5: CONCLUSIONS AND FUTURE WORK 100
5.1 Summary 100
5.2 Future work 101
5.2.1 Determining the use of MIDAS for Lunar Field Work 101
5.2.2 Connecting IRTF and SOFIA Observations 101

APPENDIX 103
REFERENCES 122

LIST OF TABLES

Table 2.1 Detector specifications 28

Table 3.1 List of data acquired. 51

Table 4.1: 6 μm band properties for the Moon, meteorites, MORB and literature values. See Appendix for full data. 91

LIST OF FIGURES

Figure 1.1: Example of emission and absorption spectra. [Evans R., 2015] 16

Figure 2.1: Spectral radiance (units: W m^{-2} sr^{-1} μm^{-1}) reflected from a surface with unit reflectance (orange), emitted from a surface with unit emissivity at 300K (green), emitted from a surface with unit emissivity at 1400K (black). Atmospheric absorption is not included. 22

Figure 2.2: Schematic of a triangular Sagnac interferometer and ray trace of the two common path beams. The beams are separated for clarity. 25

Figure 2.3: Collection of hyperspectral data by scanning a scene, stacking the frames and "drilling" down through the cube to extract an interferogram for each element in the array. Performing Fourier Transform techniques on the interferogram derives a calibrated spectral radiance spectrum for each scene element. 27

Figure 2.4: a) The packaged MIDAS instrument with the uncooled microbolometer. b) The triangular Sagnac interferometer. 28

Figure 2.5 Camera DN and temperature stability over a period of four hours. a) The INO camera reaches stabilization around an hour after turn on. b) IRCamera DN stabilized 30 minutes after cooling began, there is a slight drift of DN for the duration of the test. c) IRCamera focal plane temperature is directly linked to DN stability. 29

Figure 2.6 Spectral response of the MWIR INO microbolometer (a) and the IRCamera InSb photon detector (b). The dashed lines are raw response of the camera to the output by the monochromator. Solid lines are the raw response divided by the MWIR calibration curve. The anomaly at 4.2 μm (blue region) in the calibrated spectral response curve is due to varying path length and varying CO_2 concentration in the room. The spectral response curve was pieced together from measurements made using two gratings (blazed at 3.5 μm and 7 μm). The transition between the two sets of measurements is shown by the red bar. 31

Figure 2.7 SNR, NESR and NEdT measurements of the MIDAS (INO Microbolometer) and CIDAS (InSb IRCamera) instruments at 50 and 100 cm^{-1}. 33

Figure 2.8 The MIDAS instrument monitoring the late Halemaʻumaʻu lava lake. 34

Figure 2.9: Brightness temperature map calculated from the spectral radiance map of the Halemaʻumaʻu lava lake at 4.0 μm. 35

Figure 2.10 Viewing geometry of MIDAS and the radiance through the volcanic gas plume. 37

Figure 2.11 Spectral radiance image at 4.58 μm of the Halemaʻumaʻu lava lake. Variations on the lava lake are consistent with temperature differences seen in Figure 8. The black fractures are due to saturation. 37

Figure 2.12: Transmission spectrum acquired by MIDAS of the Halemaʻumaʻu lava lake (black). Modeled transmission spectrum (red) with CO_2 abundance of 2773 ± 167 ppm. 38

Figure 2.13: Map of CO_2 emanating from the Halemaʻumaʻu lava lake on July 25, 2017. Subtle variations can be seen in the image with some areas showing locations of CO_2 plumes. 39

Figure 3.1: Deep Impact observations of the Moon of two separate days where the local time on the Moon advanced by 7.2 hours. The color represents the strength of the 2.8 μm band. [Sunshine et al., 2009] 44

Figure 3.2: Spectrum of the Moon showing thermal (blue) and reflected radiance (cyan). Reflected radiance dominates at shorter wavelengths while thermal radiance dominates at longer wavelengths. 45

Figure 3.3: Bottom: Thermally corrected M^3 data archived at the Planetary Data System. Top: same data corrected by Bandfield et al. 2018. It is not known if the Bandfield et al. correction would perform properly at longer wavelengths. 46

Figure 3.4: Demonstration of the importance of wavelengths beyond 3 μm. Data is of the Moon acquired by the IRTF at a latitude of 11°S and a lunar local time of ~08:00. The black spectrum is the data with the correct thermal model removed while the others are the same data with models ± 2, 5, and 10 K from the proper model. a) shows the data cut off at 3 μm similar to M^3 while b) shows wavelengths out to 4.2 μm. In a, it is difficult to know which model is correct as the different 3 μm band strengths are reasonable measurements. In b however, it is clear when you apply incorrect thermal models to the data, the longer wavelengths no longer spectrally make sense for the lunar surface. 47

Figure 3.5: Comparison of M3, IRTF, Deep Impact and Cassini spectral range (a) and spatial resolution (b). The IRTF provides both the spectral coverage and spatial resolution needed to observe diurnal variations on the Moon. 48

Figure 3.6: Locations of lunar observations for this project. Each line indicated were data was collected. All were observed on two to three consecutive nights to capture any variation in the 3 μm absorption band with temperature and time of day. 50

Figure 3.7: Map of high southern latitudes from ~65° to the pole using SpEX as an imaging spectrometer. 50

Figure 3.9: The bright stripes are the 7 crossed dispersed orders of SpEX. Stray light can be seen between the orders when the contrast of the image is enhanced (left). The red stripes on the right indicate where stray light was moved into each order. 52

Figure 3.8: The 7 overlapping crossed dispersed orders of SpEX. 52

Figure 3.10: Example of the stray light correction in the opaque water region of the atmosphere from 2.5 to ~2.8 μm. The black spectrum sits on a pedestal of stray light causing the band to

appear to have signal. Data after stray light removal is shown in red and now has a mean value of zero as expected in a region that is opaque. 53

Figure 3.11: Processing steps to remove background sky emissions and telluric absorptions. 54

Figure 3.12: Removal of red slope continuum. 56

Figure 3.13: Longer wavelengths constrain which thermal model is selected. 58

Figure 3.14: On left is the result of thermal removal with a continuum removed and normalized. On right is multiple thermal models removed that are ± 5 and 10 K from the optimum thermal model. 59

Figure 3.15: Conversion of reflectance spectra to single scattering albedo Also shown are the different thermal models (red and blue). The effect of incorrect thermal model selection does not greatly affect the shape or strength of the 3 μm band. The small effect incorrect models have is added uncertainty in the point to point scatter. 60

Figure 3.16: Conversion of single scattering albedo to ESPAT with the different thermal models (red and blue). 61

Figure 3.18: Empirical relationship between band depth and absolute content H_2O in water-bearing terrestrial glasses (Li, 2017). 62

Figure 3.17: a) Empirical relationship between ESPAT and absolute content H2O in water-bearing terrestrial glasses (Li, 2017) at wavelengths 2.86 μm. b) The same relationship except at 2.95 μm. We use the relationship for 2.95 μm because from the ground the 2.86 μm region is opaque. 62

Figure 3.19: Normalized reflectance spectra after thermal radiation removal. The bottom spectrum shows a step down from 2.5 to 2.9 μm indicating the presence of total water. The top is an example of a flat spectrum with no total water. The gray bands are regions where atmospheric species absorb and cause low signal regions. A pyroxene band can also be seen at 2 μm in the top spectrum. 63

Figure 3.20: “Wet” and “dry” spectra from January 18th, 2019 observing run. The spectra show variations in the 2 μm pyroxene band along with variations in strength and shape of the 3 μm band. 64

Figure 3.21: Chords plotted as lunar time of day vs. Latitude for both ESPAT and band depth methods. Symbol size is proportional to the abundance of total water. The anomalous high abundance at ~0° latitude and ~0830 lunar time of day is believed to be high total water abundances at and around Copernicus crater. 65

Figure 3.22: Total water abundance in ppm H_2O plotted against latitude (a) and time of day (b) for the pole to pole observations. 66

Figure 3.23: Chords plotted as lunar time of day vs. latitude using the ESPAT values. Point size represents abundance with larger points being more abundant..... 67

Figure 3.24: Diurnal signature in FUV LAMP data for mare and highland regions. The diurnal signal is attributed to H_2O if it behaves like water ice in the FUV. The diurnal signal is seen near local noon. Hendrix et al., 2019. 71

Figure 4.1: Comparison of various physical states of water at 3 μm. Major spectral differences between the states are observed beyond 3 μm. From Hibbitts et al., 2011..... 78

Figure 4.2: FTIR spectra of hydrous rhyolite glasses showing the multiple OH and H_2O spectral bands. The 6 μm band of interest for this study is at 1630 cm-1 and is shown in the inset. [McIntosh et al., 2017]..... 79

Figure 4.3: Reflectance spectra measured in the lab of (a) Apollo samples (b) meteorites [Takir et al., 2019] and emission spectra of (c) Mars [Bandfield et al., 2003] and (d) asteroids observed by SPITZER where red spectra show no 6 μm band and blue spectra show a 6 μm band [Marchis et al., 2012]. All plots exhibit a 6 μm absorption or emission band with varying shape and strength. The presence of the band indicates adsorbed or bound H_2O..... 81

Figure 4.4: Atmospheric transmission at Maunakea observatory (blue), SOFIA (green), and from a stratospheric balloon (red)..... 82

Figure 4.5: SOFIA FPI guider images showing accurate location pinpointing of the three targets. Prior to the observing run it was not clear if the guider cameras would be able to view the Moon. The FPI images demonstrate feasibility of locating geologic targets on the scale of a few km. .. 83

Figure 4.6: SOFIA processing pipeline. [SOFIA Guest Observer Handbook for FORCAST Data Products] 84

Figure 4.7: a.) Spectral images from SOFIA of the Clavius region and surrounding area. Oscillation superimposed on this image is not a lunar feature. The artifact on the top right is due to some contamination on the window of FORCAST. b.) Guider image of the Clavius region and the location of the slit..... 86

Figure 4.8: Spectra of Sulpicus Gallus (top) and Goldschmidt (bottom) showing the sharp and round spectral shapes, respectively. Assuming the spectral shape indicates the presence of water or lack of, Sulpicius Gallus shows no H_2O while Goldschmidt shows theres water present. Water bearing glasses (red) with known abundance of H_2O agree with Sulpicius Gallus not containing H_2O. 87

Figure 4.9: a.) Flux spectrum of Sulpicius Gallus showing the oscillation and continuum to be removed in red. b.) continuum removed spectrum. c.) Sulpicius Gallus oscillation image. 87

Figure 4.10: a.) Oscillation-removed flux special image of Clavius region. b.) Clavius region with continuum removed. A bright band is seen around 6 μm in the continuum-removed spectral image of Clavius indicating the presence of H_2O. 88

Figure 4.11: a.) Oscillation removed radiance spectrum of Clavius region. b.) Continuum removed radiance showing a strong 6 μm emission band indicating the presence of H_2O. 89

Figure 4.13: a) Band centers of the lunar 6 μm (red), meteorite (black), and MORB (blue) bands. b) Distribution of H_2O band centers for crystalline hydrates from Falk 1984. 90

Figure 4.12: Lunar 6 μm emission band observed by SOFIA (red) compared to other 6 μm bands seen on asteroid Elektra (green), meteorites Mil15328 and Murchison (black) [Takir et al., 2019], and in water bearing glass beads (blue). 90

Figure 4.14: Water bearing glass beads showing a 3 and 6 μm absorption (a) used to derive a relationship between band depth (b) and H_2O content (c). 92

Figure 4.16: One of the six frames of Clavius showing the lunar 6 μm band depth and abundance versus latitude. No clear trend with latitude is observed. 94

Figure 4.18: Brightness temperature from one observation of the Clavius region. The variation in brightness temperature corresponds to locations of more or less illumination. The error is found by converting the variance reported by the FORCAST processing, converting it to radiance and brightness temperature and taking the square root. 96

Figure 4.19: Fraction of a monolayer available to cover the lunar surface at specific temperatures for southern latitudes. Temperature was calculated based on Hurley et al., 2015. (Personal communication, Thomas Orlando and Brant Jones] 98

LIST OF ABBREVIATIONS AND VARIABLES

Abbreviation/Symbols	Definition
A_{mono}	Area of a water molecule
ATRAN	Atmospheric TRANsmission
APL	Applied Physics Laboratory
b	6 μm band depth in reflectance
B_T	Thermal Radiance
C	Continuum
CH_4	Methane
CIDAS	Cooled Infrared Detector of Atmospheric Species
cm^{-1}	Wavenumber
CO_2	Carbon Dioxide
CRISM	Compact Reconnaissance Imaging Spectrometer for Mars
DDT	Director's Discretionary Time
DEC	Declination
d_{H_2O}	Diameter of a water molecule
DN	Digital Number
e	Emissivity
E	Emission
EO-1	Earth Orbitor-1
ESPAT	Effective Single Particle Absorption Thickness
EVA	Extra Vehicular Activity
F	Flux
FFT	Fast Fourier Transform
FTIR	Fourier Transform InfraRed
FORCAST	Faint Object infraRed CAmera for the SOFIA Telescope
FOV	Field Of View
FUV	Far Ultra-Violet
H	Hydrogen

H_2O	Molecular Water
HITRAN	High TRANsmission
HSI	HyperSpectral Imaging
i	Incidence angle
InSb	Indium Antimonide
IRTF	InfraRed Telescope Facility
JHU	Johns Hopkins University
JPL	Jet Propulsion Laboratory
Jy	Jansky
LabSPEC	Laboratory for Spectroscopy under Planetary Environmental Conditions
LADEE	Lunar Atmosphere and Dust Environment Explorer
LAMP	Lyman Alpha Mapping Project
LN_2	Liquid Nitrogen
LRO	Lunar Reconnaissance Orbiter
L_{solar}	Solar Radiance
LWIR	Long-Wave Infrared
M^3	Moon Mineralogy Mapper
M_{H_2O}	Molar Mass of Water
MI	Multiband Imager
MIDAS	Miniaturized Infrared Detector of Atmospheric Species
M_{mono}	Monolayer of Water
MORB	Mid-Ocean Ridge Basalt
MRO	Mars Reconnaissance Orbiter
MWIR	Mid-Wave Infrared
N_0	Avogadro's number
N_2O	Nitrous Oxide
NEdT	Noise Equivalent differential Temperature
NESR	Noise Equivalent Spectral Radiance
NIST	National Institute of Standards and Technology

NMS	Neutral Mass Spectrometer
OH	Hydroxyl
OH + H_2O	Total Water
OSIRIS-REX	Origins, Spectral Interpretation, Resource Identification, Security-Regolith Explorer
OTES	OSIRIS-REx Thermal Emission Spectrometer
PSRs	Permanently Shadowed Regions (
ppm	Parts Per Million
RA	Right Ascension
R_{band}	Mean absorption peak from 6.0 to 6.1 µm
R_{con}	Reflectance Continuum
R_{cont}	Mean continuum from 5.2 to 5.3 µm
RELAB	Reflectance Experiment LABoratory
RISE2	Remote In Situ and Synchrotron Studies for Science and Exploration 2
R_λ	Radiance
R_{model}	Modeled Lunar Radiance
$R_{n1.7}$	Normalize lunar spectra at 1.7 µm
R_{ref}	Reference continuum at 6 µm from Apollo
SNR	Signal-to-Noise Ratio
SO_2	Sulfur Dioxide
SOFIA	Stratospheric Observatory For Infrared Astronomy
SSA (w)	Single Scattering Albedo
T	Kinetic Temperature
TCS	Telescope Control System
TES	Thermal Emission Spectrometer
T_λ	Thermal Radiance
T_{ss}	Temperature of the sub-solar point
UTC	Coordinated Universal Time
VOx	Vanadium Oxide

wt.%	Weight Percent
x	Band Depth
X	Metal Cation
Y	Abundance of H_2O in ppm
“	arcsecond
γ	Thermal Excess
$\gamma_{measured}$	Measured lunar thermal excess
γ_{model}	Modeled lunar thermal excess
λ	Wavelength
μm	Micron

CHAPTER 1: SPECTROSCOPIC REMOTE SENSING OF VOLATIELS

For centuries humans have used sensors, whether it be the human eye, a camera, or an instrument designed for a specific use, to study the Earth, the Solar System, and the Universe. This act of deriving information about an object from a distance is termed "remote sensing" [Campbell and Wynne, 2011]. Spectroscopy, the study of the interaction between matter and electromagnetic radiation by splitting the radiation into its constituent wavelengths, can be done via remote sensing. Spectroscopic remote sensing can provide information regarding an object's intrinsic properties, like composition and abundance of molecules. One application for spectroscopic remote sensing is the study of molecular compounds that easily vaporize. These compounds are referred to as "volatiles". This dissertation focuses on the spectroscopic remote sensing of volatile species on both the Earth and Moon.

1.1 Fundamentals of Spectroscopy

Objects are made up of molecules, which are in turn made of elements, which are made of atoms, which are made of electrons, protons, and neutrons. Electrons reside close to an atom's nucleus at different energy levels. When electromagnetic radiation, photons of specific wavelength and energy, interacts with an atom, the energy of the photon can cause an electron to be excited and "jump up" to a higher energy level absorbing the photon in the process. The reverse process, emission, is also possible where the electron is de-excited and "drops down" to a lower energy level emitting a photon at a specific energy. The emission and absorption of photons depends on

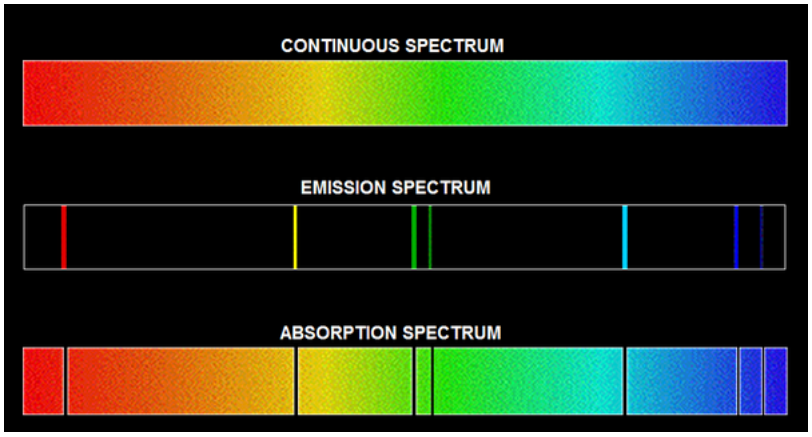

Figure 1.1: Example of emission and absorption spectra. [Evans R., 2015]

the chemical structure of atoms, and each atom has its own unique structure and therefore, its own unique "finger print", or spectrum. The release of a photon results in an emission spectrum while the inverse is a reflectance spectrum, also referred to as an absorption spectrum (Figure 1.1). The emission and absorption features occur at specific wavelengths depending on the chemical composition of the object.

The spectrum of an object can be measured by collecting the photons emitted and reflected by the object. Inspection of the absorption and emission features inform us about the composition of the object. The strength of the spectral features also provides information about the abundance of molecules present. The measurement of a spectrum can be done via remote sensing allowing us to examine the chemical composition of distant objects. This dissertation focuses on spectroscopic remote sensing of the Earth and Moon.

1.2 Importance of Volatiles in the Solar System

There are many volatile compounds that exist in the Solar System; however, for this dissertation we focus on two, carbon dioxide (CO_2) and molecular water (H_2O). Both of these volatiles are naturally occurring on Earth and possibly also on the Moon. Understanding the presence and concentrations of these volatiles inform us about on-going interior and surficial processes and the formation and evolution of a planetary body.

1.2.1 Carbon Dioxide

Carbon dioxide is a naturally-occurring volatile on Earth. It occurs in the atmosphere, hot springs, geysers, carbonate rocks, volcanoes, and because it is soluble in water, it occurs in groundwater, rivers, lakes, ice caps, glaciers, and sea water. Carbon dioxide is a colorless gas that is denser than air with a centrosymmetric molecular structure. In the infrared region, CO_2 exhibits spectral features at 2.65 – 2.85 μm, an antisymmetric stretching mode at 4.257 μm, and bending modes at 15 μm. In Chapter 2 of this dissertation, we focus on detecting CO_2 in volcanic gas plumes using the 4.257 μm antisymmetric stretching spectral feature.

Monitoring CO_2 outgassed by volcanoes is important for possible predictions of pending volcanic hazards and eruptions. CO_2 is one of the first gases to exsolve from ascending magma at depths of 21 – 24 km [Bruno, 2001]. It has been shown at Mt. Etna in Sicily, Italy [Bruno, 2001]

and Redoubt Volcano in Alaska [Werner et al., 2012] that elevated CO_2 emissions precede increased volcanic activity or an eruption. Chapter 2 does not focus on predicting a pending volcanic eruption, but instead focuses on detecting and quantifying volcanic CO_2 with an instrument that could potentially monitor CO_2 emissions from a small satellite platform.

1.2.2 Molecular Water

Molecular water is the most abundant substance on the Earth and is colorless and tasteless. It is fundamental to life on Earth and the sustainability of life in space and on other planets. On Earth, it can be found naturally in all three phases of matter, solid, liquid, and gas. It has a "bent" molecular structure, which exhibits spectral features at several wavelengths in the infrared. This dissertation, in Chapters 3 and 4, focuses on detecting water at 3 and 6 μm on the lunar surface. The Moon does not have bodies of water like Earth, but may have H_2O adsorbed onto lunar grains. The presence of water on the Moon could aid future exploration and long term sustainability of a lunar base.

1.3 Dissertation Goals and Structure

An overarching goal of this dissertation is to evaluate the use of wavelengths typically not used for remote sensing. In Chapter 2 we evaluate the use of a compact hyperspectral imager operating in the mid-wave infrared (MWIR) from 3 to 5 μm. This spectral region is typically not used in remote sensing on the Earth because of the low signal availability due to low energy at ambient temperatures. In this chapter, we look at overcoming this issue by using an imaging interferometer and by observing high temperature phenomena. We present the design and characteristics of the instrument and benchmark it against a similar instrument of the same design used as a standard. Results of field tests will also be reported along with radiative transfer modeling to derive abundances of CO_2. The goals of this project are to demonstrate that a compact instrument capable of small satellite platforms can provide high signal-to-noise ratios in the MWIR for use of monitoring and detecting high temperature targets.

Chapters 3 and 4 demonstrate the use of wavelengths beyond 3 μm to detect and characterize hydration signatures on the lunar surface. In Chapter 3, we use a groundbased telescope to acquire data of the Moon from 1.6 μm out to 4.2 μm. The wavelengths beyond 3 μm

allow for accurate thermal modeling and removal of thermal emission. With thermally corrected data, we address conflicting views of the 3 μm hydration feature and its variability on the lunar surface. The goals of this project are to determine the true nature of the 3 μm hydration feature and provide better estimates of the abundance of hydration on the Moon.

In Chapter 4 we extend out from 3 μm to 6 μm to look for H_2O on the illuminated lunar surface using new wavelengths, a new data set, and new techniques for remote sensing. We report observations of the Moon at 6 μm and the first direct detection of molecular water on the illuminated Moon. The goals of this project are to demonstrate the utility of 6 μm observations to detect and quantify the abundance of water on the Moon. We describe the 6 μm observations and the new technique for deriving abundances.

Chapter 5 summarizes our findings from Chapters 2 through 4 and presents future work for each chapter.

CHAPTER 2: EVALUATING THE SPECTRO-RADIOMETRIC PERFORMANCE OF AN UNCOOLED MID-WAVE INFRARED HYPERSPECTRAL INTERFEROMETER USING A MICROBOLOMETER ARRAY DETECTOR

Abstract

Improved technology and emerging interferometric techniques have allowed the use of uncooled microbolometers in the long-wave infrared (LWIR; 8 to 14 μm) for hyperspectral imaging. The mid-wave infrared (MWIR; 3 to 5 μm) presents several advantages with respect to the LWIR for Earth and planetary science. For example, important atmospheric trace gases on Earth such as CO_2 and CH_4 are not masked by other atmospheric constituents in the MWIR. However, hyperspectral imaging in the MWIR is more challenging at ambient Earth temperatures because less radiance is available to measure. We describe how hyperspectral images in the MWIR can be acquired with an instrument using an uncooled microbolometer married to a Sagnac interferometer. Standard characterization tests are used to benchmark the performance of the microbolometer instrument with a cryogenically cooled photon detector with the same optical design. At a spectral resolution of 100 cm^{-1} (17 bands between 3 and 5 μm), we measured a signal-to-noise ratio (SNR) of 100 at 303 K with the microbolometer instrument, and an SNR of 50 at 50 cm^{-1} (33 bands). Results from this work show that coupling microbolometers with interferometers allows for quality measurements with adequate SNR for high temperature science applications.

2.1 Introduction

Hyperspectral imaging (HSI) is defined as acquisition of image frames at several narrow contiguous spectral bands [Goetz et al., 1985; Rinker, 1990; Schott, 2007]. This imaging technique provides strong advantages when trying to disentangle compositions, as it acquires a complete spectrum of each element within a scene, i.e., for each pixel [Goetz et al., 1985]. HSI has a wide variety of uses in terrestrial and planetary remote sensing. It has been used for quantifying geological and atmospheric processes [van der Meer et al., 2012], mineral identification and vegetation mapping [Goetz et al., 1985], and as a reconnaissance tool for military applications and chemical identification [Kumar et al., 2015; Makki et al., 2017; Briottet et al., 2006].

Many HSI instruments have flown on aircrafts, including AVIRIS, SEBASS and TASI-600 [Vaughan et al., 2003; Pignatti et al., 2011; Thrope et al., 2013]. To date, Hyperion on EO-1 is the only infrared hyperspectral instrument flown in space for terrestrial remote sensing. However, many have been flown to other planets, i.e., TES on Mars Global Surveyor, Mini-TES on the Mars Exploration Rover, OTES on OSIRIS-REX, and CRISM on MRO. Just like its use for planetary remote sensing, the use of HSI is a viable option for terrestrial remote sensing [Barudcci et al., 2010] and is a growing field with increasing interest for military and civilian applications [Shukla and Kot, 2016; Rogalski, 2017].

The use of HSI on small satellites is a growing field because of the extensive scientific applications and also because of the lower launch costs and faster development times. However, small satellites have limitations on the size, weight, and power available to the instrument. Most infrared hyperspectral imagers use highly sensitive detectors, traditionally cooled to less than 100 K. All the instruments mentioned above use either cooled detectors or a Michelson interferometer that requires a moving mirror to create a spectrum. The use of moving parts, cryogenic liquids, or cryocoolers makes these instruments consume large amounts of power while also requiring large instrument footprints. To mitigate the power, size, and weight constraints of small satellites, researchers have begun investigating the use of uncooled microbolometer arrays coupled to static imaging interferometers to acquire HSI data [Barducci et al., 2010; Lucey and Wilcox, 2003; Lucey et al., 2008; Alain ,1994]. Instruments utilizing this type of coupling are attractive prospects for small satellites.

Recent improvements to microbolometer technology have led to more sensitive detectors allowing for their use in HSI instruments that mainly operate in the long-wave infrared (LWIR) from 8 to 14 µm. Lucey and Wilcox (2003) showed that integrating a static imaging interferometer with a microbolometer for LWIR HSI results in signal-to-noise ratios (SNR) of a few hundred. Following this work, it has been shown that such an instrument can acquire useful scientific data for mineral, chemical, and gas detection [Crites et al., 2012; Crites et al., 2014; Lucey et al., 2012; Wright et al., 2016; Gabrieli et al., 2016]. In this project, we investigate the use of a similar instrument for the detection of CO_2 in the mid-wave infrared (MWIR) from 3 to 5 µm.

Remote sensing in the MWIR is of interest due to the presence of greenhouse gases, such as CO_2 and CH_4, that exhibit strong absorptions that are not obstructed by other spectral features. Unlike the LWIR, the MWIR experiences challenges when conducting remote sensing observations. The main area of complication is the limited MWIR signal available to measure in for typical surface temperatures and solar illumination (Figure 2.1). For terrestrial remote sensing this is a major disadvantage for observations in the MWIR. Many targets of interest have temperatures similar to the Earth's ambient temperature in the range of 273 to 323 K. At these temperatures, the emitted signal in the MWIR is less than that available in the LWIR (Figure 2.1).

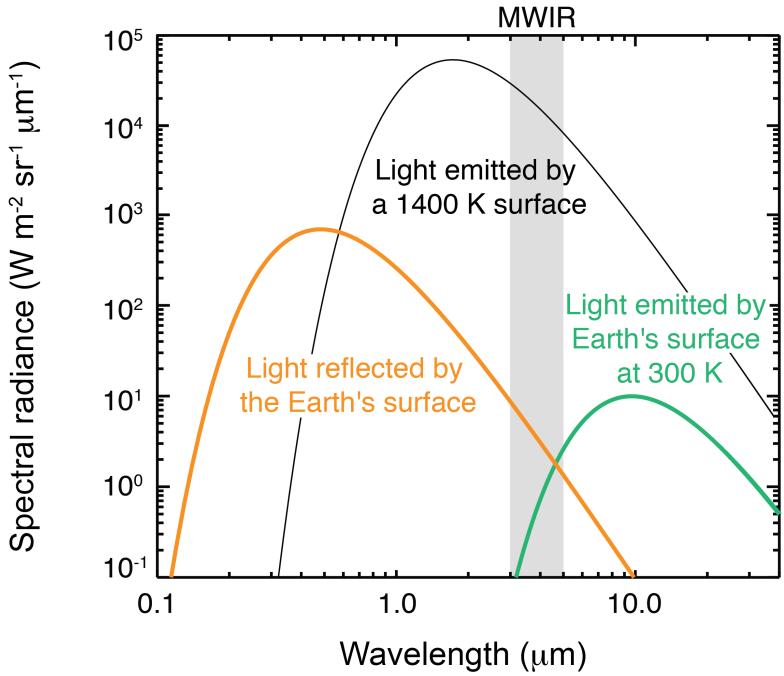

Figure 2.1: Spectral radiance (units: W m^{-2} sr^{-1} μm^{-1}) reflected from a surface with unit reflectance (orange), emitted from a surface with unit emissivity at 300K (green), emitted from a surface with unit emissivity at 1400K (black). Atmospheric absorption is not included.

For this reason, MWIR instruments are typically cooled to cryogenic temperatures between 40 and 110 K [Rogalski, 2002] to achieve high SNR from the ambient temperature targets. Operation of instruments at cryogenic temperatures, as mentioned above, causes instruments to have large footprints and consume more power.

A unique application for MWIR remote sensing is observation of high temperature phenomena, such as wildfires, lava flows, and lava lakes. There targets can reach temperatures of 700 to 1400 K [Wooster et al., 2003; Peale et al., 1979; Howell, 1997] increasing the amount of signal emitted (Figure 2.1) and, therefore, making MWIR remote sensing observations of such targets more attainable.

In this project, we developed a low mass, power efficient MWIR hyperspectral instrument that can be flown on small satellites to observe high temperature phenomena by using a static interferometer and an uncooled microbolometer detector array. We present the design, spectro-radiometric characterization of this instrument called the Miniaturized Infrared Detector of Atmospheric Species (MIDAS). We report the MIDAS instruments precision and benchmark its performance against a similar instrument with the same optical design but using a cooled detector array. We then evaluate the MIDAS instruments performance by measuring volcanic CO_2 emanating from a lava lake on Hawai‘i Island that was active until 2018 using the MIDAS instrument.

2.2 Design and Data Processing of the MIDAS MWIR Hyperspectral Imager

The MIDAS instrument includes an uncooled microbolometer detector coupled to a static Fourier transform imaging interferometer. These two fundamental components of the MIDAS instrument allow it to be compact, lightweight, and power conservative. Use of an uncooled microbolometer detector array is enabled by recent improvements in detector technology providing high pixel counts with sensitivities in the tens of mK [Rogalski, 2017; Kruse, 2002; Honniball et al., 2017]. As their name suggests, microbolometer arrays are extremely small bolometers arranged into a grid, and detectors almost universally use either amorphous silicon or vanadium oxide (VOx) bolometer technology [Kruse 2002]. Each individual bolometer (i.e., each pixel) absorbs incident radiation and converts it to an electrical signal. The typical application of microbolometer detectors is high resolution thermal imaging, but spectroscopy has somewhat different requirements. In

particular, a flat spectral response is desirable, but at minimum, the spectral response of detector must be known in order to judge its utility for a specific spectral application. Part of this project was to characterize the spectral response of the microbolometer.

2.2.1 Concepts of the Spatial Interferometer

The concept of using spatial interference patterns, i.e., an interferogram, for spectroscopy was introduced in 1979 by Caulfield and later demonstrated by Okamoto et al. (1984). Since then, several variants of spatial interferometer spectrometers have been produced, principally for remote sensing [Lucey and Wilcox, 2003; Lucey et al., 2008; Smith and Schemp, 1991; Lucey et al., 1993; Rafert et al., 1994; Smith and Hammer, 1996; Minnett and Seller, 2005; Horton, 1996]. Spatial interferometers, like the traditional Michelson interferometer use Fourier transform operations to convert raw data to a spectrum. Unlike the Michelson interferometer, however, spatial interferometers are designed to collect spatial characteristics of the imaged scene along with the spectral data [Schott, 2007].

There are several advantages to using an interferometer, such as multiplexing and throughput [Vaughan et al., 2003; Barducci et al., 2010; Griffiths and Haseth, 1986; Seller and Boreman, 2003]. The multiplex advantage arises from interferometers capability of measuring all spectral bands simultaneously [Alain, 1994; Griffiths and Haseth, 1986]. Interferometers also allow substantially more light into the system than dispersive spectrometers that require a slit [Alain, 1994; Griffiths and Haseth, 1986]. Both of these principles act to increase the amount of signal measured and therefore increase the sensitivity of a system employing an interferometer, though it should be noted that these advantages apply only when using read noise limited detectors like microbolometers. When using detectors where the SNR is dominated by photon statistics, these advantages are not present. However, an interferometer is an optimum choice when a microbolometer detector is required, for example for power consumption reasons.

For this project we chose to use the triangular Sagnac interferometer for the MIDAS instrument. The Sagnac interferometer is a two-beam common path spectrometer [Seller and Boreman, 2003]. When light enters the Sagnac interferometer, it first encounters a beamsplitter that splits the incident radiation into a transmitted and reflected beam which then traverse the interferometer in opposing directions, one clockwise and the other counterclockwise, controlled by two mirrors in a triangular configuration (Figure 2.2). The two beams recombine at the

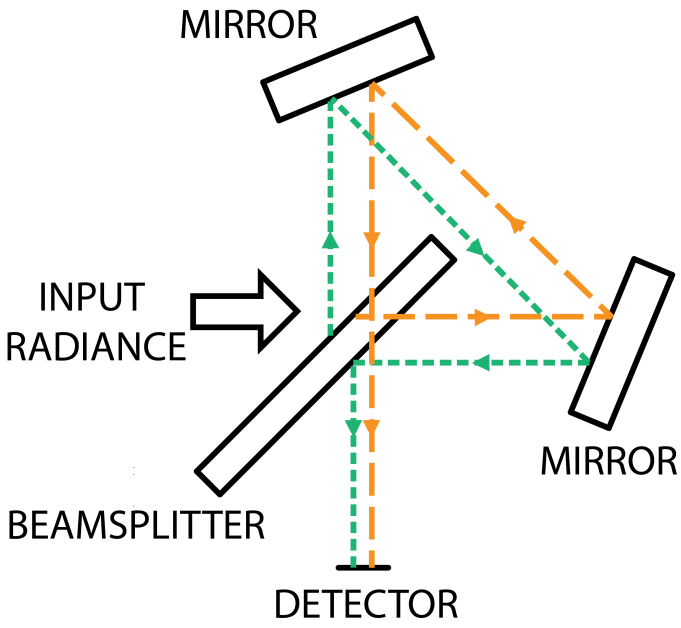

Figure 2.2: Schematic of a triangular Sagnac interferometer and ray trace of the two common path beams. The beams are separated for clarity.

beamsplitter on the second encounter and the recombined beam is then imaged onto a detector. The beamsplitter introduces a phase-delay between the two beams [Barducci et al., 2010] which generates a spatial interferogram superimposed onto the scene in each frame.

Across the detector array, there is a linear change in phase difference with respect to the optical axis, termed the optical path difference [Barducci et al., 2010]. This results in each column on the detector array measuring a single optical path difference and, therefore, a single part of the spectrum [Lucey et al., 2008]. To create a full spectrum, all optical path differences for a point in the scene must be measured; this is accomplished by operating the instrument in a push-broom mode. The design of the Sagnac interferometer allows spectra to be acquired without the need for moving components within the interferometer, unlike the Michelson interferometer that requires a moving mirror to create the interferogram. A unique characteristic of the Sagnac is that adjustments to either one of the mirror's alignment can increase or decrease the spacing of the fringes within the interferogram and therefore can change the spectral resolution of the instrument [Alain, 1994].

Instruments using the Sagnac interferometer have many advantages for small satellites. The lack of moving parts make the instrument robust against vibrations, alignment problems, and mechanical failure [Alain, 1994] while also allowing them to be compact, lightweight, and power

efficient. Such instruments are also attractive for the fast moving platform of small satellites because they operate in a push-broom mode unlike the Michelson interferometer, which requires staring at a single location while the mirror is mechanically moved to produce the interferogram [Schott, 2007; Alain, 1994].

2.2.2 Collection of Data and Processing

As mentioned in the previous section, a single acquired frame of a scene will contain only part of the optical path difference needed to construct a spectrum (Figure 2.3a). This is closely analogous to a linear variable filter spectrometer, where each column corresponds to an individual wavelength. Obtaining the complete spectral information is accomplished by scanning the interference pattern across each point of interest and acquiring multiple frames (Figure 2.3a). The resulting data set is co-registered into a data cube containing the full image of the scene at all the optical path differences for each pixel on the array (Figure 2.3b). Within this data cube, each pixel now has the complete interferogram needed to derive a spectrum stored along the z axis (Figure 2.3b and c). Standard Fourier transform operations are then performed on each interferogram to derive a fully calibrated spectral radiance cube (Figure 2.3d). Each pixel within the spectral radiance image cube now contains a complete spectrum also stored along the z axis (Figure 2.3e).

2.2.3 The MIDAS Instrument

The MIDAS instrument contains an uncooled microbolometer married to a Sagnac interferometer. The size and configuration of a Sagnac interferometer place boundary conditions on the instrument design. Sagnac interferometers have an aspect ratio that controls the amount of vignetting that will occur in the images and therefore limits the field of view (FOV) to be less than or equal to the aspect ratio of the interferometer [Seller and Boreman, 2003]. The aspect ratio is defined at the ratio between the entrance and exit aperture, i.e., the beamsplitter, and the distance between the two apertures if the interferometer is unfolded [Seller and Boreman, 2003]. For the triangular configuration, the aspect ratio is 6.8 to 1 for a refractive index of 1 [Lucey et al., 2008; Seller and Boreman, 2003]. The FOV and the size of the focal plane then fixes the focal length of the instrument. Ideally a lens with an f-number of 1 is desired for high sensitivity, but to reduce vignetting, an f-number closer to 2 is desired. Low f-numbers improve sensitivity for any optical system, but increase vignetting. For the MIDAS instrument, we compromised with an f-number

between the two of 1.4 to optimize the sensitivity and minimize the vignetting. The size of the lens then dictated the size of the interferometer so that an aperture with a clear field of view was achieved.

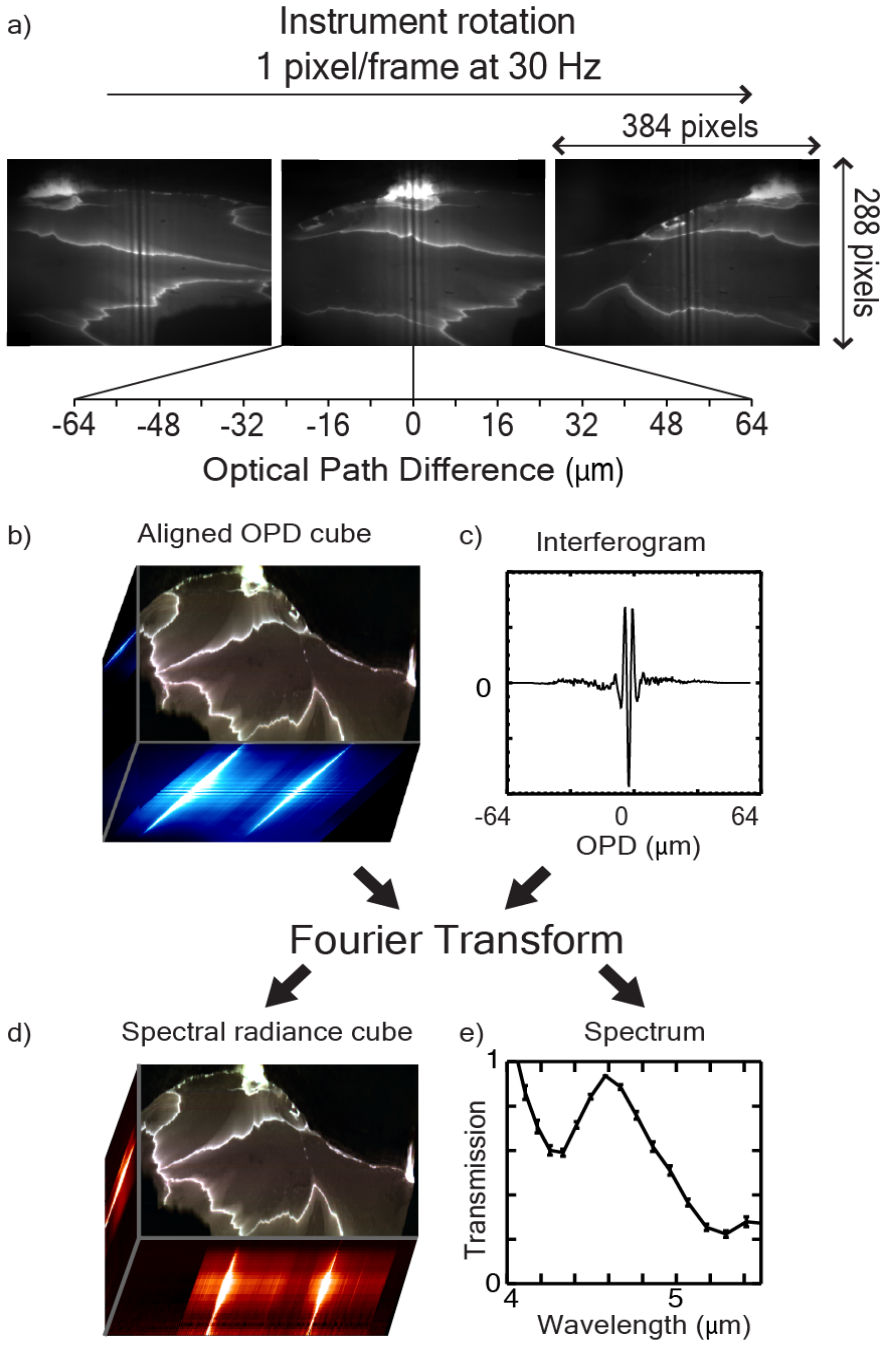

Figure 2.3: Collection of hyperspectral data by scanning a scene, stacking the frames and "drilling" down through the cube to extract an interferogram for each element in the array. Performing Fourier Transform techniques on the interferogram derives a calibrated spectral radiance spectrum for each scene element.

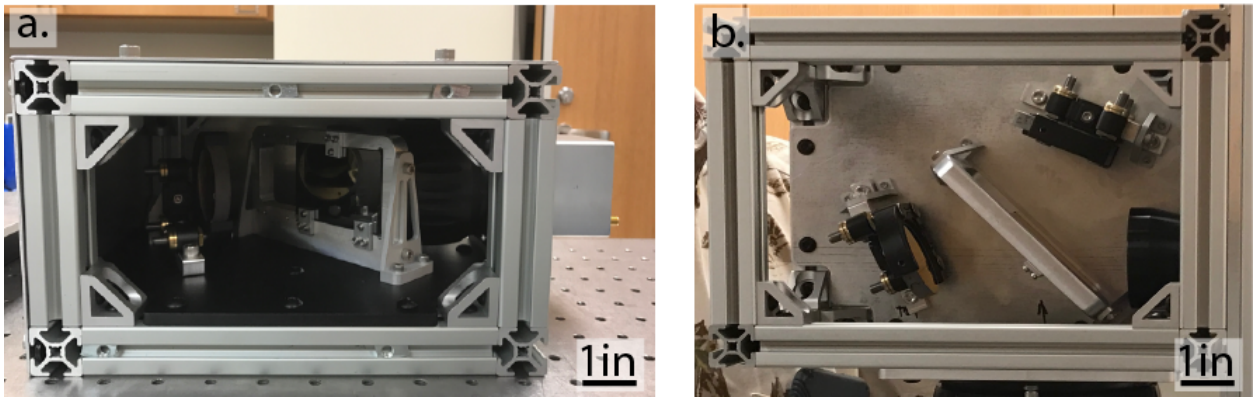

Figure 2.4: a) The packaged MIDAS instrument with the uncooled microbolometer. b) The triangular Sagnac interferometer.

The MIDAS instrument (Figure 2.4a) consists of three components, the Sagnac interferometer, a Fourier transform lens (used to image the interferogram onto the detector), and the uncooled microbolometer. The Sagnac interferometer (Figure 2.4b) is made of two gold-coated fold mirrors that are 25.4 x 25.4 mm from Thor labs and a 76.2 x 50.8 x 10 mm ZnSe beamsplitter from Spectral Systems LLC. The Fourier transform lens has a 50 mm focal length that was a custom designe and built for the MIDAS instrument by New England Optical Systems. Lastly, the microbolometer used is the INO MicroXcam and the specifications for the detector are listed in Table 2.1. One of its important features is a spectrally flat gold-black coating. A replica instrument was also built using the same optics as MIDAS, but instead used the IRCamera 803 liquid nitrogen (LN_2)-cooled InSb photon detector as the sensor. The specifications are also listed in Table 2.1. We compared the performance of the MIDAS instrument to the cooled variant (CIDAS), which is used as a standard.

Table 2.1 Detector specifications

Detector	**INO MicroXCam-384i**	**IRC803**
Type	VOx, gold-black coating	InSb
Manufacturer	INO	IRCamera
Number of pixels	384x288	320x256
Pixel size	35 mm	30 mm
Spectral range	2 - 14 mm	1 - 5.3 mm
Frame rate	30 fps	478 fps (max)
NEdT	< 35 mK	< 20 mK
Weight	< 1 lbs	< 7 lbs
Power	< 3 W	12 W

2.3 Instrument Characterization and Spectro-Radiometric Performance

For each of the breadboard implementations (uncooled microbolometer and cooled photon detector), we conducted a series of characterization tests: camera stability, wavelength calibration, spectral response, and sensitivity. The sensitivity tests are used to determine how well each instrument can measure radiance as a function of wavelength and spectral resolution. To quantify this, we used three standard sensitivity metrics, signal-to-noise ratio (SNR), noise equivalent spectral radiance (NESR), and noise equivalent differential temperature (NEdT).

2.3.1 Camera Stability

Before conducting any sensitivity tests, we determined the duration of each detector's warm-up period before stabilization. This was performed by having each camera view a blackbody (CI-Systems SR800-8D 8" x 8") at a stable temperature of 100°C for a period of four hours while 100 frames of data were collected every 30 seconds. Data collection began immediately upon turning on the camera. In the case of the IRCamera, data were collected when the focal plane temperature reached ~85 K to avoid damaging the detector. Results from the stability tests are shown in Figure 2.5. The INO microbolometer shows a rapid decrease in Digital Number (DN) within the first hour of being turned on (Figure 2.5a). After the initial hour, the microbolometer has an hour of stable operation before it begins to experience a slight drift in DN around the two hour mark. The drift could be caused by the 1/f noise, fluctuations of the temperature in the room, or the microbolometer warming up from use.

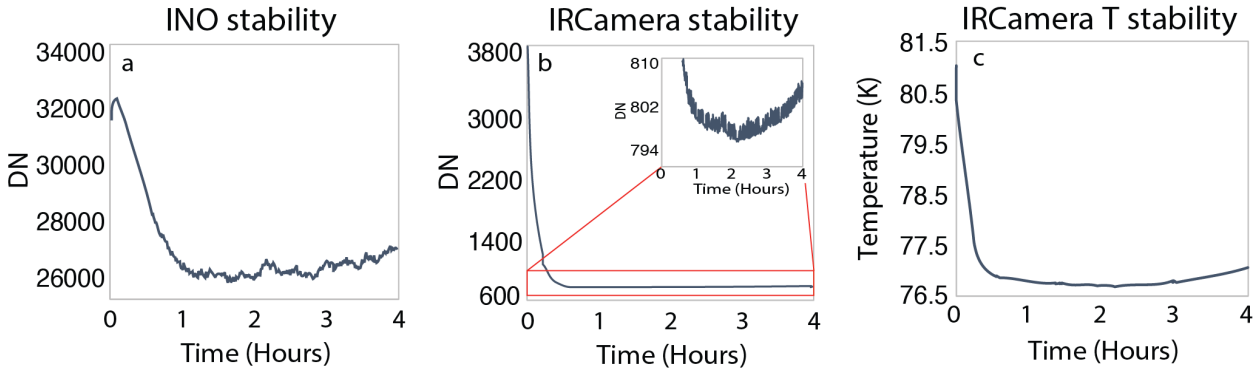

Figure 2.5 Camera DN and temperature stability over a period of four hours. a) The INO camera reaches stabilization around an hour after turn on. b) IRCamera DN stabilized 30 minutes after cooling began, there is a slight drift of DN for the duration of the test. c) IRCamera focal plane temperature is directly linked to DN stability.

We found that the IRCamera required a minimum of 30 minutes to stabilize after initialization (Figure 2.5b). After this time, the camera showed a slight downward drift in output reaching a minimum after two hours and then increasing for the remainder of the test (Figure 2.5b, insert). The LN_2 hold time of the IRCamera dewar is reported to be four hours with the camera running; however, the temperature of the focal plane, as indicated by an on-chip sensor, began to warm up by a few tenths of a K in the last two hours of the test and this small increase was reflected in a slight drift of the output DN (Figure 2.5c). This is likely due to the LN_2 boiling off as the dewar was not refilled during the four hour test. In light of this, subsequent measurements to derive SNR, NESR, and NEdT were conducted between 60 and 120 minutes of camera turn-on for both the INO microbolometer and IRCamera photon detector.

2.3.2 Wavelength calibration

Wavelength calibration of the instruments is accomplished by placing a back-illuminated narrow band filter in front of the interferometer. This produces a peak in the Fast Fourier Transform (FFT) of the interferogram from which the resolution and wavelength positions can be determined. As mentioned in Section 2.2.1, the Sagnac interferometer's spectral resolution can be varied with slight adjustments to one of the mirrors alignment. Spectral resolution and SNR are inversely proportional to one another as the available signal is more finely divided with increasing spectral resolution. Because of this, we conducted sensitivity tests at two spectral resolutions of 50 and 100 cm^{-1}.

2.3.3 Spectral Response of the Individual Cameras

To understand the SNR measurements, we needed to establish the spectral response of the two detectors and how it affects the SNR. The INO microbolometer was manufactured to have a spectrally flat response across 2 to 14 μm, but to be confident in the SNR measurements, we also conducted the spectral response test on the microbolometer. An in-depth description of the spectral response measurements can be found in Honniball et al., (2017) but a brief overview will be given here.

Measurement of the spectral response of each camera required a spectral radiance source with adjustable narrow bands. We used a monochromator (Oriel 77250) illuminated by a hot blackbody set to 700°C. We measured the incident irradiation, which was split by the monochromator into

narrow spectral bands. We calibrated the output of the monochromator with a pyroelectric detector with flat spectral responses. To calibrate the monochromator over the full MWIR region, two gratings were used, the Oriel 77301 [150 l/mm, 3.5μm blaze] for 2 to 5 microns and the Oriel 77302 [75 l/mm, 7μm blaze] for 4 to 9 microns. The two resulting calibration curves were combined into one curve, which is then used to calibrate the microbolometer and photon detector.

The microbolometer and InSb IRCamera spectral response was measured by viewing the calibrated output of the monochromator. The measured digital counts curves of the two cameras as a function of wavelength were divided by the calibration curve measured by the pyroelectric detector. The calibration curve and the full spectral response of the two cameras plus other microbolometers can be found in Honniball et al., (2017). Here we present in Figure 2.6 only the MWIR results of the INO microbolometer and the IRCamera photon detector used in this project.

In Figure 2.6, the solid line represents the calibrated spectral response curve of the cameras. The dashed line is the raw response before the monochromator output is calibrated out. The blue region shows an anomaly around 4.25 μm due to atmospheric CO_2 in the path between the blackbody and the detector, and the red region shows where the two curves were merged for the two different gratings. The INO microbolometer (Figure 2.6a) was found to have a flat spectral response, as expected, from 3 to 6 microns, and even beyond that as shown by Honniball et al.

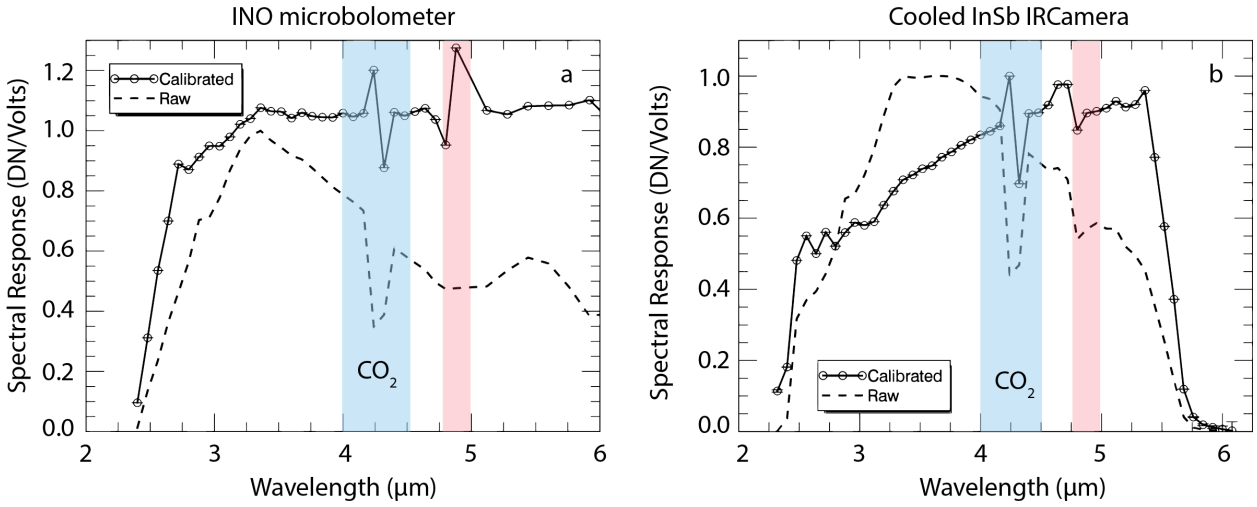

Figure 2.6 Spectral response of the MWIR INO microbolometer (a) and the IRCamera InSb photon detector (b). The dashed lines are raw response of the camera to the output by the monochromator. Solid lines are the raw response divided by the MWIR calibration curve. The anomaly at 4.2 μm (blue region) in the calibrated spectral response curve is due to varying path length and varying CO_2 concentration in the room. The spectral response curve was pieced together from measurements made using two gratings (blazed at 3.5 μm and 7 μm). The transition between the two sets of measurements is shown by the red bar.

(2017). The InSb IRCamera (Figure 2.6b) shows a spectral response typical of InSB detectors [Rogalski, 2002]. For our applications of hyperspectral imaging, the flat spectral response of the INO microbolometer is ideal.

2.3.4 Sensitivity Tests

Measurement and calculation of the sensitivity parameters SNR, NESR, and NEdT required observation of a NIST-traceable large area blackbody at multiple temperatures (Figure 2.7). We used a CI-Systems SR800-8D 8" x 8" that provides temperatures from 0˚ to 100˚C. The acquired data were converted from digital number to spectral radiance using the processing procedure described in section 2.2.2. However, because the blackbody is uniform and filled the FOV of the instruments, scanning was not required. Due to this, any error introduced in the data reconstruction algorithm is not included in the reported sensitivities. After conversion to spectral radiance, the NESR is computed from the standard deviations of the spectral radiance over time. The SNR is derived by:

$$SNR = \frac{L_\lambda}{NESR} \tag{2.1}$$

where L_λ is the spectral radiance at a specific wavelength and lastly the NEdT is found by:

$$NEdT = NESR * \frac{\Delta T}{\Delta L_\lambda} \tag{2.2}$$

where Δ is the change in spectral radiance (L_λ) over the change in temperature (T).

We measured the sensitivity of the instruments at nine temperatures ranging from 10 to 90°C and at spectral resolutions of 50 and 100 cm^{-1} (Figure 2.7). For each sensitivity measurement of a specific temperature, three temperatures were used: two calibration temperatures that bracket the target temperature by ± 10°C, e.g., for a target temperature of 50°C, two calibration temperatures of 40 and 60°C are used. The sensitivity metrics above are calculated from the center rows in the frames to avoid the vignetting effect caused by the instrument's design. Results are shown in Figure 2.7. For both the uncooled INO microbolometer and InSb IRCamera instruments, SNR, NESR, and NEdT were better for the 100 cm^{-1} data compared to that acquired at 50 cm^{-1}. Both instruments show a 50% increase in SNR between the two spectral resolutions. Not surprisingly, the cooled InSb detector instrument is approximately 10 times more sensitive than the microbolometer instrument. However, at 90°C the microbolometer based system provides several

hundred SNR which suggested that it would provide excellent data at the much higher temperature application of gas measurements at a volcanic lava lake.

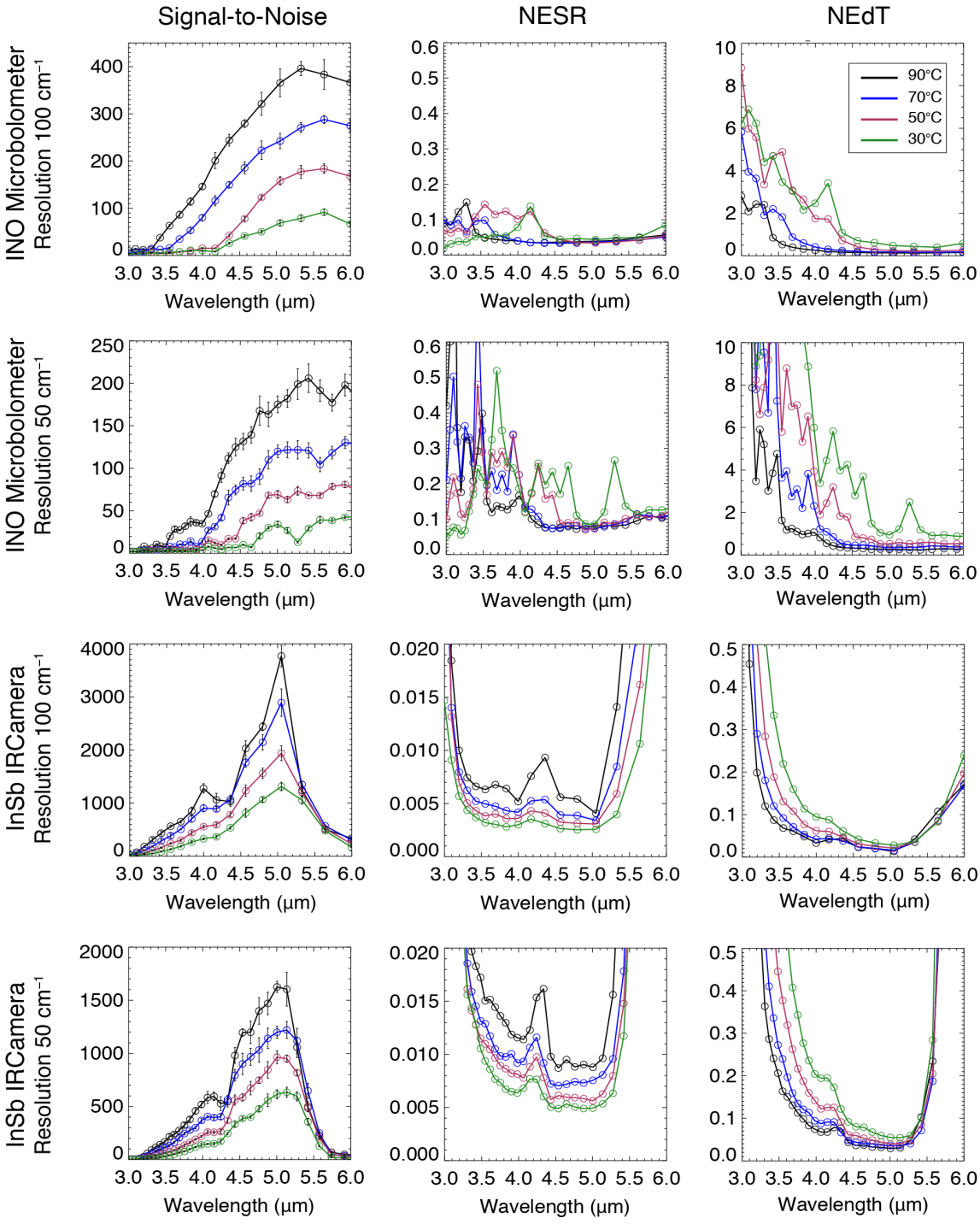

Figure 2.7 SNR, NESR and NEdT measurements of the MIDAS (INO Microbolometer) and CIDAS (InSb IRCamera) instruments at 50 and 100 cm^{-1}.

2.4 Volcanic Gas Observations Using MIDAS

Following the completion of laboratory calibration and instrument sensitivity characterization, MIDAS was prepared for field deployment to the then-active lava lake of Kīlauea Volcano on Hawai‘i Island on July 25th, 2017. From 2008 to 2018, Kīlauea was home to an active lava lake that provided a continuous source of volcanic CO_2, SO_2, and H_2O gases. The high temperature of the lava lake surface provided high radiance allowing for MWIR observations of the emitted volcanic gases. The MIDAS instrument was set up along the edge of the Halema‘uma‘u crater overlooking the lava lake (Figure 2.8). This allowed us to use the lava lake as a source of radiance with the gas plume occupying the space between MIDAS and the lake. MIDAS performed continuous spectral imaging observations of the gas plume over the course of an hour. For this project, we are most interested in quantifying the concentration of CO_2 present in the Kīlauea volcanic gas plume. The CO_2 absorption is at ~4.25 μm, in the center of our wavelength range.

2.4.1 In Field Radiance Calibration

As in the laboratory tests, the MIDAS instrument undergoes two calibrations for accurate observations in the field, a wavelength and radiance calibration. The wavelength calibration in the field is accomplished the same way as described in Section 2.3.2 and was routinely collected.

Figure 2.8 The MIDAS instrument monitoring the late Halema‘uma‘u lava lake.

A radiance calibration is necessary to convert the measured DN to measured radiance. In the laboratory, this is performed by observing large area NIST traceable blackbodies at two temperatures surrounding the target temperature to allow interpolation. In the field, and for target temperatures below 100°C, this is easily accomplished using portable blackbodies. However, typical lava lake surface crust temperatures range from 300 to 500°C [Peale et al., 1979; Howell 1997], and our available portable blackbodies cannot reach such temperatures. So, we are forced to extrapolate the calibration to high temperature. We used a portable blackbody that is observed at 50 and 100°C. The calibration frames are then converted from temperature to radiance units because the extrapolation to higher temperatures in units of radiance is nearly linear while in temperature units the extrapolation is non-linear. The non-linearity with temperature is due to the non-linear function of photons with temperature. After the data is radiance-calibrated, we calculated the brightness temperature at 4.0 μm (Figure 2.9). The temperatures derived from the lava lake are within the range reported by Spampinato et al. (2008) and Patrick et al. (2018) indicating that the extrapolated radiance calibration is performing well.

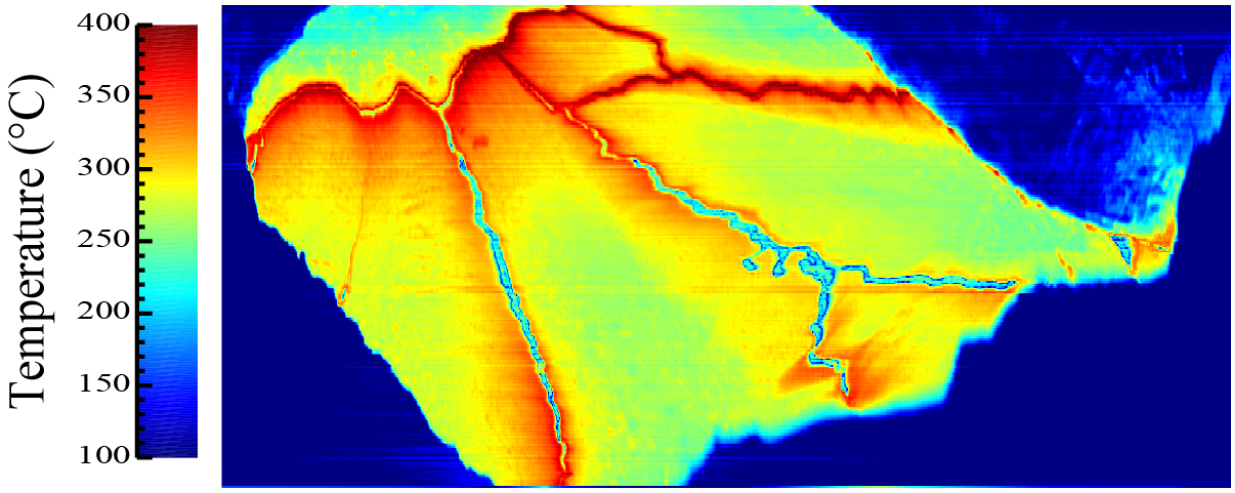

Figure 2.9: Brightness temperature map calculated from the spectral radiance map of the Halemaʻumaʻu lava lake at 4.0 μm.

2.4.2 Radiative Transfer Modeling

Radiative transfer models are commonly used to interpret remotely obtained infrared spectra of gases and to derive concentrations. For this project, we developed a fully resolved line-by-line radiative transfer model similar to that of Khayat et al. (2015; 2017). For a given gas concentration,

the model calculates the line-by-line, wavelength-by-wavelength, fully resolved transmission spectrum through a given path length. Using the HITRAN database of 2012 [Rothman et al., 2013], gas molecule parameters, such as line strength, transition of central frequency, and broadening coefficients are found. In the model, we neglect multiple scattering due to minimal scattering in the MWIR. Gas emissivity and transmission are assumed to sum to unity.

The transmission and emission spectrum of a gas mixture is calculated assuming a gas mixing ratio, temperature, pressure, and total path length. Radiance is the sum of the gas emission and background radiance (in our case, the radiance from the lava lake) multiplied by the transmission. The resultant fully resolved spectrum is convolved with a Gaussian function at the MIDAS instrument spectral resolution to produce a radiative transfer model at the MIDAS spectral resolution. Assuming the temperature of the volcanic gas plume within the volcanic pit is lower than the surface of the lava lake, (a reasonable assumption since the plume quickly intermixes with the atmosphere and cools rapidly), emission is assumed negligible compared to transmission. However, the exact temperature of the gas plume within the volcanic pit is unknown and very little work on volcanic gas plume temperatures has been conducted. One study reported the temperature of the gas plume near the main vent of Mt. Ontake at 90. 6˚C [Mori et al., 2016]. Based on the measurement by Mori et al., (2016) and the little work done on volcanic gas plume temperatures within the volcanic pit, we assumed a gas plume temperature of 100°C for our radiative transfer models.

To demonstrate the utility of the MIDAS instrument for volcanic gas detection, the total path concentration of the gas plume was sought. The radiative transfer model used the same viewing geometry as MIDAS used in the field. Figure 2.10 schematically depicts MIDAS overlooking the lava lake. Retrieval of gas concentrations measured by MIDAS was compared to spectral data in a large lookup table of gas transmissions with varying gas abundances from 0 to 500,000 ppm. To make this comparison, we first convert the spectral radiance spectra measured by MIDAS to measured transmission. This is accomplished by using the brightness temperature at 4.0 μm (Figure 2.9) and removing a blackbody curve at the given temperature.

Each MIDAS transmission spectrum is compared to model transmission spectra to find the best fit and therefore providing the concentration of gas present. Lastly, because we are mainly interested in volcanic CO_2 for this project, we subtract the atmospheric CO_2 concentration present

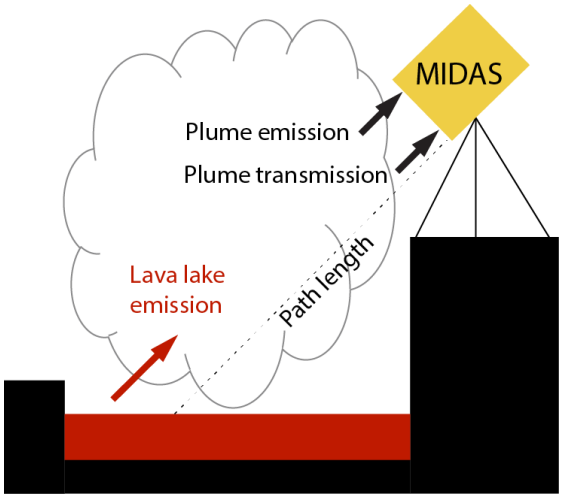

Figure 2.10 Viewing geometry of MIDAS and the radiance through the volcanic gas plume.

on that day. The CO_2 concentration is measured daily on Mauna Loa [Daily CO_2]. For every pixel in the spectral radiance image, a CO_2 concentration is modeled to produce a two-dimensional image of total gas concentration in units of ppm.

2.5 Results of Volcanic Gas Measurements

A single scan is presented here using the aforementioned methods. Each individual frame used an integration time of 30 ms. The spectral radiance image of the lava lake at 4.58 μm is shown in Figure 2.11. Lava lakes are topped with lava that has cooled sufficiently to form a layer of crust typically at temperatures ranging from 573 to 873 K [Peale et al., 1979; Howell, 1997]. This crust

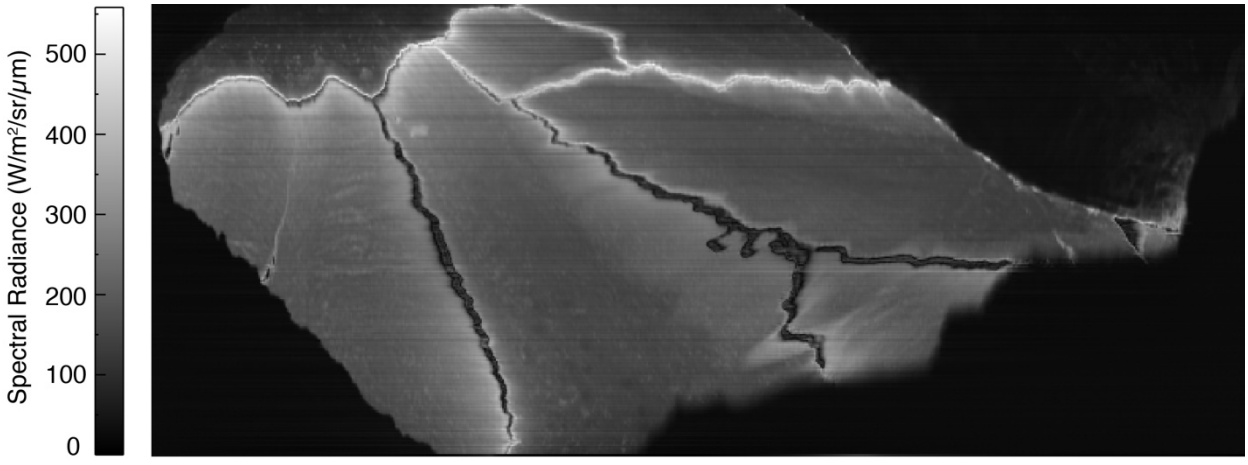

Figure 2.11 Spectral radiance image at 4.58 μm of the Halemaʻumaʻu lava lake. Variations on the lava lake are consistent with temperature differences seen in Figure 8. The black fractures are due to saturation.

is constantly changing and surface fractures come and go. The surface fractures reveal fresh lava at temperatures of ~1400 K [Peale et al., 1979; Howell, 1997]. It can be seen that crust further from fractures are darker, indicating the crust is cooler and older. The variations in the spectral radiance image can also be seen in the brightness temperature map in Figure 2.9. Fractures that appear dark were hot and caused saturation of the detector.

The spectral radiance is converted to transmission, and each spectrum was run through the radiative transfer model. An example of a transmission spectrum acquired by MIDAS is shown in Figure 2.12. The spectrum in Figure 2.12 has a CO_2 abundance of 2,773 ppm with an uncertainty of ± 167 which was derived from the standard deviation of a uniform area in the spectral radiance image on the lava lake.

Fine scale spatial variations in CO_2 abundance over active lava lakes have not previously been reported. The imaging nature of the MIDAS instrument allows us to create an abundance map of CO_2, seen in Figure 2.13. Striping across the map, like the stripe across the top third of the map, is due to effects of noise and artifacts due to systematic noise correction across the image. Light grays areas on the lava lake are plumes where CO_2 is concentrated. Subtle variations near the noise level could be gas escaping from fractures in the crust. Non-saturated cracks do not appear to have

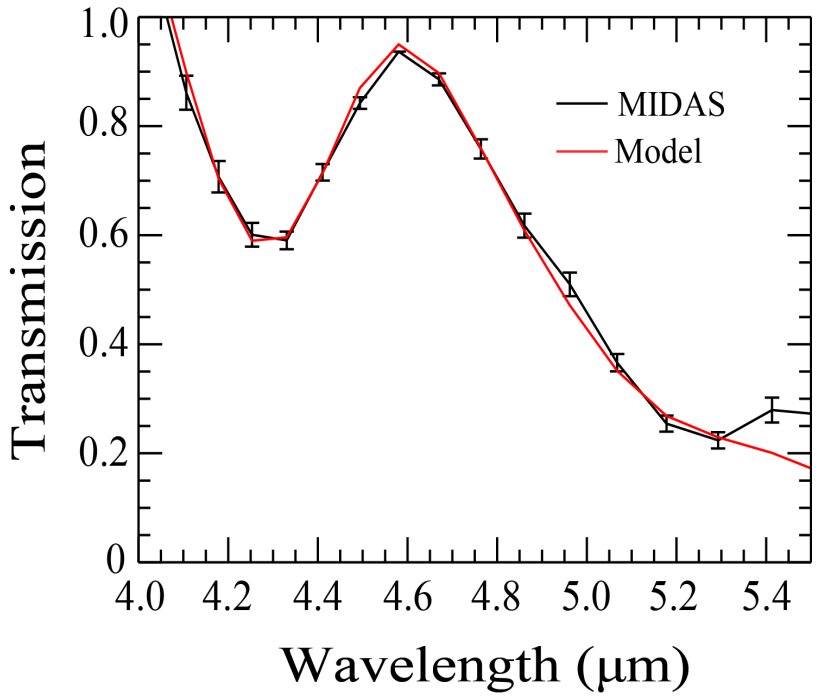

Figure 2.12: Transmission spectrum acquired by MIDAS of the Halema‘uma‘u lava lake (black). Modeled transmission spectrum (red) with CO_2 abundance of 2773 ± 167 ppm.

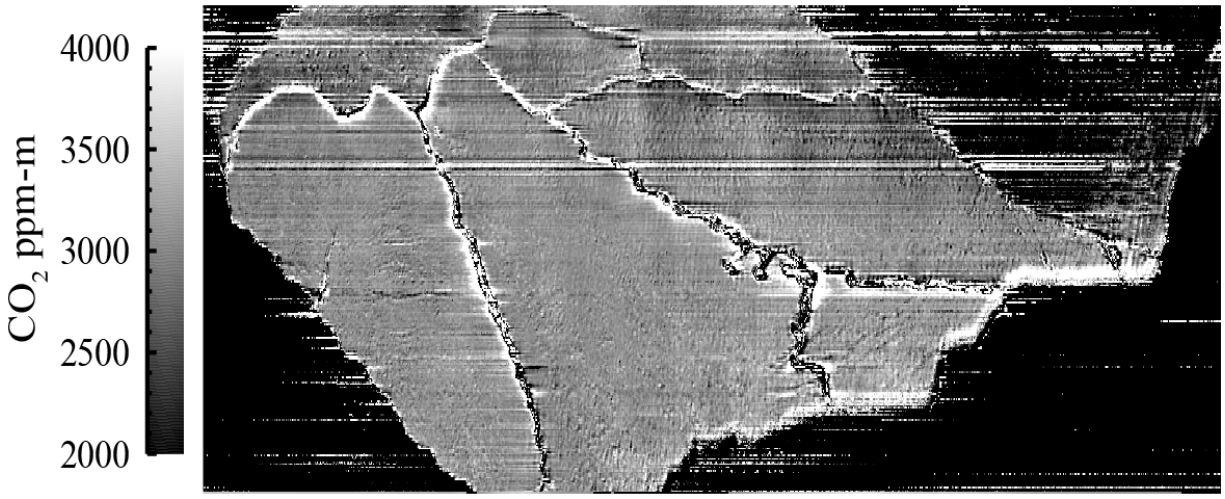

Figure 2.13: Map of CO_2 emanating from the Halema‘uma‘u lava lake on July 25, 2017. Subtle variations can be seen in the image with some areas showing locations of CO_2 plumes.

increased CO_2 emanating from them. It can also be seen that the abundance of CO_2 is not constant across the image as a result of entrainment with the atmosphere. The maximum abundance of CO_2 observed in this scan is 3,313 ± 167 ppm with a minimum of 2,553 ± 167 ppm.

2.6 Conclusions

Despite challenges such as atmospheric absorptions, mixture of signal, and the limited signal available to detect, there remains a wealth of information in the MWIR. Measurements in the MWIR region can provide important information pertaining to the chemical composition of Earth's atmosphere, planetary bodies, and high temperature phenomena such as active lavas lakes. The MIDAS instrument allows hyperspectral imaging in the MWIR by combining relatively insensitive uncooled microbolometers with an imaging interferometer. Instruments like the MIDAS instrument are attractive for space applications due to their low mass and low power consumption. We have demonstrated that uncooled microbolometers coupled with Sagnac interferometers can provide several hundred SNR for targets above 90˚C. An interesting result of the sensitivity tests is that the cooled IRCamera coupled to an uncooled Sagnac interferometer provided high SNRs for temperatures near Earth’s surface temperature. For this cooled variant, while power savings on the detector side are little, the power saved from uncooled optics makes this instrument an interesting candidate for small satellites.

With the MIDAS instrument, we were able to obtain spectral radiance data that show temperatures that are reasonable for active lava lakes. We were able to produce spectral radiance images, brightness temperature maps, and maps of CO_2 from the radiance data for each pixel in the image. Using a radiative transfer model, we found CO_2 abundances between 2,553 – 3,313 ± 167 ppm. The spectrum shown in Figure 2.12 demonstrates that the MIDAS instrument can acquire meaningful and useful spectra in the MWIR and can be used to back out the concentration of volcanic CO_2.

Acknowledgements

I would like to thank Harold Garbeil, Eric Pilger, Mark Wood, Tim Williams, Lance Yoneshige for their assistance and guidance throughout the project, Spectrum Photonics for their manufacturing of the instrument housing and the Geology and Geophysics department at UH. Funding was provided by NASA grant NNX14AN15A.

CHAPTER 3. GROUNDBASED OBSERVATIONS OF LUNAR SURFACE WATER DIURNAL VARIATIONS

Abstract

Prior to 2009, the Moon was believed to be anhydrous. However, observations by three spacecraft revealed a hydroxylated surface by reporting a 3 μm absorption band attributed to hydroxyl (OH) and possibly molecular water (H_2O). The band exhibits variations with lunar time of day, temperature, soil maturity, and composition.

Measurements of the 3 μm band were revolutionary, however, the returned spacecraft data have limitations in spatial resolution, global coverage, lunar time of day, and spectral coverage that make full characterization of the 3 μm band difficult. Recently, the presence of variation in the 3 μm band has been called into question due to uncertainties in spacecraft data. The Moon Mineralogy Mapper (M^3) spectrometer, onboard the Chandrayaan-1 spacecraft provided global coverage at high spatial resolution and several local times of day, however its spectral range ends at 3 μm. Due to the limited wavelength range of M^3, the variation in the band has been called into question due to uncertainties in the thermal corrections. At lunar temperatures, the signal at 3 μm is a combination of thermal emission and solar reflected radiance. This combination is difficult to separate in M^3 data due to the lack of data beyond 3 μm where the thermal emission dominates. This causes attempts to remove thermal emission in M^3 data to be ambiguous, and there is no consensus on how to properly remove the thermal component.

To investigate the validity of variations in the 3 μm band, we used the SPeX infrared cross-dispersed spectrograph at the NASA InfraRed Telescope Facility (IRTF) at Maunakea Observatory in Hawai‘i. With SpEX, we are able to obtain lunar data over a wavelength range of 1.67 to 4.2 μm of the entire Earth-facing hemisphere at 1 – 2 km resolution. The goal of this project is to determine if the 3 μm band exhibits a diurnal variation by utilizing wavelengths beyond 3 μm provided by SpEX to strongly constrain thermal models. If the variation is observed in SpEX data, the variation can be considered real and due to changes in the abundance of total water.

Data has been acquired on ten different nights at multiple locations on the Moon to capture a wide range of local times, temperatures, and compositional regions. From this new data set with

improved thermal removal, we find a diurnal variation of the 3 μm band along with variations with latitude and composition. Along each observed chord, as a function of latitude, there are strong variations in OH/H_2O abundances. Diurnally, we observe a decrease in abundance with increasing lunar local time. We observe an asymmetric trend about the equator that favors the southern latitudes with higher water abundances. We also observe higher concentrations in highland regions and at geologically interesting features such as craters and pyroclastic deposits. The longer wavelengths provided by SpEX have allowed us to examine variations in the 3 μm band and provide definitive evidence that the variations are due to changes in hydration. This result will have great impacts on models for the production of solar wind induced hydroxylation and the storage of OH and possibly H_2O on the lunar surface.

3.1 Introduction

A major discovery in lunar science in 2009 was the report of a widespread 3 μm band on the lunar surface, or across the lunar surface by three different spacecraft, Chandrayaan-1, Deep Impact, and Cassini [Pieters et al., 2009; Sunshine et al., 2009; Clark, 2009]. This hydration feature is in the 2.8 to 3.5 μm region (referred to as the "3 μm band") and is due to the presence of hydroxyl (OH) attached to a metal cation, molecular water (H_2O), or a combination of the two [Stolper, 1982; Starukhina, 2001; King et al., 2004; McIntosh et al., 2017]. The discovery of the 3 μm band on the surface of the Moon was surprising to the lunar remote sensing community. However, it could have been anticipated, as several laboratory studies observed 3 μm bands in experiments simulating the production of OH from solar wind interactions with oxygen-rich materials prior to 2009 [Hapke, 1965; Zeller et al., 1966; Zeller and Ronca, 1967]. These studies showed that bombarding silicate glass materials, analogous to lunar regolith, with high-energy protons, analogous to solar wind, produces OH on the surface of the grain and will exhibit a 3 μm band [Zeller et al., 1966; Zeller and Ronca, 1967] and was later confirmed by advanced studies [Ichimura et al., 2012; Mattern et al., 1976; Siskind et al., 1977; Guermazi et al., 1987; Gruen et al., 1975; Bradley et al., 2014]. However, what probably could not have been predicted by these studies was the observed variation in the 3 μm band on the lunar surface.

Variations of the 3 μm band intensity with temperature were reported using global imaging maps of the Moon by the infrared High Resolution Imaging spectrometer on Deep Impact [Sunshine et al., 2009]. From the spacecraft's distant vantage point during one of its two lunar flybys, the spectrometer captured global snapshots of the Moon. These data revealed a correlation between lunar surface temperature and the strength of the 3 μm band (Figure 3.1). The Chandrayaan-1 Moon Mineralogy Mapper (M^3) spectrometer collected data from lunar polar orbit. During periods of repeat coverage, Pieters et al. (2009) reported diurnal variations in 3 μm band depth. The high resolution of the M^3 instrument also revealed variations with lunar composition (aluminum rich highlands vs. iron rich mare), lunar latitude (independent of the observed diurnal variations), and lunar surface maturity (variation in degree of space weathering) [Pieters et al., 2009, Sunshine et al., 2009, Clark, 2009; McCord et al., 2011; Li and Milliken, 2017; Wohler et al., 2017; Grumpe et al., 2019].

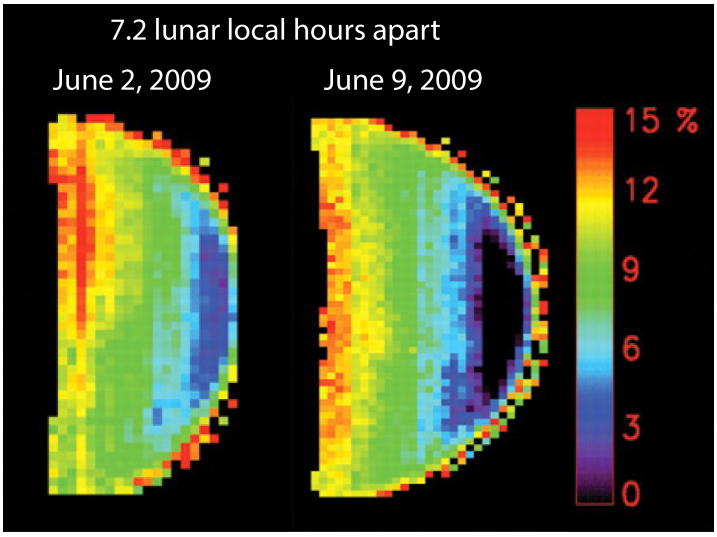

Figure 3.1: Deep Impact observations of the Moon of two separate days where the local time on the Moon advanced by 7.2 hours. The color represents the strength of the 2.8 µm band. [Sunshine et al., 2009]

Variations in the 3 µm band have important implications for how the lunar surface interacts with the solar wind and micrometeoroids, and how water may be transported to the poles to sustain lunar polar ice deposits. However, the degree of band depth variation reported may not correspond to variations in abundance. It is known that thermal emission from the lunar surface can influence the apparent depth of the 3 µm band, but experts differ in how to compensate for this effect [Li and Milliken, 2017; Wolher et al., 2017; Grumpe et al., 2019; Bandfield et al., 2018]. The 3 µm region is complicated by the fact that it is a combination of solar reflected radiance and thermally emitted radiance [McCord et al., 2011]. At 3 µm, in all data acquired of the Moon, the measured quantity contains both a reflected and emitted component. Which term dominates (i.e., reflected or emitted) depends on solar illumination angle, albedo, average lunar surface temperature at the lunar time of day the data was collected, and the amount of shadows (due to surface roughness) present in the scene causing sub-pixel temperature mixing. Figure 3.2 demonstrates this mixture of radiance components. The intensity of the 3 µm band depth can be due to variations in the ratio of thermal to reflected radiance. Rather than the band varying due to changes in abundance of OH and/or H_2O, the variation could be due to thermal infill of the 3 µm band, which is strongly influenced by the surface temperature and illumination conditions. To interpret the lunar spectrum and investigate variations and the abundance of OH + H_2O (referred to as "total water" in the FTIR community [Stolper, 1982; McIntosh et al., 2017]) in the 3 µm band, the thermal emission must be removed.

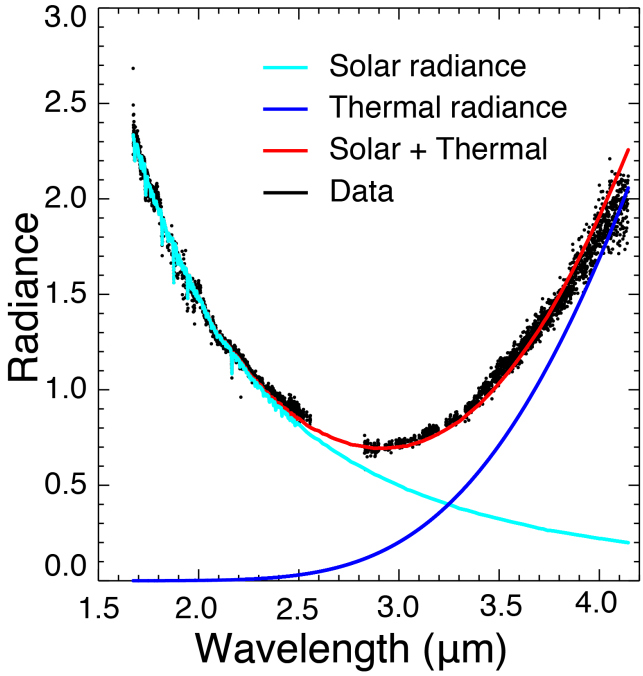

Figure 3.2: Spectrum of the Moon showing thermal (blue) and reflected radiance (cyan). Reflected radiance dominates at shorter wavelengths while thermal radiance dominates at longer wavelengths.

3.2 Background

Data acquired by the Chandryaan-1 M^3 spectrometer [Pieters et al., 2009] is most commonly used to investigate the 3 μm band variations due to its near global coverage at multiple lunar times of day. Three independent studies [Li and Milliken, 2017; Wolher et al., 2017; Grumpe et al., 2019; Bandfield et al., 2018] have addressed the removal of thermal emission and the variation of the 3 μm band using M^3 data, each study coming to a different conclusion. Li and Milliken (2017) reported strong variations with latitude, low abundances of total water near the equator and high abundances near the poles, and a strong diurnal effect between ~30˚N/S and ~60˚N/S that is asymmetric between morning and evening. Wolher et al., 2017 and Grumpe et al., 2019 reported weak variations with latitude and no diurnal effects below ~30˚N/S but strong diurnal effects above ~30˚N/S that is symmetric between morning and evening. These aforementioned studies suggest the variation in the 3 μm band is due to changes in abundances. And lastly, Bandfield et al. (2018) reported a 3 μm absorption band that is always present, but their analysis shows no variation with lunar time of day, temperature, or latitude (Figure 3.3). This study suggests the variation in the 3

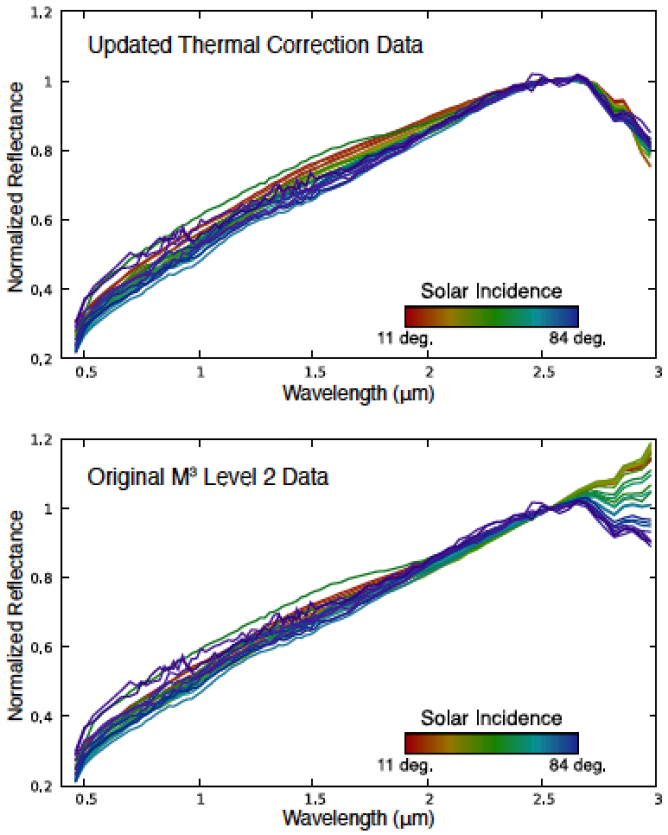

Figure 3.3: Bottom: Thermally corrected M^3 data archived at the Planetary Data System. Top: same data corrected by Bandfield et al. 2018. It is not known if the Bandfield et al. correction would perform properly at longer wavelengths.

μm is due to thermal infill instead of changes in abundance. These opposing results allow no definitive conclusions to be drawn about the behavior of the 3 μm band and therefore, the abundance of total water on the Moon.

The three studies differ because they treat the problem of thermal removal at 3 μm differently. Each study uses subtly different assumptions regarding the photometric and sub-pixel temperature behavior of the Moon, and these slight differences led to their different conclusions. Furthermore, data from M^3 suffer from a fundamental and technical limitation: the data are limited to wavelengths below 3 μm while most thermal emission is at longer wavelengths. The reliability of the thermal correction is only very weakly constrained by the M^3 data itself and there is little constraint on how realistically the thermal component has been removed.

McCord et al. (2011) pointed out that observations of the lunar surface at wavelengths beyond 3 μm would greatly improve the removal of thermal emission and are even strongly recommended. To illustrate this limitation of M^3 data and the value of longer wavelengths, we acquired spectral

measurements using the NASA InfraRed Telescope Facility (IRTF) on Maunakea in Hawai‘i (Figure 3.4). The data were acquired at a latitude of 11°S, with the lunar surface at a temperature of ~300 K, and a lunar local time of ~08:00 am. The modeling is described in detail in Section 3.5 but applied here as a demonstration. The spectrum in black in Figure 3.4 shows the spectrum with an optimum thermal model with a temperature of 297 K applied to remove the thermal component, while the green, blue, and red spectra have thermal models removed that are different from the optimized model by ± 2, 5, and 10 K, respectively. Figure 3.4a shows the spectra cut off at 3 µm, similar to the M^3 data. With only the shorter wavelengths available, it is not possible to determine which thermal model and temperature is correct. All spectra in Figure 3.4a show, what appear to be, valid variation in the apparent band strength of the 3 µm band, varying from no absorption (top red spectrum with a model at 287 K) to a strong absorption (bottom red spectrum with a model at 307 K). However, if we apply these same models to longer wavelengths provided by the IRTF data (Figure 3.4b), we see that the data from 3.5 µm to 4.2 µm show a behavior that is not appropriate for lunar spectra, with one spectrum even going to negative reflectance values. These plots demonstrate the issue surrounding the M^3 data set and the utility of longer wavelengths to constrain thermal models.

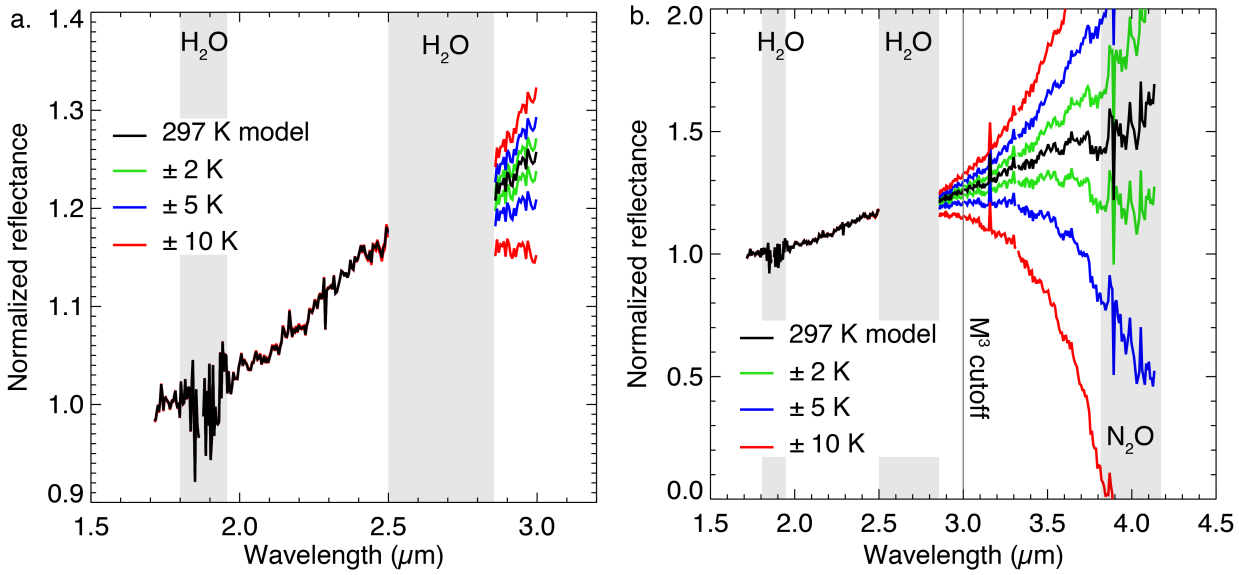

Figure 3.4: Demonstration of the importance of wavelengths beyond 3 µm. Data is of the Moon acquired by the IRTF at a latitude of 11°S and a lunar local time of ~08:00. The black spectrum is the data with the correct thermal model removed while the others are the same data with models ± 2, 5, and 10 K from the proper model. a) shows the data cut off at 3 µm similar to M^3 while b) shows wavelengths out to 4.2 µm. In a, it is difficult to know which model is correct as the different 3 µm band strengths are reasonable measurements. In b however, it is clear when you apply incorrect thermal models to the data, the longer wavelengths no longer spectrally make sense for the lunar surface.

3.3 Contribution of Groundbased Astronomical Observations

Cassini and Deep Impact were spacecraft missions to other Solar System bodies that observed the Moon as a calibration target on the way to their final destination [Sunshine et al., 2009; Clark, 2009]. As a result, the data acquired were few and have low spatial resolution. M^3 on the other hand, from its vantage point in lunar orbit, provided nearly global high spatial resolution data at three separate lunar times of day. Unfortunately, as discussed above, M^3's spectral range ends at 3 µm making it difficult to accurately correct for thermal radiation plaguing M^3 data (Figure 3.4). These limitations to spacecraft data make it hard to address variations in the 3 µm band. Fortunately, observations from the groundbased NASA IRTF using the SpEX near-infrared spectrograph provide the spectral range, temporal coverage, and spatial resolution needed to independently investigate the 3 µm band variations (Figure 3.5).

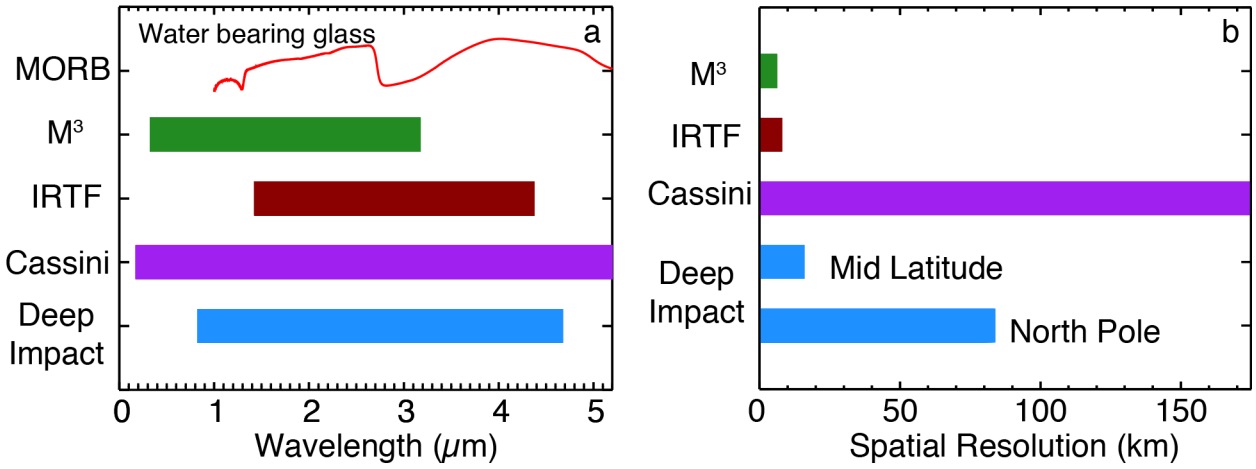

Figure 3.5: Comparison of M3, IRTF, Deep Impact and Cassini spectral range (a) and spatial resolution (b). The IRTF provides both the spectral coverage and spatial resolution needed to observe diurnal variations on the Moon.

SpEX provides a spectral range from 1.67 to 4.2 µm; the longer wavelengths are of extreme importance for this project as they provide a strong constraint on thermal models. Data from SpEX also provide access to the lunar nearside at all lunar times of day with a spatial resolution of 1 to 2 km (at the center of disk), capable of resolving small geologic targets. In addition, access to the entire nearside hemisphere allows us to examine the variations with latitude and the temporal coverage allows us to address how and if the species creating the 3 µm band is varying with time of day.

The existence of variation in the 3 μm band, called into doubt by Bandfield et al., 2018, is central to testing hypotheses for behavior of volatiles on the lunar surface. An independent test of the existence of this variation is the subject of this chapter. Here, we present a study of the variation of the 3 μm band using a new data set from the groundbased IRTF that allows us to address the thermal modeling issues by providing data beyond 3 μm with coverage not available in M^3 data. A strength of using groundbased data is the access to true diurnal coverage. The IRTF allows us to control variations with composition by observing the same regions over multiple lunar times of day with varying temperature, and therefore, revealing the true nature of diurnal variations. If variations are still observed with the improved thermal removal, they are likely caused by changes in abundance of total water. In this case, variations in the 3 μm band seen with time of day, latitude, composition, and soil maturity can be taken as real changes in abundance. We will derive total water abundances and compare our estimates to previous spacecraft estimates.

3.4 Lunar Observations with the IRTF

Observing the same lunar locations at multiple times throughout the lunar day and latitudes allows us to assess the diurnal variation of the 3 μm feature. With each passing Earth night, the time of day at a location on the Moon advances by ~0.8 lunar hours. Observations of the same location for multiple Earth nights and across different observing runs allows us to look at how the lunar time of day, and therefore, temperature of the surface, affects the variation in the 3 μm band.

Data were acquired with the IRTF SpEX cross-dispersed spectrograph imager that collects data from 1.67 to 4.2 μm using a 0.3 x 15 arcsecond slit (about 0.6 x 30 km at the lunar center of disk). We collected data in two modes that we call “maps” and “chords” (Figure 3.6). In maps, we treat SpEX as a pushbroom imager, collecting data while the spectrometer is read out, and using telescope control to scan the slit across the Moon. The advantage of "maps" is that it produces true images that are useful for finely locating features and assessing the presence of artifacts (Figure 3.7). Maps are relatively time consuming to acquire as it takes about 2 seconds to read out the spectrometer data for each frame and we limit our rate of advance to ~2 arcseconds (~ 4km) per frame to provide a completely sampled image. Chords orient the slit along the axis of scan and are offset by 7 arcseconds per frame allowing us to scan much faster with continuous and adjacent spectra, producing spectral profiles, however, we lose the second axis of spatial information.

We have acquired data along three chord lines on two consecutive nights in two different months, pole to pole maps on two consecutive nights, and four chord lines from pole to pole on different nights (Fig 3.6, 3.7 and Table 3.1). The pole to pole chord lines and maps are used to examine variations of the 3 μm feature as a function of lunar time of day and latitude.

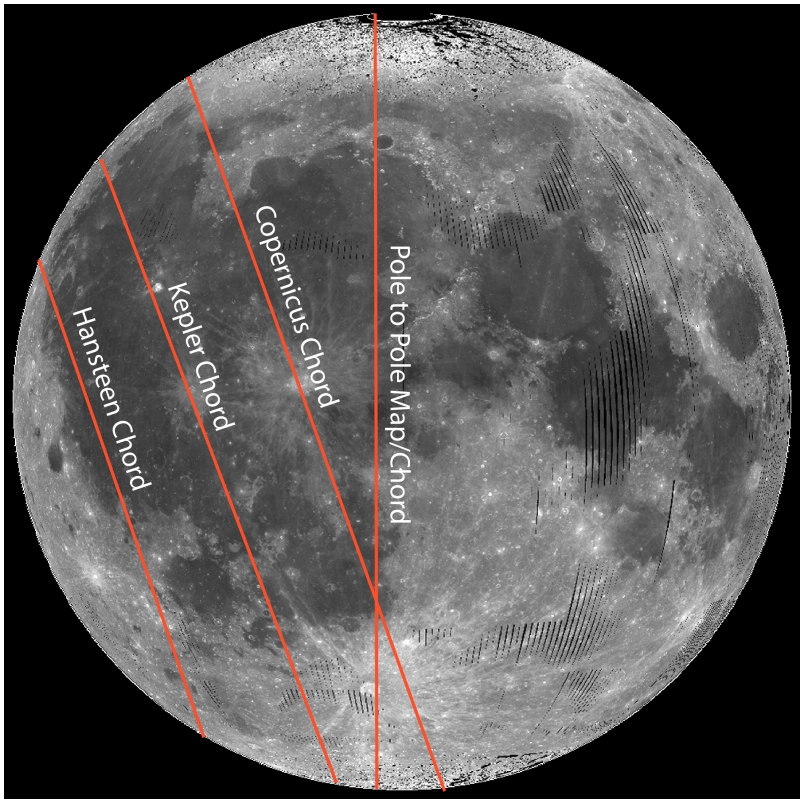

Figure 3.6: Locations of lunar observations for this project. Each line indicated were data was collected. All were observed on two to three consecutive nights to capture any variation in the 3 μm absorption band with temperature and time of day.

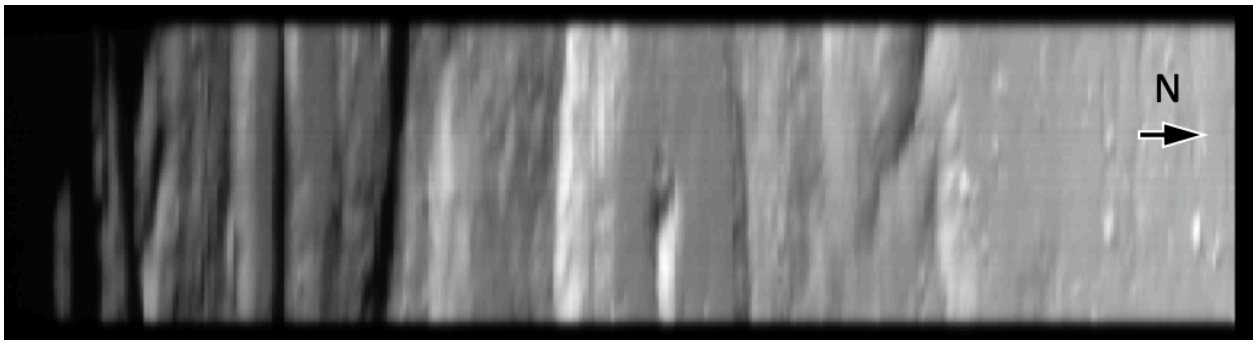

Figure 3.7: Map of high southern latitudes from ~65° to the pole using SpEX as an imaging spectrometer.

Table 3.1 List of data acquired.

Observation	Date HST	Lunar local time	# of observations a night	Phase Angle
Hansteen Chord	Oct 21 2018	0503-0722	2	28.8°, 28.4°
	Nov 19 2018	0556-0650	1	36.9°
	Nov 20 2018	0459-0729	2	25.1°, 24.9°
Kepler Chord	Oct 21 2018	0444-0921	2	28.6°, 28.3°
	Nov 19 2018	0603-0833	1	37.2°
	Nov 20 2018	0549-0901	1	25.2°
Copernicus Chord	Oct 21 2018	0557-1213	1	29.1°
	Nov 19 2018	0422-1255	3	37.8°, 37.6°, 37.4°
	Nov 20 2018	0544-1116	1	25.5°
Pole to pole map	Jan 17 2019	0911-0933	1	40.3°
	Jan 19 2019	1023-1129	1	11.5°
Pole to pole chord	Mar 27 2019	1632-1734	1	-84.1°
	May 13 2019	0704-0749	1	74.0°
	May 14 2019	0757-0837	1	60.7°
	May 15 2019	0847-0854	1	47.1°

3.5 Data reduction

The SpEX instrument offers several data collection modes: we used "LXD Short" that acquires spectra of the lunar surface from 1.67 to 4.2 μm with a spectral resolution of R ~ 2500 [Rayner et al., 1998]. The Moon is the brightest and most extended object in the night sky, so lunar observations with SpeX are therefore susceptible to saturation. To avoid saturation, we use the narrowest slit available and integration times ranging from 0.5 to 1 second depending on the illumination conditions. If saturation is observed, it is typically at longer wavelengths near 4 μm and can be avoided in processing and interpretation, while still allowing wavelengths between 3 and 3.5 μm to be used for thermal modeling.

The main advantage of SpEX is the full spectral coverage of the 3 μm absorption feature. SpEX provides this spectral range over seven spectral orders with partially overlapping wavelengths (Figure 3.8 and 3.9). Each order is extracted separately and spliced together in wavelength space during custom data reduction. Furthermore, each order overlaps the next by a few microns. When splicing the orders together, care is taken to avoid low signal areas in each

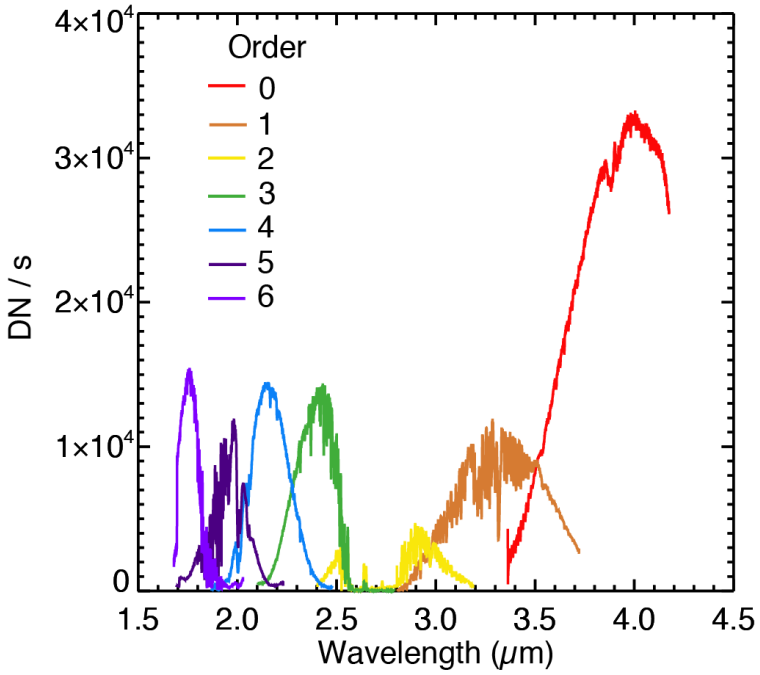

Figure 3.8: The 7 overlapping crossed dispersed orders of SpEX.

order. A wavelength calibration is performed at the beginning and end of each observing run using an argon lamp calibration box attached to SpEX.

SpEX exhibits stray light, that is, a diffuse background of light from scattering within the spectrometer. Typical observations of stars and other point sources remove this stray light background through a process called "nodding", but nodding cannot be used for objects that fill

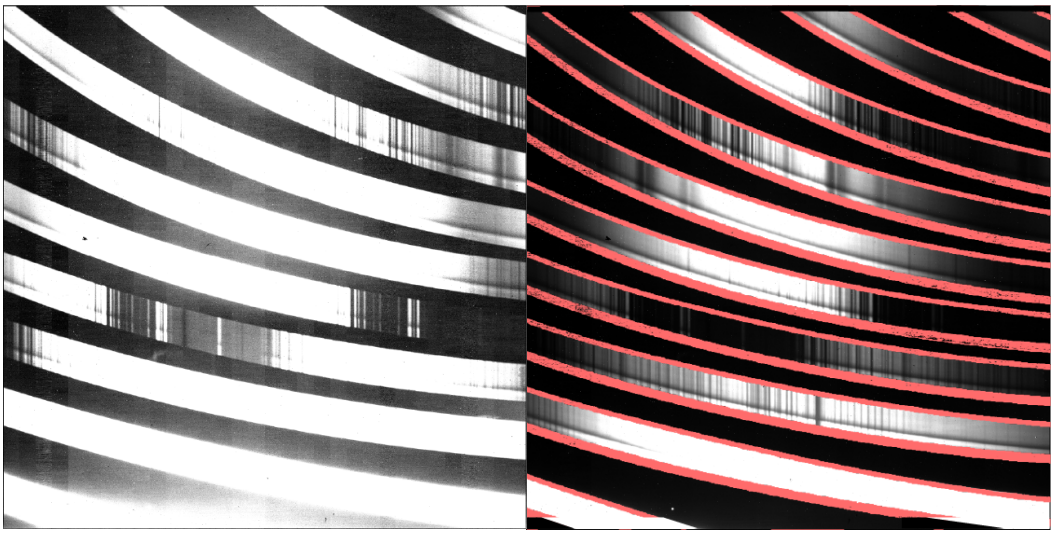

Figure 3.9: The bright stripes are the 7 crossed dispersed orders of SpEX. Stray light can be seen between the orders when the contrast of the image is enhanced (left). The red stripes on the right indicate where stray light was moved into each order.

the entire slit like our lunar observations. The stray light can be seen in the raw data between each of the cross dispersed orders, Figure 3.9. The standard software to reduce data from SpEX is the IDL-based spectral reduction tool SpEXTool [Cushing et al., 2004], which offers a way to remove the background in observations of point sources that do not fill the spectrograph slit. Because the Moon fills the spectrograph slit, we developed a method to use SpEXTool on stray light that appears outside the slit. Stray light is identified and moved from above and below each order into its respective order along the edges of the slit (Figure 3.9). At this position SpEXTool can be instructed to subtract this portion of the slit where we have moved in stray light from the data (these portions of the slit have low response and are discarded in processing by us, so do not result in loss of data). We then process the modified raw data with the stray light correction through SpEXTool as usual. An example of the stray light correction is shown in Figure 3.10.

The initial data reduction steps include internal flat fielding, wavelength calibration, and nonlinearity correction of each spectrum. The spectra are then extracted at 10 locations along the slit, and the flux is summed within a user defined aperture of 0.5". After the data is processed

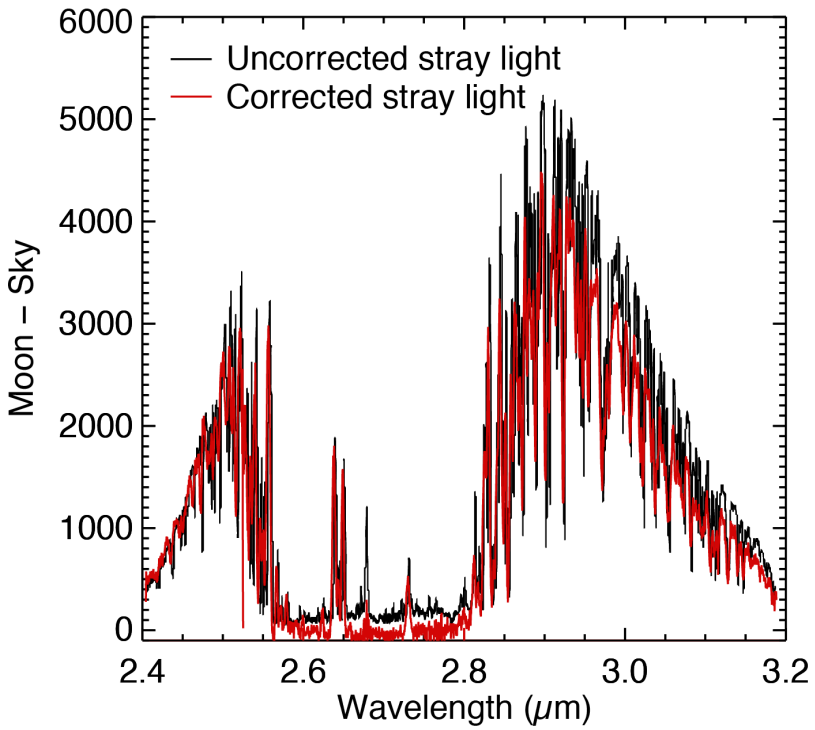

Figure 3.10: Example of the stray light correction in the opaque water region of the atmosphere from 2.5 to ~2.8 μm. The black spectrum sits on a pedestal of stray light causing the band to appear to have signal. Data after stray light removal is shown in red and now has a mean value of zero as expected in a region that is opaque.

through SpEXTool, we further reduce the data using custom IDL scripts. Groundbased telescopic data are effected by background sky emissions from the Earth's atmosphere emitting in the infrared as well as absorptions due to the atmosphere, termed telluric absorptions. To characterize the background sky emissions, observations of the sky are taken just off the limb of the Moon which captures telescope and sky emission background (Figure 3.11b). These data are then subtracted from the lunar spectra (Figure 3.11a). Correction of telluric absorptions are accomplished by normalizing data to observations of stars that have similar spectral properties as the Sun, typically called solar analog stars (Figure 3.11c). Stars are selected from solar analog stars used for asteroid observations from the IRTF [Takir and Emery, 2012]. The solar analog spectrum is divided out

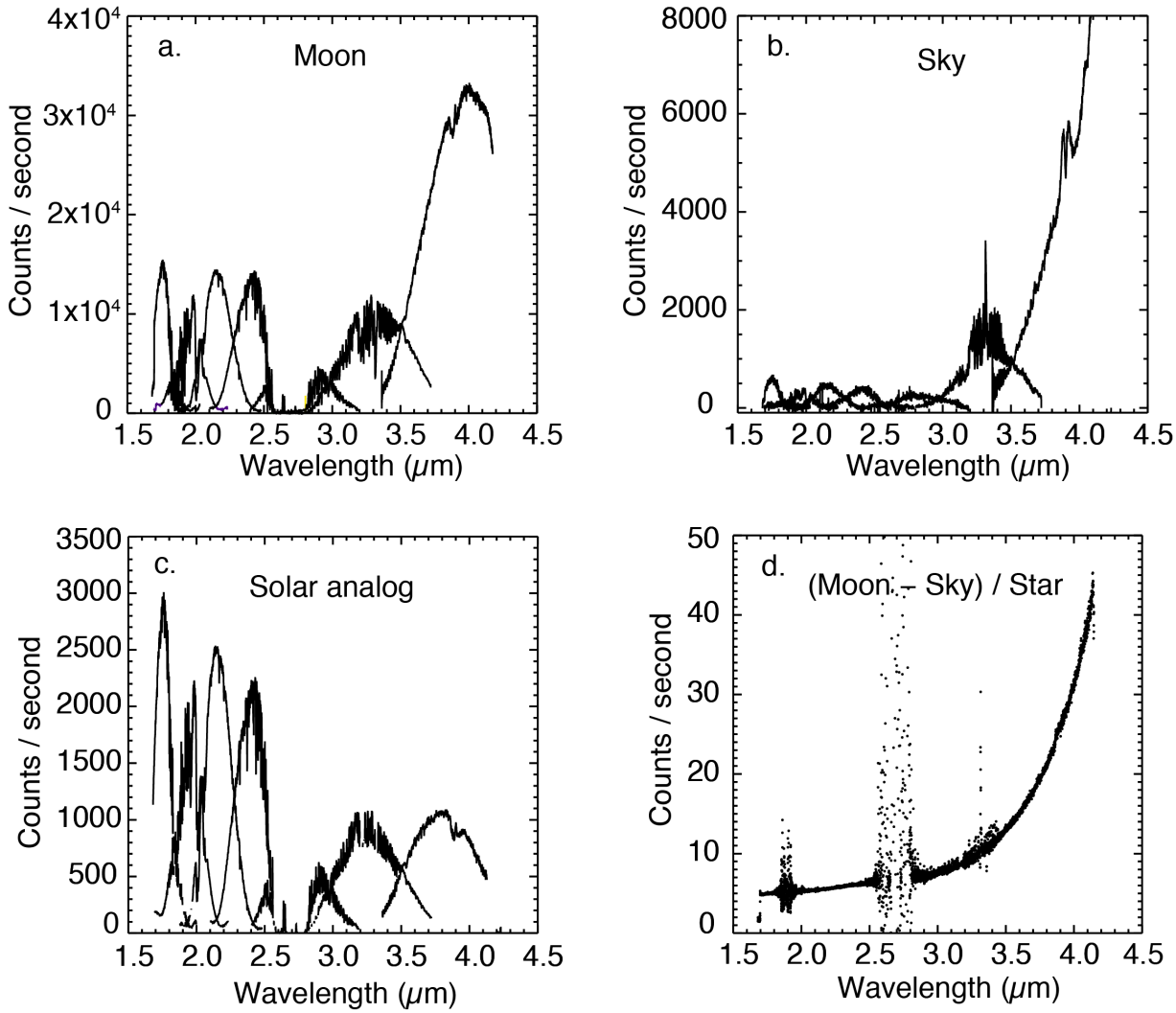

Figure 3.11: Processing steps to remove background sky emissions and telluric absorptions.

from the sky corrected lunar data to remove atmospheric absorption lines (Figure 3.11d). While we chose calibration stars that are close in proximity to the Moon with a similar airmass, some telluric absorptions are not fully removed due to differences in atmospheric conditions between the lunar observations and star observations.

Throughout each night, small shifts in wavelengths occur. This is caused by the weight of the instrument causing slight motion of spectrometer internal components. When the telescope is pointed to a new location on the sky the wavelength position will shift slightly due to the shift in weight. This needs to be corrected for proper telluric and sky emission removal. We corrected this using strong atmospheric lines and shift each lunar and sky spectrum to the wavelength calibration of the solar analog star. After correcting for wavelength shift, telluric absorption, and sky emission, the spectra are ready for further processing to separate reflectance and emission.

3.6 Removal of Thermal Emission

Lunar spectra longward of 2.5 μm are heavily affected by thermally emitted radiance (Figure 3.2). This thermal radiation is dependent on temperature, albedo, emissivity, surface roughness, and thermal inertia. As pointed out above, accurate removal of thermal radiation is vital for investigation of the 3 μm feature and its variation. Observations of total water on asteroids has been conducted since 1978 (Lebofsky, 1978) and asteroid spectra are also affected by thermal emission. For this lunar work, we follow the methodology widely used for asteroid thermal radiation removal defined by Rivkin et al., 2005, Reddy et al., 2009, and Takir and Emery, 2012 in part because they also used SpEX for their asteroid observations and so this method is well established for that spectrometer.

Planetary astronomers observing in the visible and near IR typically normalize their data to solar analog stars that have a spectral shape similar to the sun. This normalization provides astronomical spectra that are similar to spectra of samples with the same composition measured in the laboratory. However, at longer wavelengths such as used here, the thermal emission is obvious as a strong turn-up in the spectrum relative to the star at longer wavelengths. Rivkin et al. (2005) called this turn-up the “thermal excess" and developed a method to model this excess and remove it. Thermal excess, γ, is defined as:

$$\gamma = \frac{R_\lambda + T_\lambda}{R_\lambda} - 1, \tag{3.1}$$

where R_λ is the radiance (W/m^2/μm) at a wavelength λ and T_λ is the thermal radiance (W/m^2/μm) at a given wavelength. To calculate the thermal excess observed, we first normalize the lunar spectra ($R_{n1.7}$) at 1.7 μm per the method of Rivkin et al. (2005).

Spectra of the Moon are inherently red, and removal of the red continuum is important for thermal excess removal. To remove the red continuum, we fit a straight line between 1.7 μm and 2.5 μm (Figure 3.12) while taking care not to include a 2 μm band due to the presence of lunar pyroxene, which is often strong in our spectra.

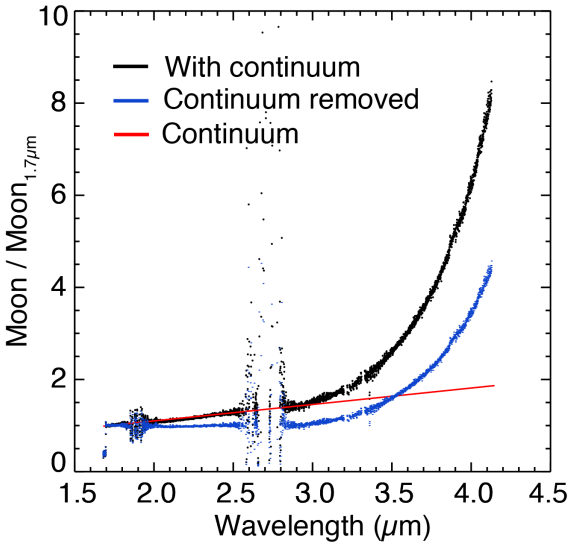

Figure 3.12: Removal of red slope continuum.

After fitting the continuum (R_{con}), we then calculate the measured thermal excess for each lunar spectrum by dividing the normalized spectrum by R_{con}, and subtracting 1 (Eq. 3.1). $R_{n1.7}$ contains both the reflected and thermal emission terms where R_{con} contains the modeled reflected radiance component making Eq. 3.1 become:

$$\gamma_{measured} = \frac{R_{n1.7}}{R_{con}} - 1 \tag{3.2}$$

In order to model the thermal excess represented by $\gamma_{measured}$, we model both the expected lunar radiance (which includes solar radiance) and thermal radiance. To model the lunar radiance (R_{model}), we multiply solar radiance (L_{solar}) by expected reflectance ($MI_{30,0,30}$) and then by the red lunar continuum (R_{con}) (Eq. 3.3):

$$R_{model} = MI_{30,0,30} * R_{con} * \frac{L_{solar}}{\pi}\ W/m^2/\mu m \tag{3.3}$$

The solar radiance is modeled using the known solar irradiance spectrum [ASTM E490-00a, 2014] divided by π to convert it to units of radiance. The expected reflectance of the Moon at the location observed is extracted from global albedo data collected by the Multiband Imager (MI) on the Kaguya spacecraft, corrected to the standard geometry of incidence angle 30°, emergence angle 0°, and phase angle 30° and at a wavelength of 1.7 μm. The retrieval of the MI reflectance value

is based on the latitude and longitude at which each spectrum was acquired. The Telescope Control System (TCS), however, reports the right ascension (RA) and declination (DEC) at which the telescope was pointed, which needs to be converted to latitude and longitude on the Moon. Because the Moon is constantly moving in the night sky, this transformation to latitude and longitude is dependent on the night of the observation, but also on the UTC time the data was acquired. To convert TCS reported RA and DEC to latitude and longitude, we generated a large look-up table of ephemeris using the JPL Horizons system. The JPL Horizons system is capable of taking in a latitude and longitude of a Solar System body and outputting the RA and DEC at specified times. For each night of observation spanning the UTC time the data was acquired, we ran JPL Horizons for a latitude range of 90°S to 90°N and longitudes at which the data was expected to be acquired. For pole to pole scans, this was typically 10°W to 10°E, but for the chords, that diagonally transected the Moon, we had to generate tables from 90°W to 90°E longitude.

In the tables, we then searched for the RA and DEC from the TCS and the UTC time it was acquired, providing us with the latitude and longitude of each spectrum. This method works well for a majority of the nights. However, on some observing nights, the TCS did not accurately record the RA and DEC. In these cases, the guider images from the SpEX guider/slit viewer are used to locate prominent features and their latitude and longitude is used to create the RA and DEC of our data for that night. This is then run through the same look tables to get the full latitude and longitude range of the data. At high latitudes and near the limb of the Moon, the latitude and longitudes have more scatter due to the spherical nature of the coordinate system. This, however, has no effect on the thermal removal, spectral shape, or abundance calculations.

Lastly, to model the thermal radiance (B_T), we use a rough surface thermal model similar to Bandfield et al. (2011). Because lunar data are affected by thermal radiance at wavelengths shorter than 3 μm, the removal of the red continuum above also removes some of the thermal component in the measured thermal excess. Due to this, the modeled thermal radiance must also have a continuum (C) removed at the same wavelengths as the data before the model can be used to find the correct thermal model for the data. The modeled thermal excess is given by Eq. 3.4:

$$\gamma_{model} = \frac{R_{model}+B_T/C}{R_{model}} - 1 \tag{3.4}$$

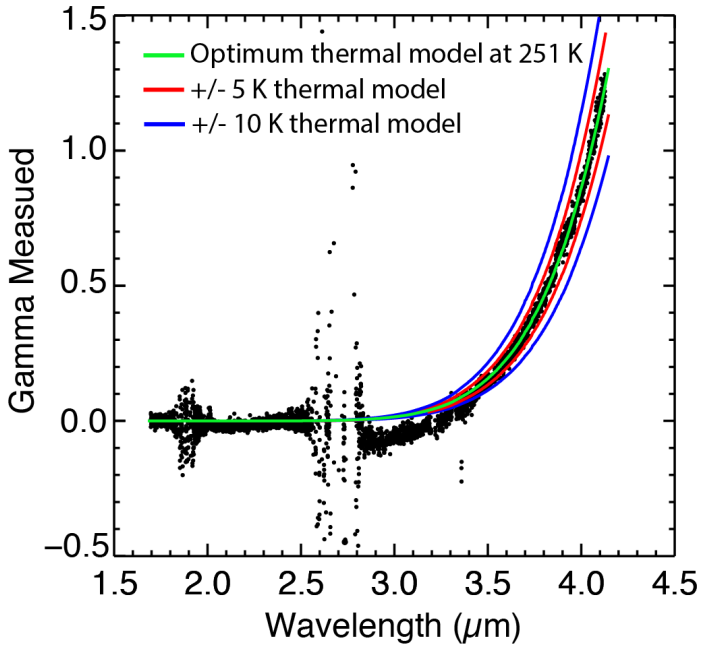

Figure 3.13: Longer wavelengths constrain which thermal model is selected.

Modeled thermal radiance is created using a range of surface roughness and temperatures between 200 to 400 K. This creates a library of model thermal excess.

With both the $\gamma_{measured}$ and the library of γ_{model}, we then subtract all models from the lunar $\gamma_{measured}$ and take the mean of the absolute value of the difference. The model that provides the minimum value is taken to be the appropriate γ_{model} (Figure 3.13). Selection of a thermal model that does not fit at longer wavelengths causes the long wavelengths to be either over or under corrected (Figure 3.14b). Figure 3.14b shows the reflectance using different thermal models, with the optimum model at 251 K and models that are ± 5 and 10 K. Applying thermal models that are a few Kelvin off has noticeably large effects at longer wavelengths, either causing an upturn or downturn of wavelengths longer than ~3.5 µm. Below 3.5 µm, however, the shape of the remaining spectrum is not greatly affected, including the shape of the 3 µm band.

Once the appropriate model has been found, we remove the optimum thermal model from our normalized continuum removed lunar spectra. We then scale the data to MI reflectance at the local lunar viewing geometry and introduce the continuum back into the reflectance spectrum (Eq. 3.5):

$$R_{Moon} = MI_{local} * \left(\frac{R_{n1.7}}{R_{con}} - \gamma_{model}\right) * R_{con} \quad (3.5)$$

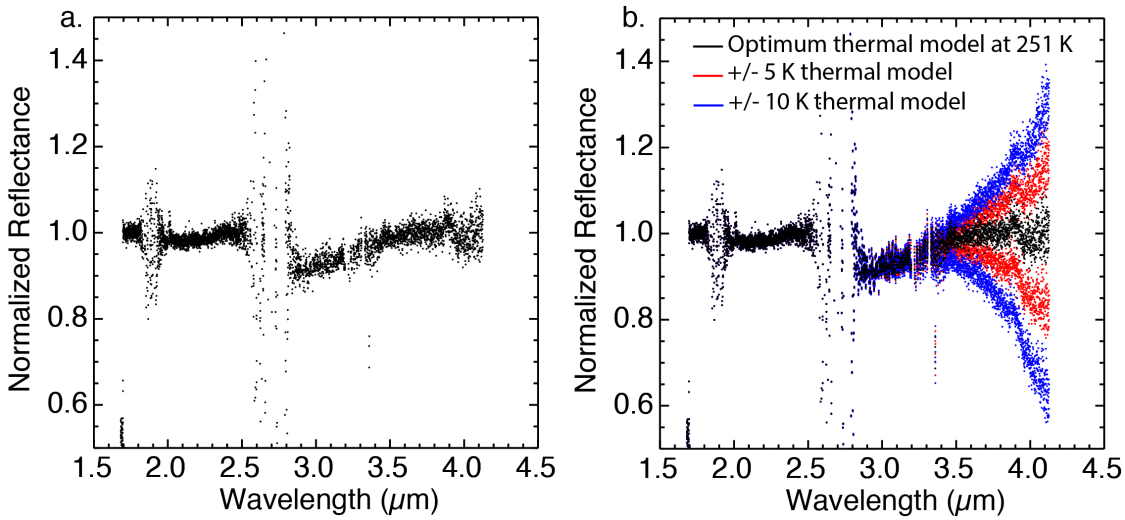

Figure 3.14: On left is the result of thermal removal with a continuum removed and normalized. On right is multiple thermal models removed that are ± 5 and 10 K from the optimum thermal model.

The spectra are now in reflectance (Figure 3.14a) and can be used for estimates of the abundance of total water.

3.7 Estimating the Abundance of Total Water

The abundance of H_2O has been estimated for decades using band depth in the infrared in carefully controlled samples where the thickness of the samples are well known. Milliken and Mustard (2005) was the first to develop a relationship for estimating the abundance of H_2O in remote sensing data. Later, Li and Milliken (2017) would go on to apply this to the Moon using empirical measurements of water bearing glasses to calibrate data to water concentration. We use two methods to estimate the abundance of H_2O: the Effective Single Particle Absorption Thickness (ESPAT) [Li, 2016; Milliken and Li, 2017] and band depth. ESPAT reduces the dependence on composition while band depth is more analogous to FTIR measurements. Unlike band depth, ESPAT improves the correction to abundance when strong albedo contrasts are present [Milliken and Mustard, 2005].

ESPAT is a function of the single scattering albedo (*w,* SSA, Figure 3.15), which is the probability that a photon will survive an encounter with a grain. This is calculated using work by Hapke (1981; 1993) [Li, 2016]. To calculate ESPAT from our reflectance data, we convert the reflectance spectra to SSA. In contrast with reflectance spectra, SSA spectra have many

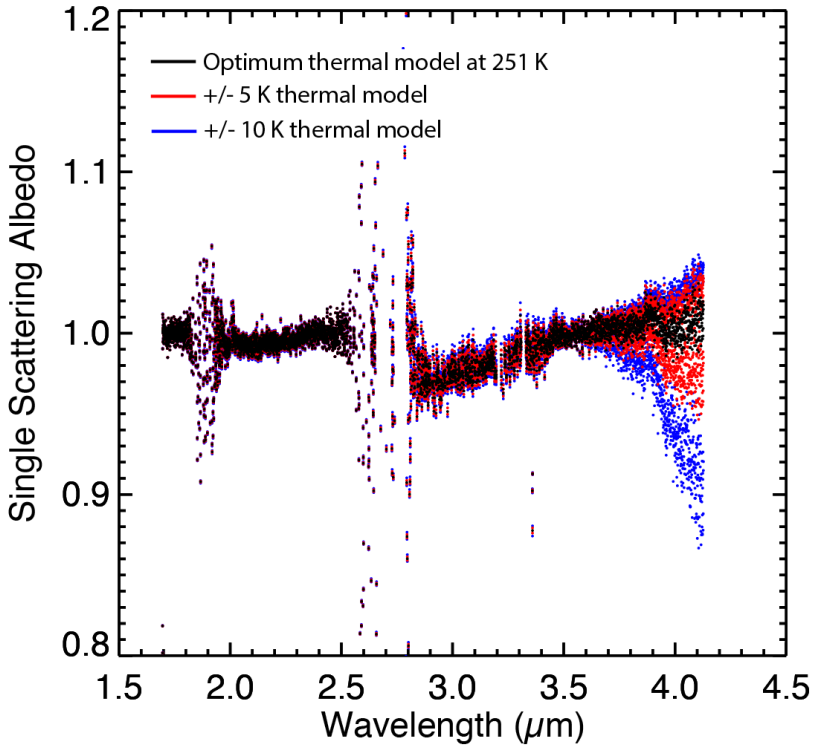

Figure 3.15: Conversion of reflectance spectra to single scattering albedo Also shown are the different thermal models (red and blue). The effect of incorrect thermal model selection does not greatly affect the shape or strength of the 3 μm band. The small effect incorrect models have is added uncertainty in the point to point scatter.

advantages; it accounts for variations in viewing geometry and it reduces the effects of multiple scattering and albedo and absorption strength correlations that are not related to the abundance [Li and Milliken, 2017]. Once the reflectance spectra have been converted to SSA spectra, we remove a continuum spectrum by fitting a straight line similar to the thermal excess removal, but in SSA units. This differs from Li (2017) who uses a single wavelength to define the point of the continuum and create a straight line continuum consisting on a single SSA value. With this method, it is possible to under estimate the continuum on the long wavelength shoulder of the 3 μm band causing negative abundances when there is little to no total water present. Fitting the SpEX data between 1.5 and 2.5 μm with care to avoid fitting any pyroxene band provides a red continuum more appropriate for the Moon. This method reduces the negative values when low abundances of total water are present providing a mean of zero. The continuum removed SSA is then used to calculate ESPAT (Figure 3.16):

$$ESPAT = \frac{1-w}{w} \tag{3.6}$$

After the calculation of ESPAT, we convert to abundance in ppm H_2O via:

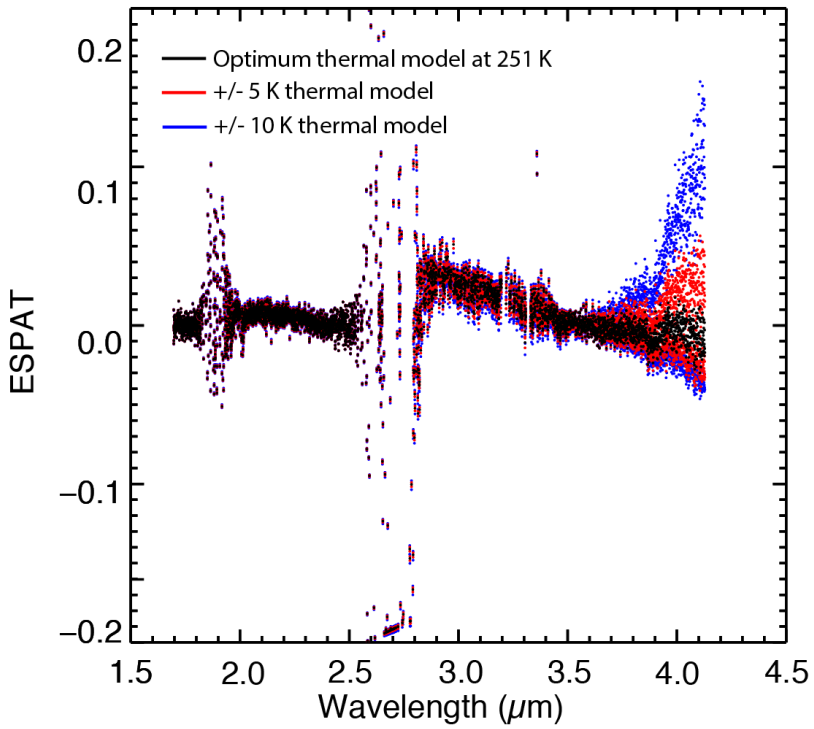

Figure 3.16: Conversion of single scattering albedo to ESPAT with the different thermal models (red and blue).

$$H_2Oppm = 0.8 \cdot ESPAT \cdot 10000 \quad (3.7)$$

Li and Milliken (2017) derived the empirical relationship to convert ESPAT to absolute total water content using a particle size of 60 to 80 μm. This particle range gives a conversion factor from ESPAT to wt.% of 0.5 (Figure 3.17a). From wt.% to ppm H_2O is another factor of 10000. However, Li and Milliken (2017) calculated this relationship at the band center of the 3 μm band which is at 2.86 μm (Figure 3.17a). From the IRTF, this wavelength is within the opaque region and therefore we use the average between 2.9 μm and 3 μm for the total water abundance of the 3 μm region. Instead of using 2.86 μm for the conversion of ESPAT to wt.%, we derive the empirical relationship at 2.95 μm providing a conversion factor of 0.8 (Figure 3.17b). When the abundance of total water is low or zero, the ESPAT calculation sometimes results in negative numbers. Negative numbers are interpreted to mean zero absorption.

The second method to derive total water abundances from the 3 μm band is by using the actual band depth with the band depth taken as the mean of the continuum removed data between 2.9 and 3 μm. Using the same lab experiments to derive ESPAT, we also derived a relationship for band depth to H_2O ppm (Fig 3.18) Eq. 3.8:

$$H_2Oppm = 2.534e4x^2 + 606.6x \quad (3.8)$$

where x is the band depth. The two methods will be compared to help inform us about the effect of composition on the strength of the 3 µm band and its variation.

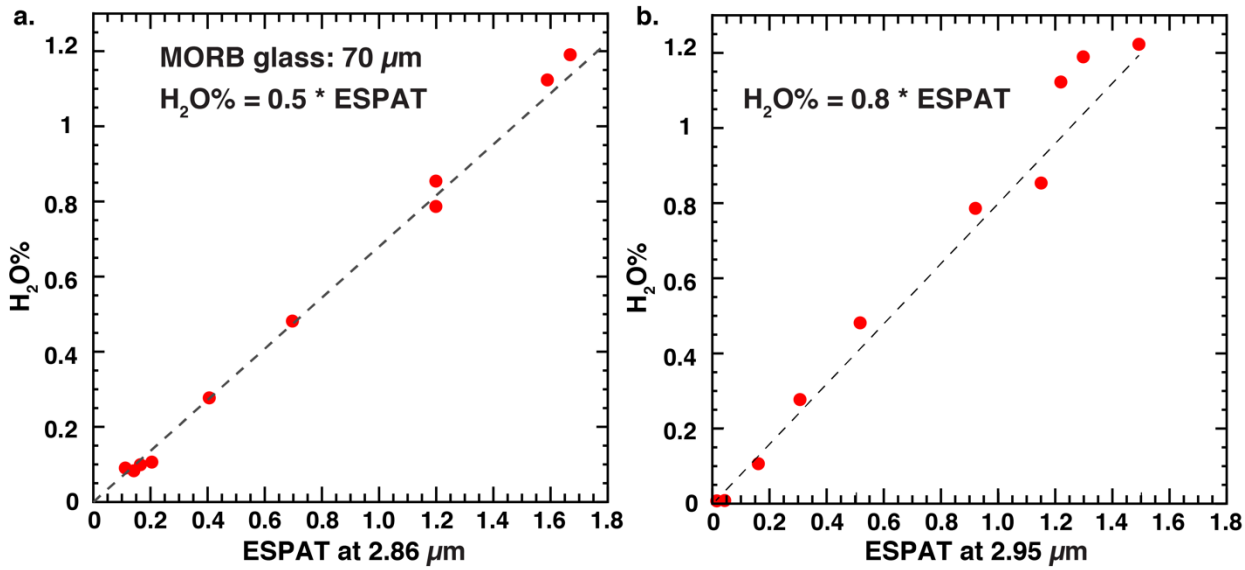

Figure 3.17: a) Empirical relationship between ESPAT and absolute content H2O in water-bearing terrestrial glasses (Li, 2017) at wavelengths 2.86 µm. b) The same relationship except at 2.95 µm. We use the relationship for 2.95 µm because from the ground the 2.86 µm region is opaque.

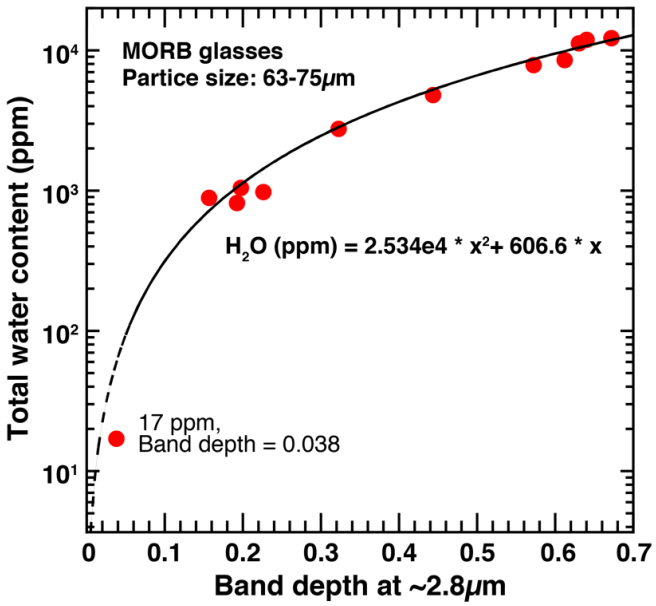

Figure 3.18: Empirical relationship between band depth and absolute content H_2O in water-bearing terrestrial glasses (Li, 2017).

3.8 Results

Figure 3.19 shows two examples of thermally corrected lunar IRTF SpEX data that have been continuum removed and normalized. The presence of total water in our spectra is indicated by a clear discontinuity between 2.5 and 2.9 µm (Figure 3.19 bottom). A pyroxene band is also observed at 2 µm and varies from a weak absorption (Figure 3.19 bottom) to a strong absorption (Figure 3.19 top). The data exhibit strong variations in depth of the 3 µm absorption. The depth of the band ranges from no absorption (Figure 3.19 top) to a strong 3 µm absorption (Figure 3.19 bottom). Many spectra show no total water absorption, like the top spectrum in Figure 3.19 indicating no detectable total water is present at the location where the spectrum was acquired. Due to the Earth's atmosphere, some regions of our spectra are low signal and are therefore, blocked out in this example. The region from 3.7 to 4.05 µm is due to N_2O in the atmosphere. In some spectra, like the one with a 3 µm absorption (bottom), the N_2O is corrected well while in others, like the top spectrum, N_2O is not correct well and causes scatter at the long wavelengths. The N_2O is typically not corrected well in spectra taken at warmer lunar temperatures, although the N_2O does not affect thermal modeling.

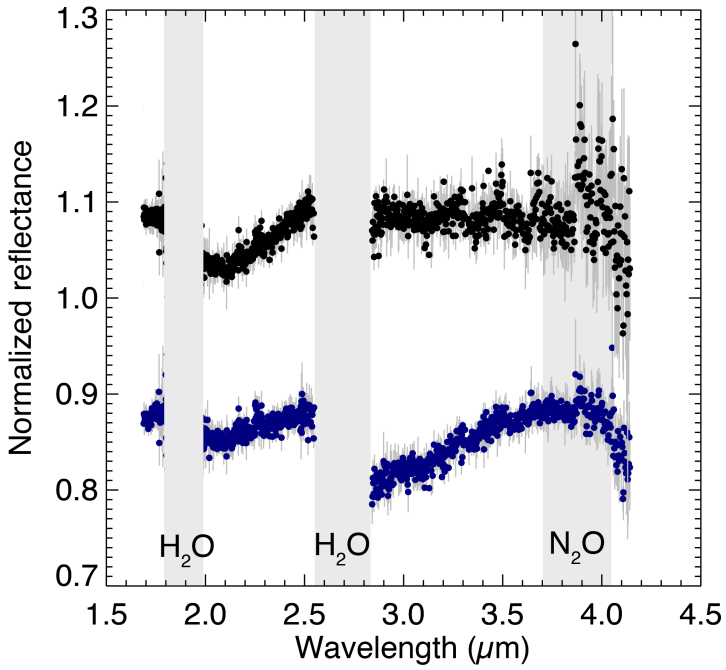

Figure 3.19: Normalized reflectance spectra after thermal radiation removal. The bottom spectrum shows a step down from 2.5 to 2.9 µm indicating the presence of total water. The top is an example of a flat spectrum with no total water. The gray bands are regions where atmospheric species absorb and cause low signal regions. A pyroxene band can also be seen at 2 µm in the top spectrum.

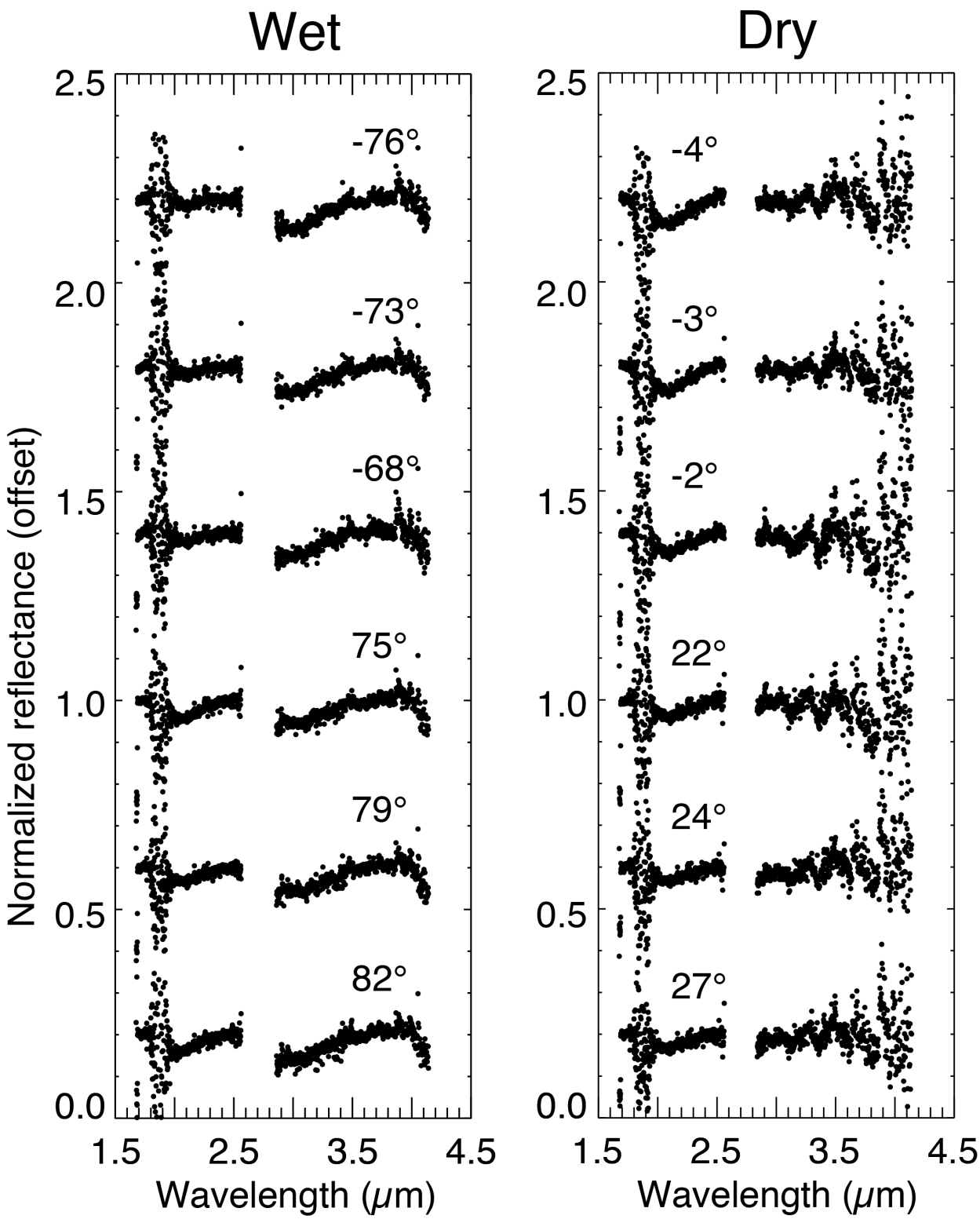

Figure 3.20: "Wet" and "dry" spectra from January 18th, 2019 observing run. The spectra show variations in the 2 μm pyroxene band along with variations in strength and shape of the 3 μm band.

Figure 3.20 shows more spectra demonstrating the absorption versus no absorption. In these spectra the pyroxene band at 2 μm can also be seen to vary. Closer investigation of the "wet" spectra in Figure 3.20 shows two different band shapes. The northern bands have a band minimum somewhere in the opaque region of the 3 μm band. However, the two most southerly bands appear to have a band minimum at 3 μm. The shape of 3 μm bands in asteroids was studied by Takir and Emery (2012) using SpEX. In their work they developed four 3 μm spectral groups based on the shape of the band; sharp, Ceres-like, Europa-like, and rounded. The spectral shapes of the 3 μm bands shown in Figure 3.20 can be classified into these groups. The northern spectra can be classified as having a sharp 3 μm band while the southern ones are rounded. The sharp versus rounded spectral shapes may provide information regarding which species, OH or H_2O, is responsible for the 3 μm absorption.

The abundance of total water as a function of lunar latitude and lunar time of day is shown in Figure 3.21 for both the ESPAT and band depth methods. The size of the points represents the abundance of total water, larger points indicate more total water while the smallest points have approximately zero ppm H_2O. Black indicates pole to pole scans and grey indicated chord scans that transected the Moon on a diagonal (Figure 3.6). When two chords intersect, it does not indicate

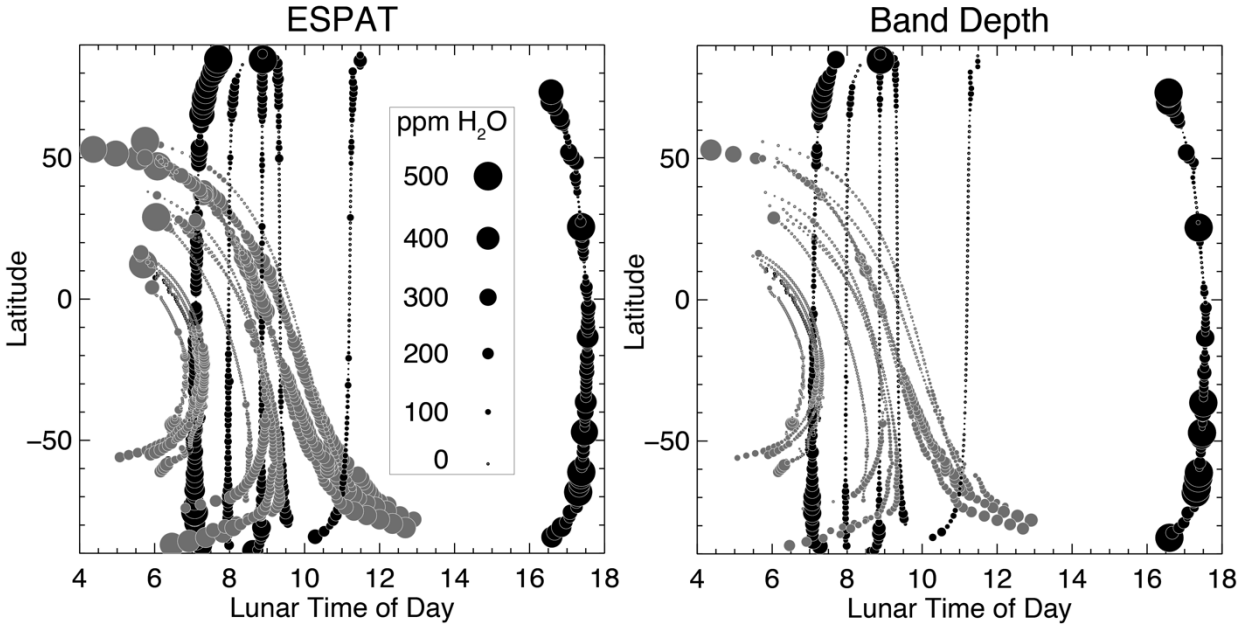

Figure 3.21: Chords plotted as lunar time of day vs. Latitude for both ESPAT and band depth methods. Symbol size is proportional to the abundance of total water. The anomalous high abundance at ~0° latitude and ~0830 lunar time of day is believed to be high total water abundances at and around Copernicus crater.

they are at the same location, just that they have the same local time of day. For the sake of viewing diurnal effects, the abundances are limited to a maximum of 500 ppm. Minimum abundances are approximately zero. Along each observed chord, as a function of latitude, there are strong variations in total water concentrations. The minimum water observed occurs at low-northern latitudes at mid-morning to noon hours. Maxima for each chord occurs at high latitudes with increased abundances in the south compared to the north. Diurnal variations are seen across constant latitude in Figure 3.21. With increasing time of day, there is a decrease in abundance towards local noon. There is an asymmetric trend about the equator that favors the southern latitudes with higher total water abundances.

Figure 3.22a plots the abundance versus latitude where each color represents a pole to pole observation and its time from local noon. The two pole to pole observations, in blue and purple, were acquired at the furthest time from local noon and show the highest abundances across all latitudes with a weak latitude dependence. The four other pole to pole observations show a strong latitude dependence. The sharp drop from morning, 4.8 hours before local noon (blue) to 3.1 hours before local noon (yellow), is also seen in this plot. In Figure 3.22b, we plot the abundance of total water from ESPAT versus time of day. The latitudes were binned into 10° increments from 90°S to 90 °N and the abundance within each 10° wide bin was averaged and plotted at the average time

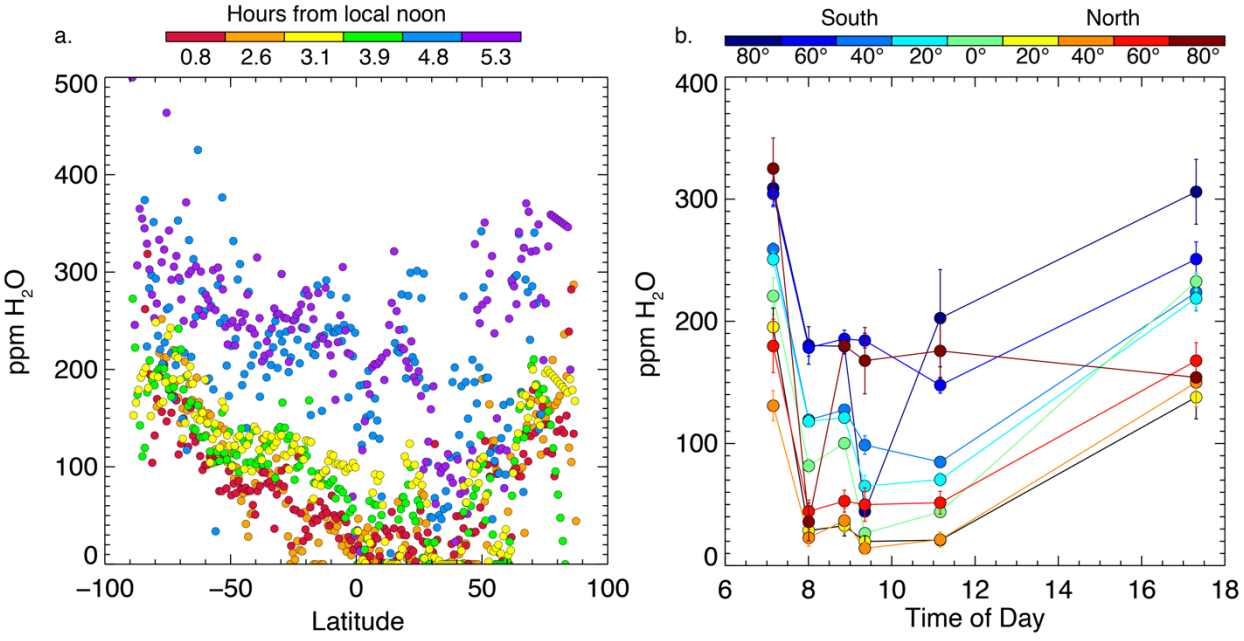

Figure 3.22: Total water abundance in ppm H_2O plotted against latitude (a) and time of day (b) for the pole to pole observations.

of day for each pole to pole observation. A sharp drop is observed at all latitudes from 07:00 to 08:00. After that, the abundance stays relatively constant at each latitude, except for an anomalous point for 80° – 90° N at ~09:00. The evening shows an increase in abundance again.

On the Copernicus chords (Figure 3.23a) there is an anomaly in abundance around ~0 degrees latitude and local time ~08:30 am; this is due to the chord passing through Copernicus

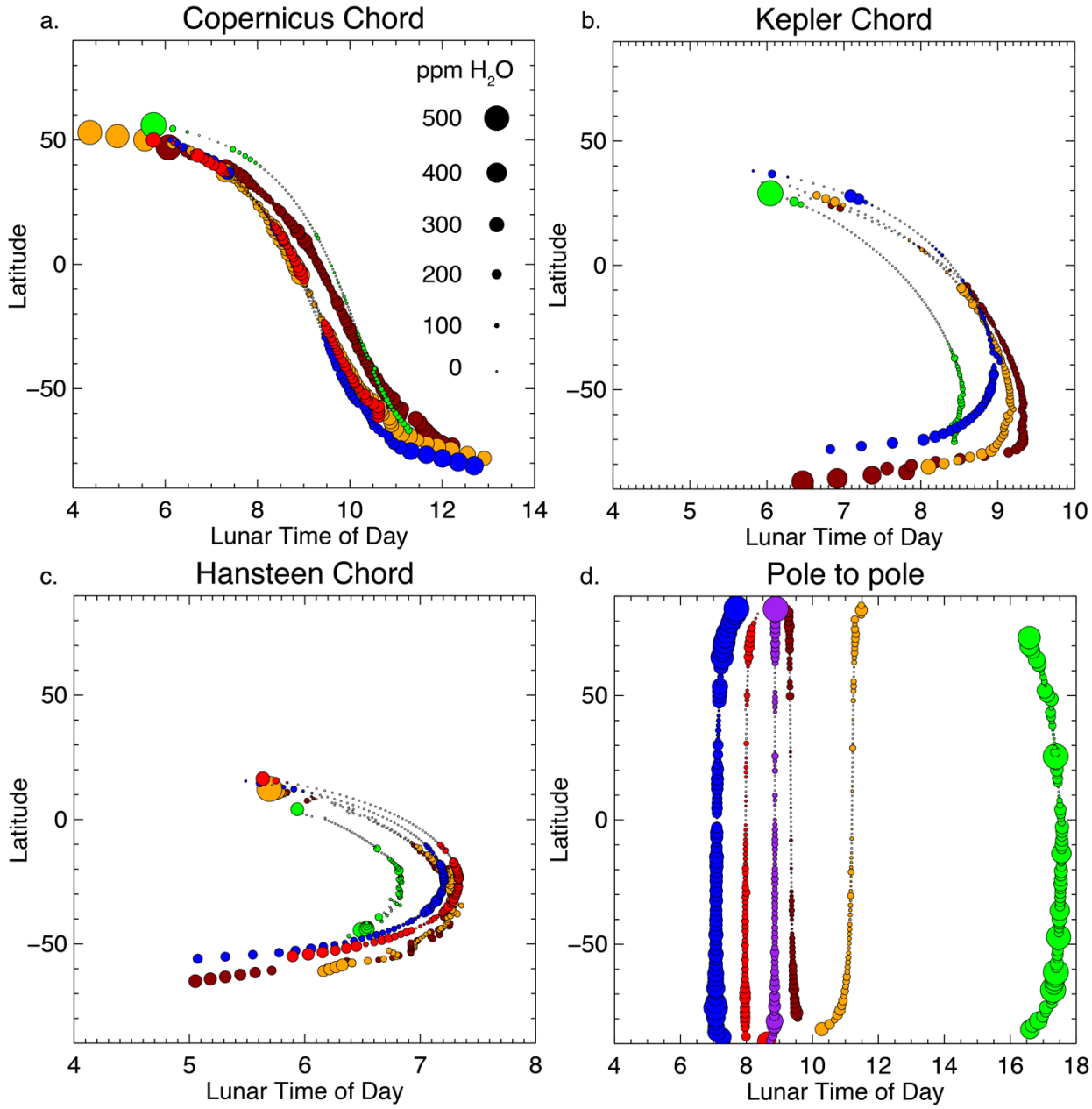

Figure 3.23: Chords plotted as lunar time of day vs. latitude using the ESPAT values. Point size represents abundance with larger points being more abundant.

crater. Copernicus has shown an enhanced 3 μm absorption in M^3 data [Li and Milliken, 2017]. The same location viewed at different lunar times of day show lower abundances, indicating a diurnal variation occurring at Copernicus crater. On the Hansteen chords (Figure 3.23c) we observe another anomaly at ~07:00 and latitudes 20° to 30°S. This is due to the pyroclastic deposit just west of the Humorum pyroclastic deposit which was shown by Li and Milliken (2017) to have higher abundance of total water in M^3 data.

These plots show a strong diurnal variation at mid-southern latitudes, and a weaker but still present diurnal variation at low latitudes and mid-northern latitudes. The high latitudes also show a weak diurnal variation, but at later local times than at low- and mid-latitudes. Comparisons between ESPAT and band-depth derived total water abundance reveals that the diurnal variation appear roughly the same for both methods. Water abundances derived from band depth show higher abundances in general compared to the ESPAT method. The ESPAT method, however, displays more variation in abundance along the chords, especially those that were taken during early morning or late evening hours.

3.9 Discussion

Using thermally corrected (based on long wavelengths) SpEX data, we observe variations with latitude, time of day, and composition. The variations in the 3 μm band after strongly constraining thermal models indicate that they are due to changes in total water abundance and not to thermal infill of the band. This result is in agreement with a number of studies [Sunshine et al., 2006; Li and Milliken, 2017; Wolher et al., 2017; Grumpe et al., 2019], which also observe variations in the 3 μm band in spacecraft data. The variation indicates that the species responsible for the 3 μm band are undergoing temperature driven processes, such as migration and diffusion, depending on the species.

One implication of the variation being due to changes in total water abundance is the activation energy of OH and H_2O. Activation energy is the energy needed for a chemical reaction. In the context of total water, it is the amount energy required for H_2O to break its bonds from surface material and be released from the lunar surface. If no variation was observed in our data set, it would imply the activation energies are high and require high temperatures for H_2O to be released. However, variations were observed, and this implies that the activation energies are

actually low enough such that lunar temperatures can generate enough energy to reach the activation energy allowing for migration of H_2O.

The observed diurnal variations are mostly in agreement with Li and Milliken (2017), but with some differences. First, the abundances we measure using ESPAT and band depth are lower than those of Li and Milliken (2017) by a factor of about 1.5. This difference could be due to the uncertainty in thermal modeling M^3 data. The higher abundances could indicate that the model used by Li and Milliken (2017) selects temperatures slightly higher than the actual temperature of the surface and therefore artificially creates a stronger 3 μm band. We showed that even ± 10 K can make the difference between no absorption to a large absorption in M^3 data and, without the long wavelengths, there is no certainty in the thermal removal.

The second difference is the asymmetry between the northern and southern hemispheres. Li and Milliken (2017) observe higher abundances in the northern hemisphere while we observe higher abundances in the southern hemisphere. A possible explanation for this is the lunar time of day at which the M^3 observations were acquired. The southern observations were taken slightly closer to lunar noon than the northern observations, possibly creating the asymmetry seen in M^3 data. The asymmetry in our data cannot be explained by different acquisition times, especially for the pole to pole observations. Another possible explanation is composition. Across our pole to pole scan we traverse through mare and highland regions with most of our northern observations in mare regions and our southern observation in highland regions. Our results, therefore, agree that highland material retains more total water than mare material [Wohler et al., 2017; McCord et al., 2011].

Due to a majority of the data being collected before lunar noon, we cannot comment on the symmetry of abundance between dawn and dusk terminators, but we observe abundances between 07:00 and 17:00 are similar. This is in contrast to Li and Milliken (2017) who see more total water in the morning than in the afternoon. Again, this could be due to the time of day the data was acquired with M^3, with the afternoon observations begin closer to noon than the morning observations. We are, however, in agreement with Wohler et al., (2017) and Grumpe et al., (2019) who see similar abundances between morning and afternoon using their version of thermally corrected M^3 data. Unfortunately, Wohler et al., (2017) and Grumpe et al., (2019) did not provide

estimates of total water in absolute concentrations and therefore, we cannot compare our abundances to their data.

The variations in total water abundance with latitude is due to changes in average local temperature. Our observations agree with Li and Milliken (2017) that most of the diurnal variations occur in the mid-latitude ranges and that there is weak, to no, variation at high latitudes. The increased abundance at high latitudes may indicate the surfaces ability to retain and accumulate more total water due to the lower temperatures. Latitudinal variations also provide information regarding the migration of total water from low latitudes to higher latitudes, which could also be supplying the polar cold traps [Arnold, 1979; Watson et al., 1961].

Our observations also show some anomalous total water abundances at Copernicus crater similar to Li and Milliken (2017). However, they did not observe the diurnal variation in Copernicus. Li and Milliken (2017) suggests the anomalous abundance is due to endogenic water within the lunar grains. However, the diurnal signal we observe cannot be due entirely to internal water. Another possibility is that the chord observations did not alway pass directly through the enriched areas of Copernicus. Humorum pyroclastic deposit also shows anomalous total water abundances in both our observations and those of M^3. However, unlike Copernicus, no diurnal signals are observed at Humorum. Therefore, we attribute the higher abundances to endogenic water contained in the glass beads of the pyroclastic deposit that is trapped and thus unable to vary with lunar time of day and temperature.

Observations conducted by the Deep Impact spacecraft, presumably using thermally corrected data constrained by their long wavelengths (though the correction is not provided), revealed a temperature dependence [Sunshine et al., 2009]. However, they only acquired data of a quarter of the Moon at two different lunar days and, therefore, cannot demonstrate a true diurnal variation, additionally they did not provide estimates of total water abundance based on their spectra. They do, however, suggest that the observed variation is due to migration of H_2O on the lunar surface. If H_2O is the migrating species, it will hop along temperature gradients to cooler locations. Eventually the H_2O will reach a cold trap and remain stuck over a lunation and require outside forces to continue migrating. This could be a possible source of H_2O to permanently shadowed regions and supply the polar ice deposits [Arnold, 1979]. H_2O, however, is unstable on the surface at lunar temperatures [Hibbitts et al., 2011]. If H_2O is formed on the surface via

recombinative desorption, then it is not expected to survive a lunar day at low- and mid-latitudes. If however, the migrating species is metastable OH [Tucker et al., 2019, Farrell et al., 2017, Starukhina, 2006], then the variations seen in the 3 μm band are due to H diffusing through the lunar surface and temporarily forming OH bonds and degassing as H_2 through recombinative desorption. This process is highly dependent on temperature; thus with increasing latitude and decreasing temperature, there is an accumulation of H towards the poles as the temperatures are not high enough for recombinative desorption [Starukhina, 2006; Tucker et al., 2019].

Hendrix et al., (2019) also observed a diurnal variation in the far ultra-violet (FUV) water ice band ratio using Lyman Alpha Mapping Project (LAMP) data. They attribute the diurnal variation to the migration of H_2O (Figure 3.24). If their signal is due to H_2O, then the activation energies are high. However, their diurnal effect occurs right before and after local noon. Our results show a sharp drop in total water abundances at early morning hours and weak to no variation just before noon. We are unable to separate OH from H_2O at 3 μm; however, it is possible we are observing H_2O migrating [Sunshine et al., 2009] in the early morning hours, and Hendrix et al., 2019 is instead seeing the destruction of metastable OH via diffusion of H [Tucker et al., 2019; Farrell et al., 2017]. This would indicate that the activation energy is low for H_2O, but relatively high for metastable OH.

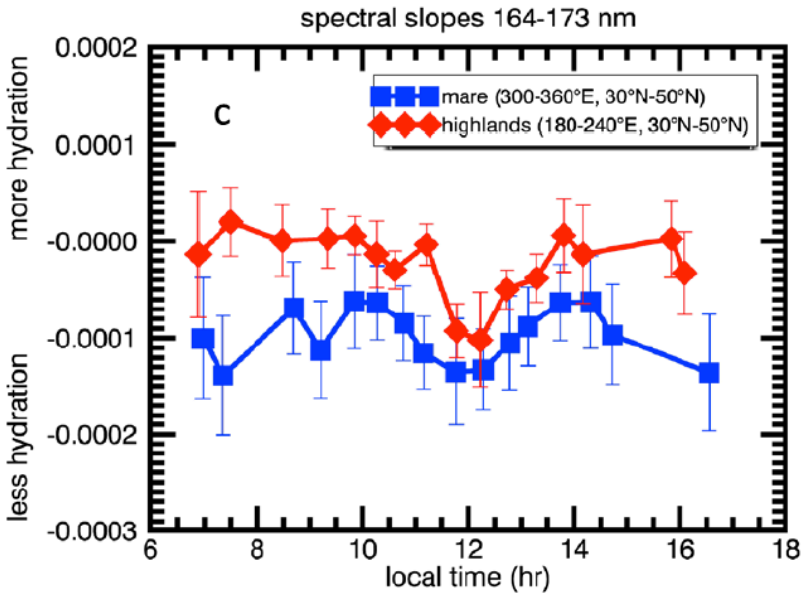

Figure 3.24: Diurnal signature in FUV LAMP data for mare and highland regions. The diurnal signal is attributed to H_2O if it behaves like water ice in the FUV. The diurnal signal is seen near local noon. Hendrix et al., 2019.

Currently it is not known if H_2O is migrating on the lunar surface or if the variations are caused by the diffusion of H. However, the spectral shapes observed in our data may provide information of the species present. The two shapes observed are sharp and rounded 3 μm bands as defined by Takir and Emery (2012). The rounded bands have band minima at 3 μm, which could be an indication of H_2O. Unfortunately, OH attached to metal cations can also produce band minimums near 3 μm, so the 3 μm band is ambiguous when trying to detect H_2O. The detection of H_2O will be investigated further in the next chapter.

3.10 Conclusions

We used a new data set from the groundbased IRTF to determine the variability of the 3 μm total water band using wavelengths beyond 3 μm to strongly constrain thermal models. We demonstrated that data limited to less than 3 μm can show apparent variations in the total water band with small errors in thermal model temperatures, especially at higher surface temperatures. We showed that thermal emission removal does not remove or enhance the observed 3 μm band when using the longer wavelength to constrain the thermal models. We showed that the 3 μm band does vary with time of day, temperature, latitude, and composition. Our results show that total water is dynamic on the lunar surface which has large implications for ongoing surface processes.

The variations and abundances we observe are similar to those reported by Li and Milliken (2017) except that we derive slightly lower abundances and observe higher abundances in the southern hemisphere than the north. The higher abundances in the south could be due to observing more highland regions than mare, which is in agreement with observations of Wohler et al., (2017) and Grumpe et al., (2019). However, we cannot compare our abundances to Wohler et al., (2017) and Grumpe et al., (2019) as they did not provide absolute abundances of total water. Observations of diurnal variability by Hendrix et al., (2019) show the variability occurring near local noon while our diurnal signal occurs in the early morning hours. We interpret this as H_2O leaving the surface in the morning hours while LAMP observed OH.

Our results indicate that there is a migrating species on the surface of the Moon. The species could be H_2O or H diffusing and forming metastable OH. Which species is responsible for the variability of the 3 μm band, however, cannot be distinguished using 3 μm observations. Instead

new observations at longer wavelengths are needed to separate OH and H_2O and is the subject of the following chapter.

CHAPTER 4: DETECTION OF MOLECULAR WATER ON THE ILLUMINATED MOON WITH SOFIA

Abstract

For a decade the lunar surface has been known to host hydroxyl (OH) and possibly molecular water (H_2O) [Pieters et al., 2009; Sunshine et al., 2009; Clark, 2009]. Distinction between OH and H_2O from spacecraft measurements at 3 μm, however, is difficult due to their similar spectral properties. Currently, the only direct measurement of H_2O on the lunar surface is of ice deposits within permanently shadowed regions [Li et al., 2018]. On the illuminated Moon, Hendrix et al., (2019) suggests the detection of molecular water using far ultra-violet observations of the Moon, however, they could not rule out the possibility of their observed diurnal signal being due to OH.

We have developed a new approach for unambiguous detection of the water molecule on the illuminated lunar surface. At 6.07 μm the fundamental H-O-H bend of H_2O is exhibited and is strictly due to H_2O without any contribution by OH. However, there are currently no spacecraft capable of observing this feature on the Moon and it cannot be conducted from groundbased telescopes because Earth's atmosphere is opaque at 6 μm. The only observatory currently capable of 6 μm observations of the Moon is the Stratospheric Observatory For Infrared Astronomy (SOFIA). SOFIA flies at 13.7 km, above a majority of the Earth's atmosphere allowing for 6 μm observations.

Using SOFIA, we conducted the first observations of the Moon at 6 μm on August 30th, 2018. Observations at high southern latitudes reveal the presence of a strong 6 μm emission feature due to H_2O. The abundance of H_2O present on the surface ranges from 243 to 725 ppm H_2O, which is calibrated to 6 μm laboratory measurements of water-bearing glasses with known H_2O concentrations. Comparison of the lunar 6 μm feature to 6 μm features seen on asteroids and in meteorites show similar spectral shapes. An estimated temperature of 310 K is used to determine that 10% of a monolayer could cover the lunar surface. At high southern latitudes, we estimate that ~96% of the detected H_2O is trapped within the lunar grains and unable to migrate. These observations with SOFIA are the first direct detection of H_2O on the lunar surface.

4.1 Introduction

The chemical state of hydrogen on the Moon and how it interacts with the lunar surface is at the forefront of lunar science and understanding ongoing surface processes, the lunar interior, and future resources. Part of the hydrogen story is determining the degree to which H is bound in molecular water (H_2O), if at all. Several studies have been dedicated to characterizing H [Wohler et al., 2017; Milliken and Li, 2017; Li and Milliken, 2017; Li et al., 2018; Daly and Schultz, 2018; Bandfield et al., 2018; Benna et al., 2019; Zhu et al., 2019] and are a testimony to the importance of understanding water on the Moon. The discovery of the 3 μm hydration band on the lunar surface [Pieters et al., 2009; Sunshine et al., 2009; Clark, 2009], left unanswered questions regarding which species is present and their relative abundances. The 3 μm band indicates the presence of OH, H_2O, or OH + H_2O (termed "total water" in the FTIR community that studies hydration in geologic materials using infrared spectroscopy [Stolper, 1982; McIntosh et al., 2017]), but cannot be used to decipher which is present and their relative abundance. Speciation of the H compound present is important for studying the supply of H to polar regions, *in-situ* resource utilization, and surface chemistry processes, such as production, retention, and storage of H_2O on the surface of the Moon and other airless bodies.

To date, the presence of H_2O on the lunar surface is uncertain as all assertions that H_2O has been detected have valid alternative explanations, such as the presence of hydroxyl (OH) mimicking the spectral shape of H_2O. No unambiguous observations of H_2O on the sunlit portion of the lunar surface has been reported. In order to confirm or refute the presence of H_2O, new techniques are needed. Starukhina (2001) pointed out that H_2O possesses a third fundamental vibration at ~6 μm and suggests observations at 6 μm will provide a definitive detection of the water molecule if it is present on the lunar surface. In this chapter we report observations of the Moon in the 6 μm region using the airborne NASA/DLR Stratospheric Observatory For Infrared Astronomy (SOFIA). Analysis of the data reveal the presence of a strong emission feature near 6 μm that we attribute to the presence of H_2O on the lunar surface. Next we derive H_2O abundances from our emission spectra and discuss the possible migration and storage of water on the Moon. This remote observation is the first direct and unambiguous detection of the water molecule on the lunar surface.

4.2 Background

There are two main sources of hydration on the Moon, the solar wind [Hapke, 1965; Zeller et al., 1966; Starukhina, 2001; Dyar et al., 2010; Ichimura et al., 2012] and micrometeoroid impacts [Liu et al., 2012; Daly and Shultz, 2018]. The solar wind consists of protons that are constantly bombarding the illuminated lunar surface. Solar wind protons upon interacting with the lunar surface can either be reflected or implanted into the lunar soil. During implantation, a proton can penetrate 5 to 10 nm into lunar grains [McCord et al., 2011] while destroying the crystal structure and leaving crystallographic defects in the grains. Once slowed or neutralized, protons may diffuse out of the grain as H or H_2 [Farrell et al., 2015], react with the abundant oxygen in lunar minerals to form OH [McCord et al., 2011; Farrell et al., 2015; Ichimura et al., 2012; Mattern et al., 1976; Siskind et al., 1977; Guermazi et al., 1987; Gruen et al., 1975; Bradley et al., 2014], diffuse out forming metastable OH at available O bonds along its diffusion path [Tucker et al., 2019], or form H_2O at local noon temperatures via recombination desorption ($OH + OH \rightarrow O + H_2O$) of native OH [Poston et al., 2013]. However, even at the maximum lunar temperatures recombination desorption is relatively ineffective in producing water [Hibbitts et al., 2011; Poston et al., 2015; Jones et al., 2018]

The other source of lunar hydration is micrometeoroid impacts. It was proposed that surfaces rich in hydroxyl from prior solar wind irradiation, such as the lunar surface, could produce water during micrometeoroid impacts due to the high temperatures produced during the impact [Bennett et al., 2013]. Zhu et al., (2019) simulated meteoroid impacts and verified that a surface irradiated with hydrogen (in their case deuterium), which is then exposed to laser irradiation, simulating the high temperatures of micrometeoroid impacts, does produce H_2O, as anticipated by the temperature programmed desorption experiments [Poston et al., 2015]. Some of this water may be captured into a product formed from micrometeoroid impacts which is agglutinate glass. It has been shown that agglutinate glasses are host to large amounts of H, equivalent to 27 – 470 ppm H_2O [Liu et al., 2012]. As agglutinate glasses make up a large fraction of lunar soil (about 30 wt. % [McKay et al., 1991]), these impact glasses are potentially an abundant reservoir of OH and H_2O [Liu et al., 2012]. Further, a wet impactor could deliver 30% of its indigenous water to the Moon that could be captured in the resulting impact generated glasses [Daly and Schultz, 2018].

So there are two ways for meteorites to introduce OH or H_2O to the Moon, production resulting from the high temperatures of the impact or by delivering the impactor water to the resulting impact glasses. Supporting micrometeoroid production or delivery is the detection of spikes of OH and/or H_2O in the lunar exosphere during periods of annual meteoroid streams by the Neutral Mass Spectrometer (NMS) onboard the Lunar Atmosphere and Dust Environment Explorer (LADEE) spacecraft [Benna et al., 2019].

Although it has been shown that H_2O could be produced on the lunar surface by these high temperature impact events, there remains a lack of direct observational evidence. Two recent studies interpret their data in such a way to suggest the presence of H_2O on the lunar surface. Hendrix et al. 2019 suggest detection of H_2O using far ultra-violet (FUV) measurements with the Lyman Alpha Mapping Project (LAMP) on the Lunar Reconnaissance Orbiter (LRO) assuming adsorbed H_2O behaves like water ice in the FUV. LAMP is a FUV spectrometer operating in the 57.5 – 196.5 nm wavelength range aimed at studying the lunar atmosphere and looking for polar ice in permanently shadowed regions (PSRs) [Gladstone et al., 2010]. LAMP detects water ice based on a ratio of reflectance measured between 155.57 – 189.57 nm and 129.57 – 155.57 nm, which samples a FUV water ice band [Hayne et al., 2015]. When water ice is present, the ratio is expected to be high [Gladstone et al., 2012]. Using this method, water ice has been detected in PSRs at both lunar poles [Gladstone et al., 2012]. Dayside surface observations with LAMP reveal FUV spectral variations with latitude, local time, composition, and soil maturity [Hendrix et al., 2012 & 2019]. A diurnal signal was observed in both highland and mare regions at mid-latitudes with a sharp drop in the ratio of off-band/on-band near local noon [Hendrix et al., 2019]. They suggest the diurnal signal is consistent with <1% monolayer of H_2O, if absorbed H_2O behaves like water ice in the FUV. However, the variation could be due to OH as there is no data on the behavior of adsorbed H_2O in the FUV.

Using data from the Chandryaan-1 Moon Minerology Mapper (M^3), an infrared spectrometer that provided global coverage of the Moon, Li et al., (2019) detected hematite on illuminated surfaces near the lunar poles. Hematite is commonly found on Earth, Mars, and asteroids as a result of aqueous alteration and is readily formed if H_2O is present [Li et al., 2019]. The maps of hematite also spatially match maps of total water using the M^3 3 μm total water band from Li and Milliken (2017). Because of the nature of hematite and its correlation to the total water

maps, Li et al., (2019) infer that for hematite to be present on the lunar surface, H_2O must also be present to oxidize surface iron. However, detection of this is not a detection of hematite implies the presence of H_2O but is not a direct detection of H_2O on the lunar surface.

Lastly, in the previous chapter we investigated the underlying cause of the variation in the 3 μm band as observed by M^3 using groundbased IRTF data and concluded the variations are due to changing total water abundance. There are two hypotheses to explain variation in total water: migration of molecular water along temperature gradients on the lunar surface [Watson et al., 1961; Sunshine et al., 2009] and diffusion of H through grains temporarily forming metastable OH [Tucker et al., 2019; Farrell et al., 2017]. Molecular water is less thermally stable than OH on the surface [Hibbitts et al., 2011], which allows it to migrate and potentially supply the known water ice deposits at the lunar poles [Watson et al., 1961; Li et al., 2018] or participate in chemical reactions, such as the formation of hematite [Li et al., 2019]. OH, however, is not mobile [Hibbitts et al., 2011] and may provide a long term sink for hydrogen in the lunar regolith.

However, as pointed out in Chapter 3, water and hydroxyl cannot be unambiguously distinguished by the hydration band at 3 μm. The 3 μm band is characteristic of the symmetric and asymmetric stretching vibration of the O-H bond, which can be produced by OH attached to any metal cation (X), or to H [Stolper, 1982]. With OH attached to a variety of metal cations, such Si, Al, Mg, Ti, and Fe [Heiken et al., 1991], the 3 μm band minimum caused by X-OH may shift to

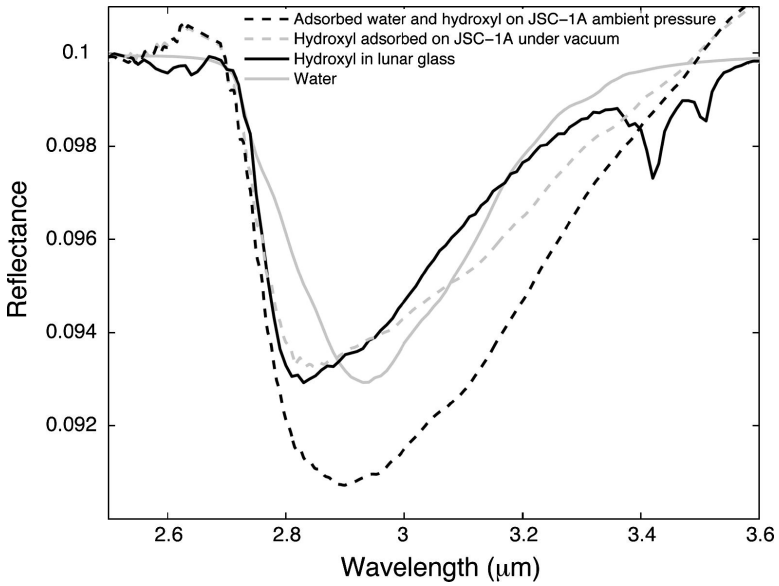

Figure 4.1: Comparison of various physical states of water at 3 μm. Major spectral differences between the states are observed beyond 3 μm. From Hibbitts et al., 2011.

longer wavelengths and the band width may broaden based on different bond strengths [King et al., 2004; McIntosh et al., 2017; Starukhina, 2001]. The shifting band minimum and band broadening of X-OH can mimic the spectral shape of H_2O at 3 μm. Figure 4.1 demonstrates the shape of the 3 μm band of various physical states of H_2O and OH. Currently, the shape of the 3 μm band due to OH attached to metal cations cannot be predicted and the use of a 3 μm band minimum, depth, shape, or width is therefore not useful for determining the speciation of water [Stolper, 1982; Starukhina, 2001]. For this reason, unambiguous detection of H_2O on the lunar surface has remained elusive.

Detection and quantification of molecular water, however, has been carried out for decades using Fourier Transform InfraRed (FTIR) spectroscopy in thin section [Bartholomew et al., 1980; Glew, and Rath, 1971; Newman, et al., 1986; McIntosh et al., 2017]. The FTIR community does not use absorption at 3 μm for detection of molecular water but instead uses 6.07 μm, which is the fundamental H-O-H bending vibration of H_2O (Figure 4.2) [Bartholomew et al., 1980; Glew and Rath, 1971; Newman, et al., 1986; Thompson, 1965; Stolper, 1982; King et al. 2004, McIntosh et al., 2017; Starukhina, 2001; Daly and Schultz, 2018]. This feature can only be created by H_2O, as no other common lunar materials exhibit a 6 μm feature. Starukhina (2001) pointed out that the 3 μm band is ambiguous, and suggest remote measurements at 6 μm would "prove" the presence of H_2O by optical spectroscopy in reflectance or emission spectra.

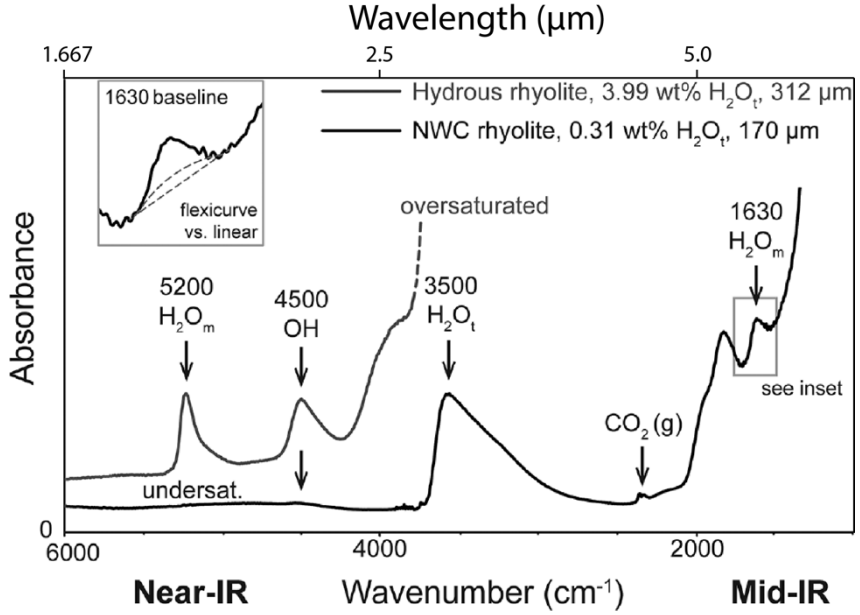

Figure 4.2: FTIR spectra of hydrous rhyolite glasses showing the multiple OH and H_2O spectral bands. The 6 μm band of interest for this study is at 1630 cm-1 and is shown in the inset. [McIntosh et al., 2017]

4.3 6 μm Observations in Samples and on Planetary Bodies

The 6 μm emission and absorption band has been detected in both lunar and meteorite samples. Apollo samples, as measured by the NASA Reflectance Experiment LABoratory (RELAB) at Brown University using FTIR spectroscopy, exhibit a 6 μm band in conjunction with the 3 μm total water band (Figure 4.3a). Although the detected water is due to terrestrial water contaminating the sample, the presence of the 6 μm band in Apollo samples demonstrates the ability of lunar soils to exhibit this spectral feature if H_2O is present. At the Laboratory for Spectroscopy under Planetary Environmental Conditions (LabSPEC) at the Johns Hopkins University Applied Physics Laboratory (JHU APL), Takir et al., (2019) measured carbonaceous chondrites under asteroid-like conditions to study the 3 μm total water band (Figure 4.3b). In their experiments they heat the sample to remove adsorbed H_2O and verify it has been removed by observations of the 6 μm band (Figure 4.3b). Their study illustrates the use of reflectance spectroscopy and the 6 μm band as a monitor to determine the presence or absence of water.

In remote sensing data, a 6 μm emission feature is observed on Mars [Bandfield et al., 2003; Ruff, 2004] and asteroids [Marchis et al., 2012]. Using the Thermal Emission Spectrometer (TES) instrument on the Mars Global Surveyor, a 6 μm emission feature was observed in dust-covered regions indicating the presence of bound or adsorbed water (Figure 4.3c) [Bandfield et al., 2003, Ruff ,2004]. On some asteroids, a 6 μm band is present in Spitzer Space Telescope Infrared Spectrograph data (Figure 4.3d) [Marchis et al., 2012]. The observations of a 6 μm band on Mars and asteroids demonstrates that if the lunar surface is host to H_2O, it should also exhibit a 6 μm feature in emission. While the 6 μm feature has been observed on planetary bodies, it has not previously been used to estimate the abundance of H_2O.

Currently, there are no operating or planned spacecraft capable of making 6 μm observations of the Moon. And, from groundbased telescopes, the 6 μm region is opaque to (Figure 4.4) making it impossible to obtain data of the lunar surface in this spectral region. Fortunately, there is one observatory capable of making these observations of the Moon; the airborne NASA/DLR Stratospheric Observatory For Infrared Astronomy (SOFIA). SOFIA operates at an altitude of 13.7 km, above a majority of the Earth's atmosphere. At this altitude, the 6 μm region

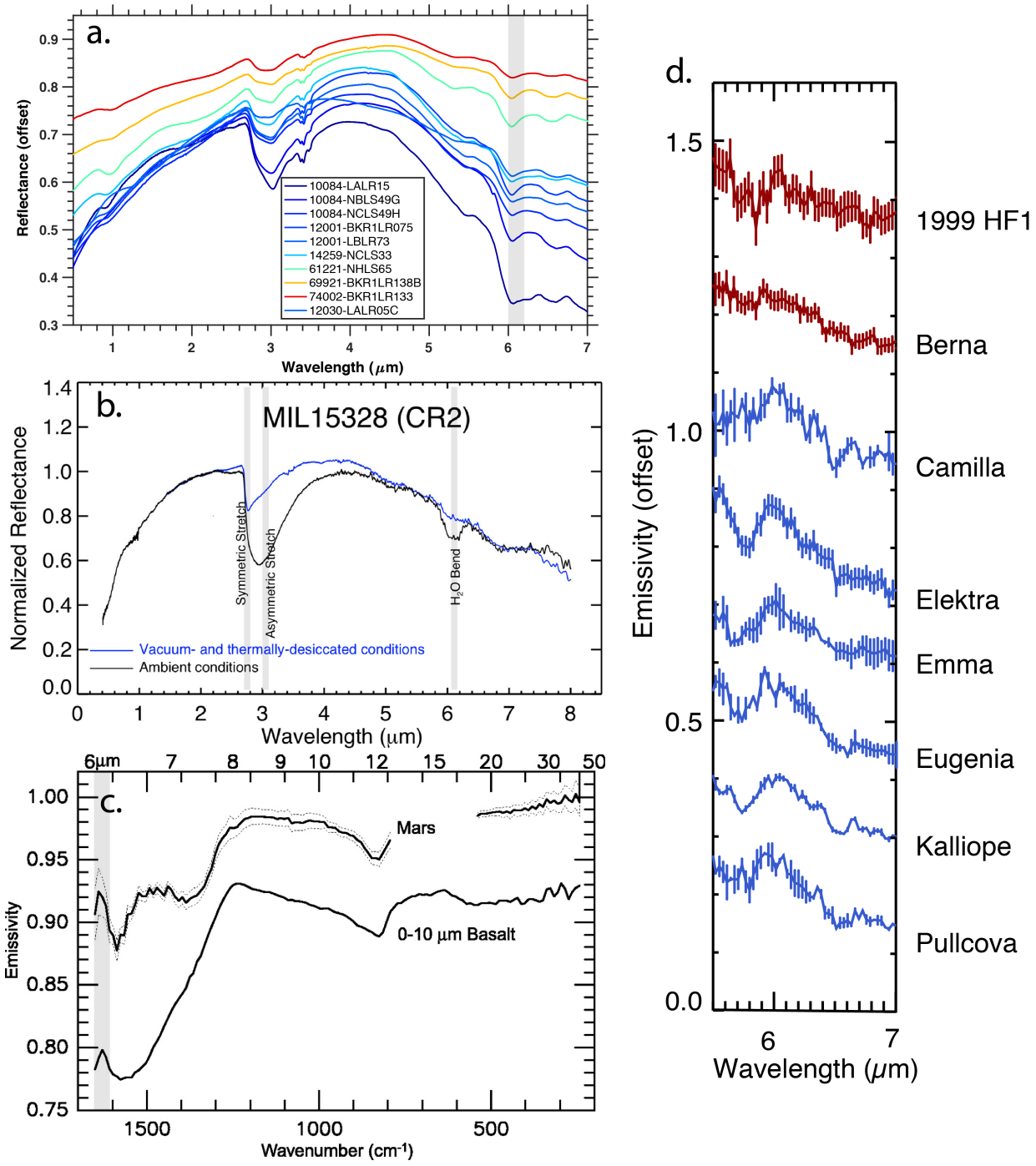

Figure 4.3: Reflectance spectra measured in the lab of (a) Apollo samples (b) meteorites [Takir et al., 2019] and emission spectra of (c) Mars [Bandfield et al., 2003] and (d) asteroids observed by SPITZER where red spectra show no 6 μm band and blue spectra show a 6 μm band [Marchis et al., 2012]. All plots exhibit a 6 μm absorption or emission band with varying shape and strength. The presence of the band indicates adsorbed or bound H_2O.

has high atmospheric transmission allowing for observations of a 6 µm feature on the lunar surface (Figure 4.4). The Faint Object infraRed CAmera for the SOFIA Telescope (FORCAST) instrument provides the required spectral range, spatial and spectral resolution, and sensitivity needed to observe the Moon at 6 µm. In the following sections, we report data from SOFIA FORCAST that show the presence of H_2O on the illuminated lunar surface.

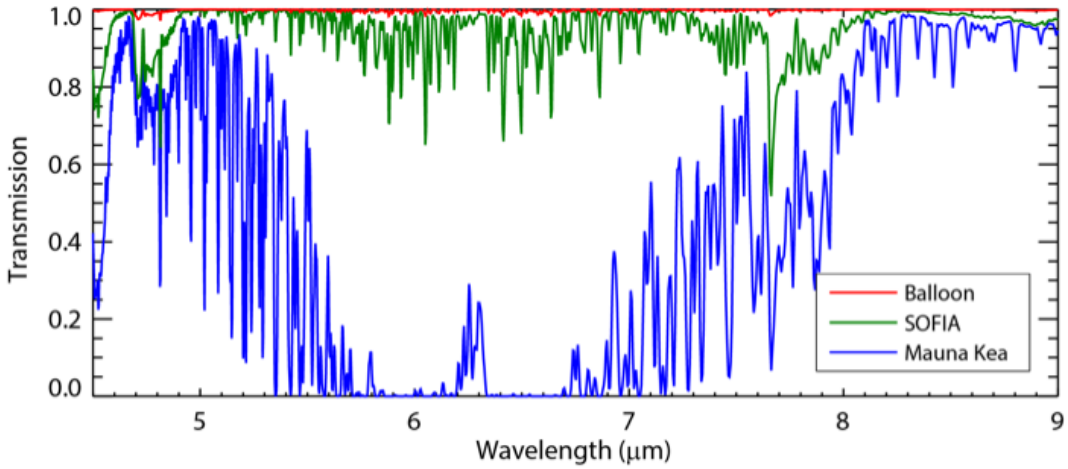

Figure 4.4: Atmospheric transmission at Maunakea observatory (blue), SOFIA (green), and from a stratospheric balloon (red).

4.4 Lunar Observations with SOFIA FORCAST

SOFIA is a 2.5 m telescope flown on a Boeing 747-SP aircraft and is used for infrared and submillimeter astronomy [Becklin and Moon, 2001]. The FORCAST detector combines a mid-infrared camera and spectrograph using 256 x 256 Si Blocked-Impurity-Band infrared focal plane arrays [Herter et al., 2018]. FORCAST is capable of both spectral imaging and slit spectroscopy. The instrument has multiple band filters and spectroscopic modes: long-slit low-resolution (R = 100 – 300) and short-slit, cross-dispersed high-resolution (R = 800 – 1200) mode [Herter et al., 2018]. For lunar observations, we used the G063 filter mode with the long-slit (2.4 x 191") low resolution mode to provide a spectral coverage of 4.9 to 8 µm. With a slit width of 2.4" and 0.768" pixel height, the spatial resolution on the center of disk of the Moon is 4.8 x 1.5 km.

Using FORCAST on SOFIA, we conducted the first observations of the lunar surface at 6 µm on August 30th, 2018 under a Director's Discretionary Time (DDT) proposal. During the DDT we were granted 30 minutes of observing time to demonstrate the feasibility of lunar observations using SOFIA as it had not been done since early operations. Our goal for this observing run was

to demonstrate lunar observations with SOFIA, but to also maximize the science return. During our run, the Moon was at a phase angle of 57.5°. To avoid saturating the detector, we chose locations near the dusk terminator that would be at temperatures ranging from 150 to 350 K with flux values between 0.49 to 4,559 Jy. We also chose two locations that would be most likely to have H_2O present and one location that was expected to have no H_2O as a control: Goldschmidt crater, Clavius crater, and Sulpicius Gallus pyroclastic deposit, respectively. Goldschmidt and Clavius were chosen because they are located at high northern and southern latitudes, respectively. At these latitudes we expect H_2O to be present and detectable owing too low surface temperatures. In contrast, we use Sulpicius Gallus to represent a location with little to no H_2O abundance because it is at low latitude (high surface temperature) and because basaltic glass is hydrophobic as observed from lab experiments [Hibbitts et al., 2011]. All three locations are also prominent on the lunar surface, which would aid in locating each feature in guider images used to support FORCAST target acquisition (Figure 4.5). During the observing run, each location was found with ease in the guider images using the Focal Plane Imager camera (Figure 4.5). Although the locations were found within guider images, we did not re-position the slit exactly on our targets to save time and maximize data collection.

The telescope on SOFIA is passively cooled by the surrounding air and operates at ~250 K causing the telescope itself to emit thermal radiation with a peak emission at 11 μm [Bufton and Yorke, 2016]. Therefore, our emission signals are from the telescope and our target of observation,

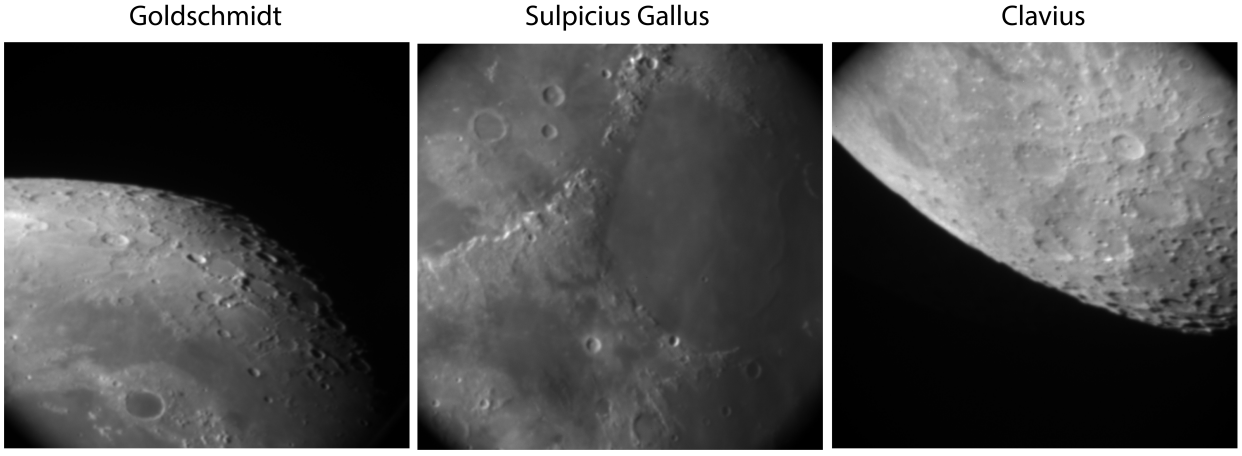

Figure 4.5: SOFIA FPI guider images showing accurate location pinpointing of the three targets. Prior to the observing run it was not clear if the guider cameras would be able to view the Moon. The FPI images demonstrate feasibility of locating geologic targets on the scale of a few km.

the lunar surface. To remove the sky background, a process termed "chopping" is used. Chopping uses a secondary mirror, which oscillates between on-target and off-target, where the off target is, ideally, clean sky without other potential emission sources [Bufton and Yorke, 2016].

The Moon is a highly extended object in the sky, and distances required to chop off the Moon to a clean sky is a maximum of 15 arcminutes, if the location of interest is near the center of disk. This distance is larger than SOFIA is capable of chopping, for this reason (and in addition to science reasons), we chose the three targets near the limb of the Moon and the dusk terminator to keep the chop distance ~ 200 arcseconds. Sulpicius Gallus was located next to the terminator, and therefore, we chopped onto the unilluminated side of the Moon which displayed a flux signal less than one mJ/arcsecond^2.

The first target we observed was Goldschmidt crater and, unfortunately, the chop direction was incorrect. Instead of chopping off the Moon to clean sky, the chop observations went farther onto the Moon, which caused a ghost image on the guider camera and the data could not be corrected for sky emissions. This issue was resolved for observations of Sulpicius Gallus and Clavius but the Goldschmidt observations are left out for the remainder of this study.

4.5 Data Processing

The processing steps are shown in Figure 4.6 which include cleaning of bad pixels, droop effect correction (the readout electronics exhibit a response offset causing a reduction in signal), nonlinearity correction (linearize the response of the detector), stacking (background subtraction of chop observations), and jailbar removal (removal of residual signal). Because the Moon

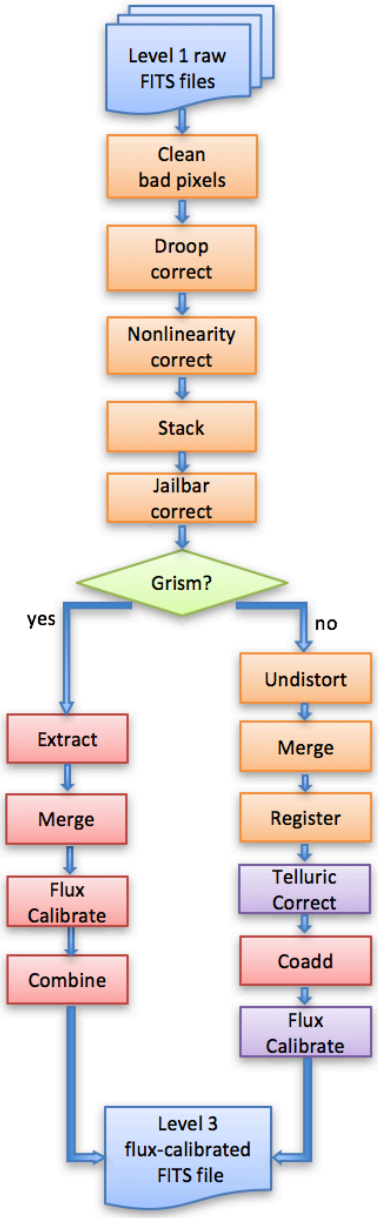

Figure 4.6: SOFIA processing pipeline. [SOFIA Guest Observer Handbook for FORCAST Data Products]

fills the entire FORCAST slit, we requested to have the full spectral image without spectral extraction. The processing, therefore, skips the extract and merge steps and continues with the flux calibration (Figure 4.6).

During flux calibrations, each spectrum is corrected for instrumental response and atmospheric transmission. At its operational altitude near 14 km, spectra collected by SOFIA are not free from telluric water vapor absorption lines (Figure 4.4), and water is typically present at abundances of ~2 to 10 ppm [Bufton and Yorke, 2018]. Correction of water vapor and other atmospheric lines is performed by modeling and removing the atmospheric transmission during the observations at the altitude SOFIA was flying using the Atmospheric TRANsmission (ATRAN) model [Lord, 1992]. At the end of processing, the data consist of flux-calibrated spectral images in units of Jy. The data reduction and calibration processes is described in detail in the Herter et al., 2013.

4.6 Methods

We receive fully calibrated flux data from SOFIA. The data are spectral images that are 248 x 248 pixels, where the x axis is wavelengths covering 5 to 8 μm and the y axis is spatial position on the Moon along the spectrograph slit (Figure 4.7a). Figure 4.7b shows where the slit position on the guider image and data was collected. Further processing of the data is done via custom IDL routines and includes removal of additional instrumental artifacts and estimating water abundances from the spectra.

4.6.1 Removal of Instrument Artifact

Spectra received from FORCAST show a low frequency spectral oscillation (Figure 4.7a) that has been observed in previous FORCAST data. This oscillation is not due to lunar surface spectral variation. Typically, SOFIA observers ignore the oscillation because their spectral lines are sharp and strong and can be seen through it. However, the 6 μm emission, that we show in the next section, is relatively weak, on the same order of intensity as the spectral oscillation artifact. Therefore, the oscillation must be removed to properly analyze the data. To remove the oscillation, we use the six Sulpicius Gallus spectral images at low latitude (i.e., low total water) to isolate the oscillation. We use Sulpicius Gallus pyroclastic deposit as a reference because we expect it to

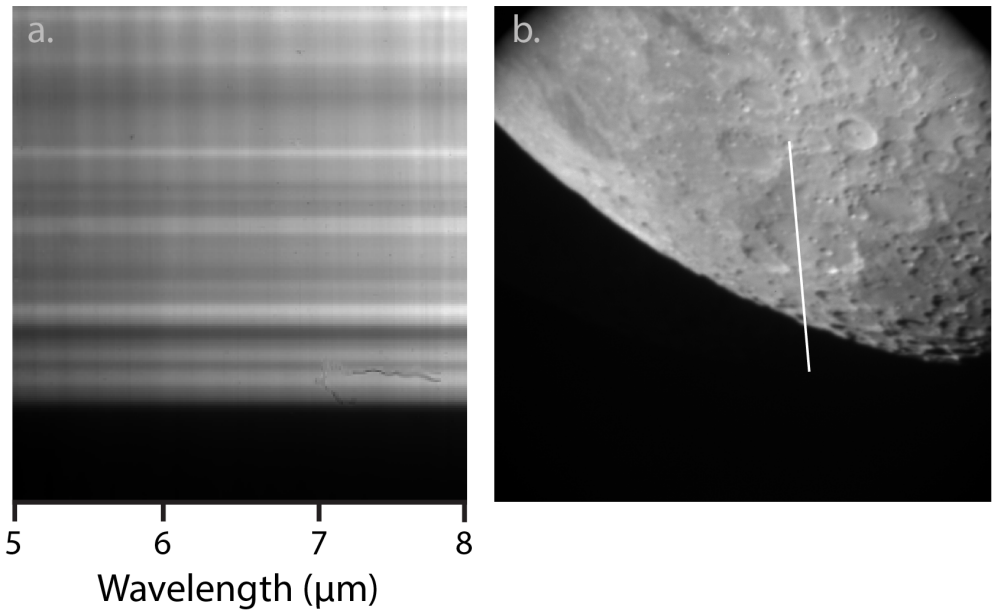

Figure 4.7: a.) Spectral images from SOFIA of the Clavius region and surrounding area. Oscillation superimposed on this image is not a lunar feature. The artifact on the top right is due to some contamination on the window of FORCAST. b.) Guider image of the Clavius region and the location of the slit.

contain low abundance of H_2O in contrast to the Clavius region. We reasoned this based on lab analysis that basaltic composition glass, analogous to pyroclastic deposit material, is hydrophobic [Hibbitts et al., 2011] but also due to its spectral shape at 3 μm using data acquired with the groundbased IRTF SpEX instrument from Chapter 3 with no indications of molecular water.

Although the 3 μm total water band cannot be used to distinguish between OH versus H_2O (described in Section 4.2), the spectral shapes of the 3 μm band [Takir and Emery, 2012], as observed in the SpEX data, do show differences due to either the species present or the composition of the material. If we assume the varying spectral shape indicates the presences of OH (sharp Figure 4.8 top) or H_2O (round Figure 4.8 bottom), then we can use the SpEX data to indicate locations that may have water (indicated by a round spectral shape) and those that may only have OH (indicated by a sharp spectral shape). We compared the SpEX spectrum at Sulpicius Gallus and Goldschmidt crater to water-bearing glasses (Mid-Ocean Ridge Basalt; MORB) measured in the lab that have known abundances of H_2O (Figure 4.8). We find that when no H_2O is present in the MORB glass, the spectral shape is sharp and fits the Sulpicius Gallus spectrum (Figure 4.8 top). When we examine Goldschmidt, we find that its round spectral shape matches a MORB

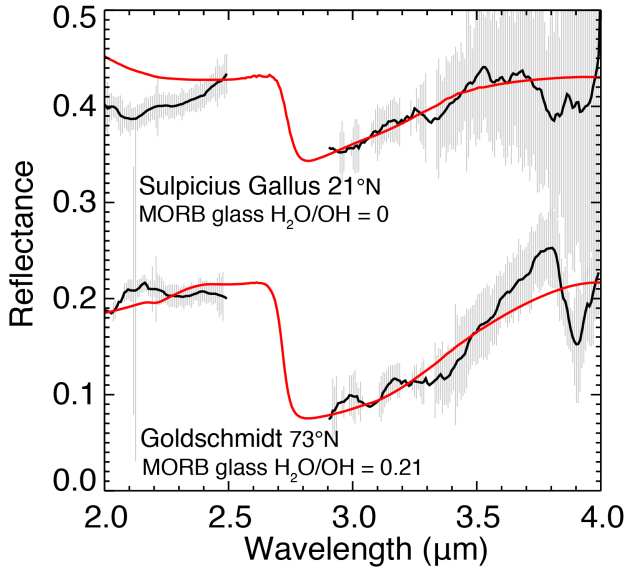

Figure 4.8: Spectra of Sulpicus Gallus (top) and Goldschmidt (bottom) showing the sharp and round spectral shapes, respectively. Assuming the spectral shape indicates the presence of water or lack of, Sulpicius Gallus shows no H_2O while Goldschmidt shows theres water present. Water bearing glasses (red) with known abundance of H_2O agree with Sulpicius Gallus not containing H_2O.

containing water (Figure 4.8 bottom). For this reason, we chose to observe Sulpicius Gallus as a dry reference.

However, as discussed in section 4.2, at 3 μm, OH attached to metal cations can broaden the 3 μm band, and this is therefore not a definitive detection of H_2O. We use Sulpicius Gallus to extract the oscillation and remove it from the Clavius data. To remove the oscillation observed in the spectral images, we first remove a continuum from each spectrum in all six of the acquired

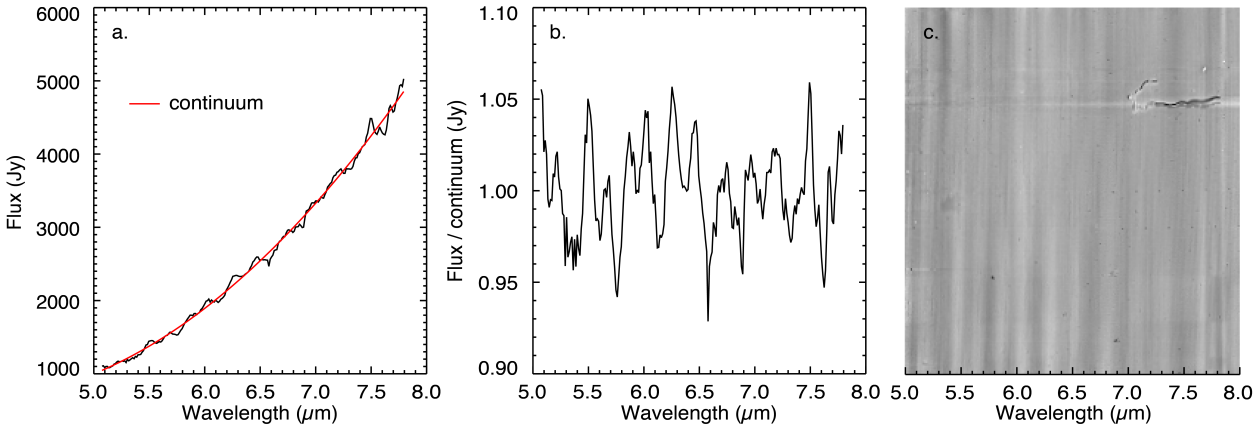

Figure 4.9: a.) Flux spectrum of Sulpicius Gallus showing the oscillation and continuum to be removed in red. b.) continuum removed spectrum. c.) Sulpicius Gallus oscillation image.

Sulpicius Gallus spectral images (Figure 4.9a and b). Then we take the mean of the continuum-removed images to create an image of the oscillation (Figure 4.9c). The oscillation image is then divided out of the Clavius spectral images to provide clean spectral images (Figure 4.10a). The removal of the continuum sets the oscillation image to have a mean about 1 so that when the oscillation image is divided out of the Clavius spectral images, the flux values are preserved. It is unknown if there is H_2O present at Sulpicius Gallus, therefore, if there is H_2O present, the oscillation image will cancel out that amount in the Clavius data. For this reason we report lower limit abundances of H_2O.

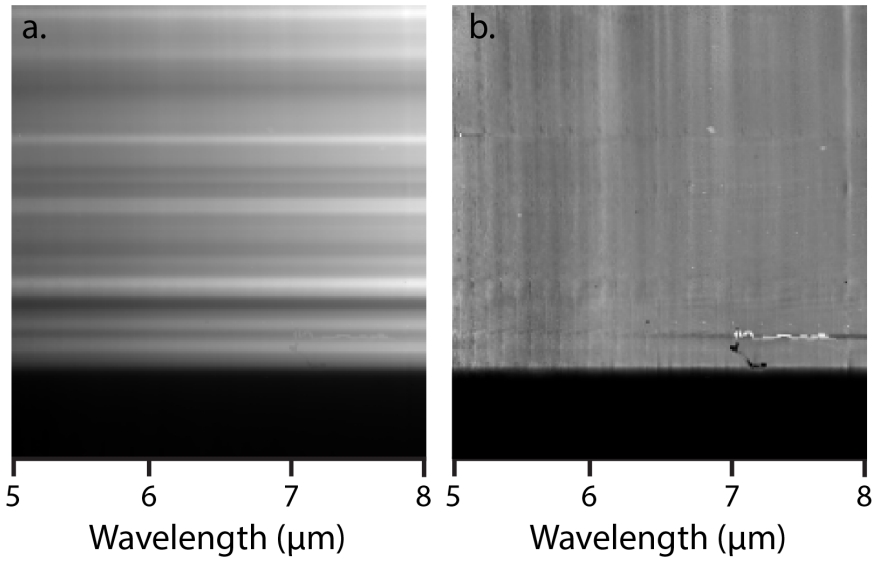

Figure 4.10: a.) Oscillation-removed flux special image of Clavius region. b.) Clavius region with continuum removed. A bright band is seen around 6 μm in the continuum-removed spectral image of Clavius indicating the presence of H_2O.

4.7 Detection of a 6 μm Emission Band

Using the SOFIA observations of the Clavius region, we have made the first direct detection of H_2O on the illuminated lunar surface. At Clavius crater and the surrounding terrain, we observed a broad 6 μm emission band (Figure 4.11). The band shown in Figure 4.11 is centered at 6.06 μm with a band width of 0.01 μm and an intensity of 0.028. The error is derived from the square root of the variance reported by SOFIA propagated through the data processing. In Figure 4.9b the band can be seen along the entire slit and is not present at just a single location but instead

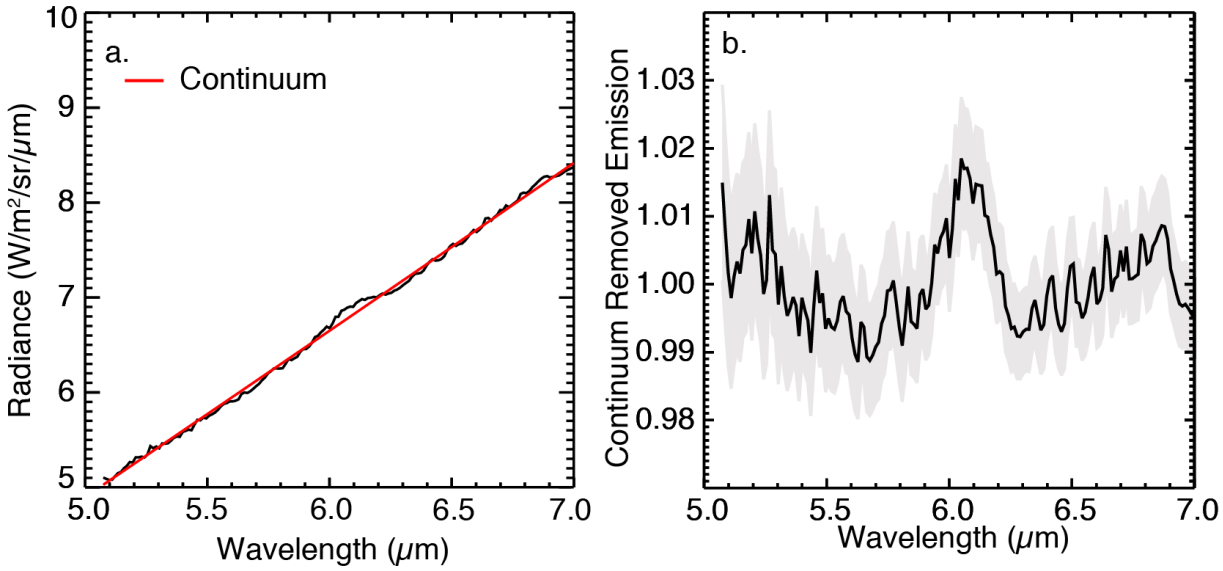

Figure 4.11: a.) Oscillation removed radiance spectrum of Clavius region. b.) Continuum removed radiance showing a strong 6 μm emission band indicating the presence of H_2O.

covers a larger spatial area. Even before the continuum is removed (Figure 4.11a) the 6 μm band can be seen.

4.7.1 Assigning 6 μm Emission to H_2O

After first inspection, the data show a clear 6 μm emission feature that is possibly due to H_2O. However, because of the limited work in observing the 6 μm H_2O feature, remotely we examined the spectral band qualitatively and quantitatively to determine if its properties are consistent with particulate water-bearing materials. To do this, we looked at the properties of water-bearing MORB glass samples [Li, 2017], meteorites with water from exposure to the terrestrial environment [Takir et al., 2019], asteroid Electra [Marchis et al., 2012], and literature values of the fundamental H-O-H bend [Falk, 1984].

On visual inspection, the lunar 6 μm band is broader than the 6 μm band of the MORB glasses and the band center is shifted to slightly lower wavelengths (Figure 4.12). The differing 6 μm bands are to be expected given the differing composition of material and phases. However, comparison of the lunar 6 μm band to the meteorites 6 μm band, they have almost identical band shape, center, and width. The asteroid band is slightly broader than the lunar and meteorite 6 μm bands and its band center is shifted slightly to lower wavelengths. Each of these spectra exhibit only one single feature and the similar 6 μm band properties indicate that the same species is being

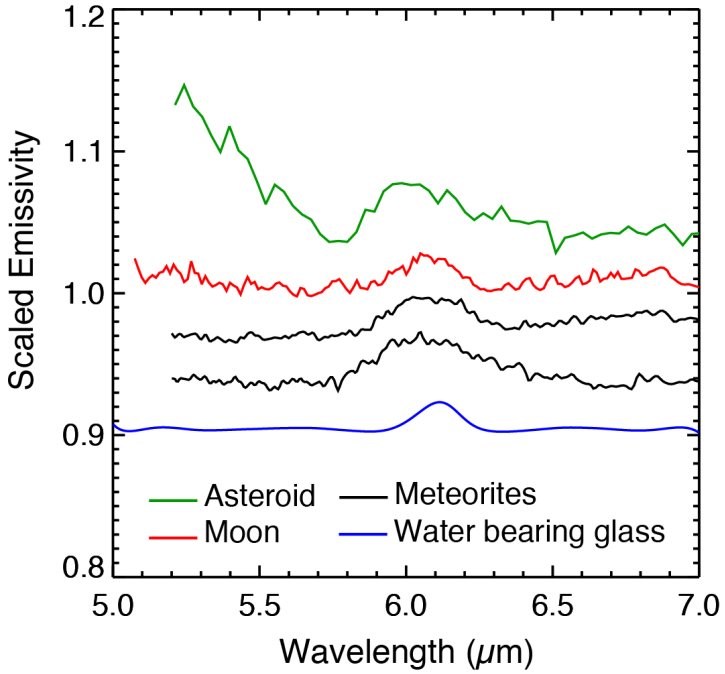

Figure 4.12: Lunar 6 µm emission band observed by SOFIA (red) compared to other 6 µm bands seen on asteroid Elektra (green), meteorites Mil15328 and Murchison (black) [Takir et al., 2019], and in water bearing glass beads (blue).

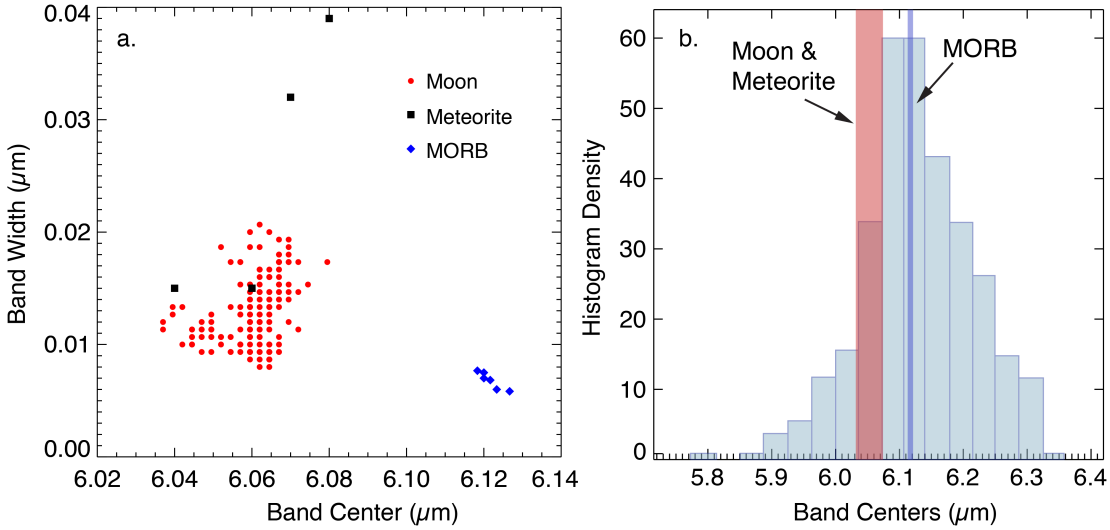

Figure 4.13: a) Band centers of the lunar 6 µm (red), meteorite (black), and MORB (blue) bands. b) Distribution of H_2O band centers for crystalline hydrates from Falk 1984.

observed. The difference in band center and widths can be effects of differing composition of the host material and chemical phase of the water.

To quantitatively determine the band center, width, and peak height of our lunar data, meteorites, and the MORB glasses, we fit a library of Gaussian functions to each spectrum and

Table 4.1: 6 μm band properties for the Moon, meteorites, MORB and literature values. See Appendix for full data.

Material	Band Center		Band Width		Peak Height	
	Range	Mean	Range	Mean	Range	Mean
Moon	6.032 – 6.122	6.080	0.054 – 0.270	0.125	0.012 – 0.035	0.022
Meteorite	6.052 – 6.088	6.073	0.118 – 0.204	0.166	0.070 – 0.199	0.142
MORB	6.118 – 6.124	6.121	0.086 – 0.089	0.087	0.008 – 0.015	0.011
Falk, 1984	5.811 – 6.321	6.112	–	–	–	–

find the best fit. The range and widths of the band centers and widths are shown in Fig 4.13a and given in Table 4.1. The observed values for the Moon, meteorites, and MORB glasses all fall within the reported band center range of the H-O-H bend in crystalline hydrates [Falk ,1984] (Figure 4.13b). We find that the lunar band centers are consistent with Falk (1984) and with water bearing meteorites. The Moon and meteorites band centers are offset from the MORB glasses, this is to be expected as the MORB glasses are synthetic and pristine samples that lack the complexity of planetary material. The complexity of planetary material may affect the position and shape of the 6 μm band.

Based on these comparisons, we attribute the observed 6 μm feature on the Moon to molecular water. We are unaware of any other material reasonable for the Moon that exhibits a single spectral feature at 6 μm other than H_2O.

4.8 Deriving Abundances

In laboratory analysis of geologic thin sections, the abundance of H_2O is quantified by measuring the thickness of the sample, its absorbance peak and baseline, and converting these to concentrations using the Beer-Lambert law [McIntosh et al., 2017]. In remote sensing of planetary regolith's, samples are in particulate form and no work has been done on deriving the absolute abundance of H_2O from reflectance spectra near 6 μm. In previous work, Li et al., (2017) measured the reflectance spectra from 1 to 25 μm of MORB glasses with known absolute water content [Shimizu et al., 2015]. Each sample was heated to 600°C in 50°C increments and measured by FTIR spectroscopy at every step to determine how the 3 μm band varies with total water (Figure 4.14a & b). The data in Figure 4.14a and b show how the 6 μm band strength varies with varying

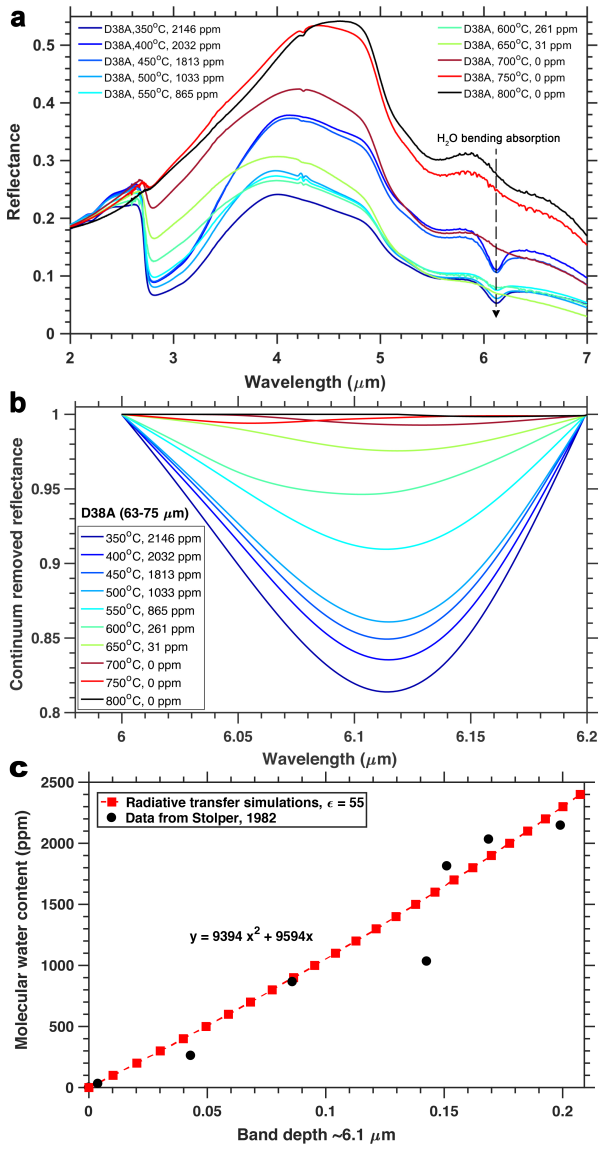

Figure 4.14: Water bearing glass beads showing a 3 and 6 μm absorption (a) used to derive a relationship between band depth (b) and H_2O content (c).

abundance in H_2O. Using this same data set, we used the 6 μm band to derive an empirical relationship between band depth in reflectance and absolute abundance of H_2O:

$$y = 9394 \cdot b^2 + 9594 \cdot b, \tag{4.1}$$

where y is the abundance of H_2O in ppm and b is the 6 μm band depth in reflectance (Figure 4.14c). The particle size of this group of samples is 63 to 75 μm which is within the mean particle size range of 60 to 80 μm measured by Mitchell et al., (1972).

Our data, however, are in emission, and we therefore need to convert to reflectance to measure the band depth and estimate the abundance. First we assign an emissivity (e) to our data using:

$$e = 1 - R_{ref} \tag{4.2}$$

where R_{ref} is the reference continuum at 6 μm from Apollo samples taken to be 0.3 providing an emissivity of 0.7. We apply this to our emission spectra (E):

$$E = F * e \tag{4.3}$$

where F is the flux. We then use Kirchoff's law to convert emission to reflectance (R):

$$R = 1 - E \tag{4.4}$$

Lastly we calculate the band depth of the 6 μm band in reflectance using:

$$b = 1 - \frac{R_{band}}{R_{cont}} \tag{4.5}$$

where R_{band} and R_{cont} are the mean absorption peak from 6.0 to 6.1 μm and the mean continuum from 5.2 to 5.3 μm, respectively. Now, we can use the empirical relationship in Eq. 4.1 to estimate the abundance of H_2O. Over the entire data set for the Clavius region, we calculate abundances between 243 and 725 ppm H_2O with average abundances of 494 ± 14 ppm H_2O (Figure 4.15).

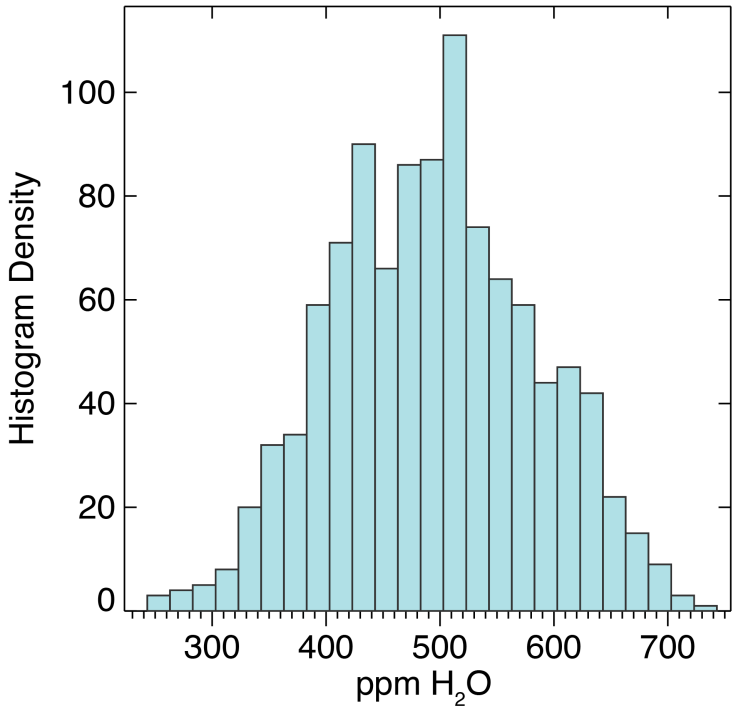

Figure 4.15: Distribution of H_2O abundance for all six Clavius spectral images with a mean of 494 ± 14 ppm H_2O.

These estimates are lower limits because Sulpicius Gallus was used as reference and any water present would have been removed from the Clavius data. The error in abundance is found by adding plus and minus one sigma to the spectra and converting the spectra to abundance and finding the difference in abundance between the original spectra and the error included spectra.

4.8.1 H_2O Abundance with Latitude

SOFIA FORCAST data are spectral image cubes with 248 spectra along the slit. This provides spatial information regarding the strength of the 6 μm band as the slit transected high southern latitudes out to the sky as seen in Figure 4.7. Because of this, we can examine how the strength of the band varies with latitude. Figure 4.16 shows the band depth and lower limit abundance in ppm H_2O versus latitude. From the observed band depth, there is no clear trend of increasing or decreasing band strength, and therefore abundance of H_2O, with latitude. However, only a limited area was observed and therefore we cannot comment on global variations with latitude.

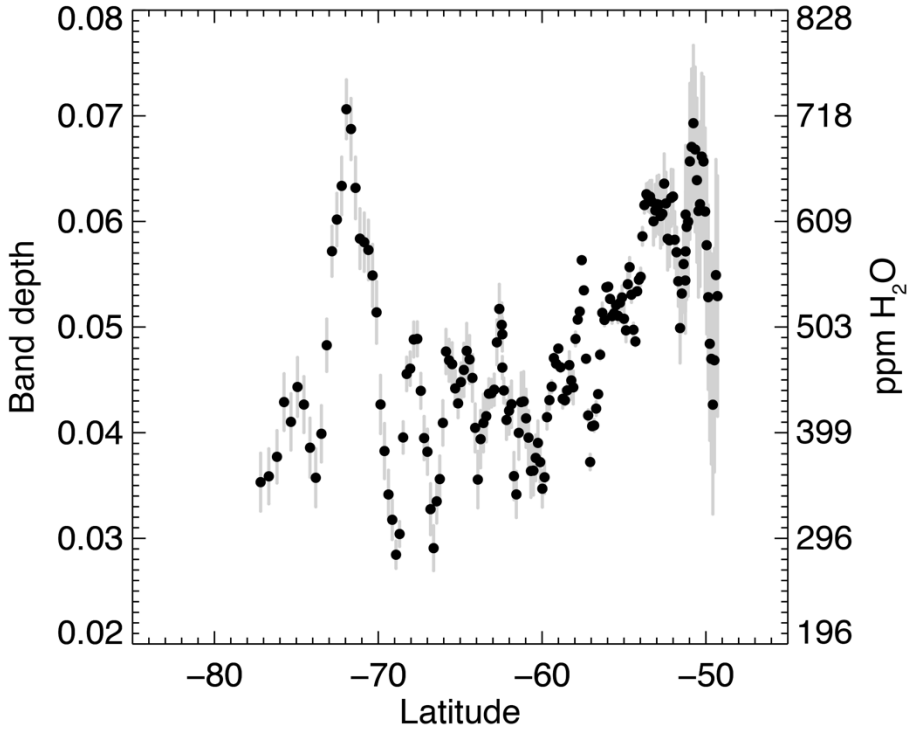

Figure 4.16: One of the six frames of Clavius showing the lunar 6 μm band depth and abundance versus latitude. No clear trend with latitude is observed.

4.9 Discussion

The detection of the 6 μm band supports the hypothesis that the lunar surface can retain migrating water (as described in Chapter 3) [Watson et al., 1961; Sunshine et al., 2009] or sequester metastable water in impact glass [Liu et al., 2012; Daly and Schultz, 2018]. How much of the water is stored within the grains and how much is on the grain surface is important for understanding the migration of water and its ability to supply the poles and the atmosphere. The abundance of water that can survive on grain surfaces is highly dependent on surface temperature. To estimate the abundance of water in grains or on the surface of grains, we first estimate the temperature of the lunar surface and how much the surface of grains can hold at the observed temperature.

4.9.1 Estimating Surface Temperature

There are two types of temperatures: kinetic and brightness temperature. Kinetic temperature is the physical temperature that governs the surface chemistry. Brightness temperatures is what we measure with remote sensing and is a measurement of energy emitted by an object and the temperature of a blackbody that would result in the measured energy. Measurements of brightness temperature commonly includes of both illuminated and shadowed surfaces due to the lunar surface being rough at small scales. At high latitudes, we observe the surface at high inclination illumination angles, which exacerbates the surface roughness problem. These surfaces will either be shadowed with low temperatures or inclined towards the sun with high temperatures, which will dominate the spectrum. Consequently the brightness temperature should be lower than the kinetic temperature. The kinetic temperature of the illuminated hot surface can be calculated using:

$$T = T_{ss} * cos(i)^{1/6} \tag{4.8}$$

where i is the incidence angle and T_{ss} is the temperature of the sub-solar point [Pettit and Nicholson, 1930; Lawson and Jakosky, 1999]. Using 380 K for the sub-solar point and the incidence angle of 74.92˚ for our observations of Clavius region calculated from JPL Horizons ephemeris, we calculate the kinetic temperature to be 304 K.

To find the brightness temperature, we use Planck's law by first converting our data to radiance in W/m^2/sr/μm and using the FORCAST slit width (2.4") and pixel height (0.768") to determine the relevant solid angle. We calculate a mean brightness temperature of 310 ± 12.5 K

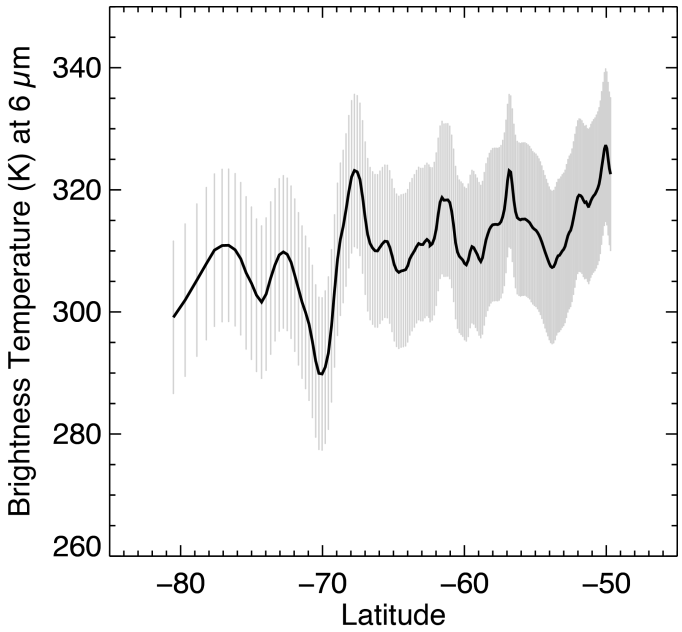

Figure 4.18: Brightness temperature from one observation of the Clavius region. The variation in brightness temperature corresponds to locations of more or less illumination. The error is found by converting the variance reported by the FORCAST processing, converting it to radiance and brightness temperature and taking the square root.

in the Clavius region at 6 μm at a lunar local time of ~14:30. Figure 4.18 shows the brightness temperature at 6 μm along the slit, as a function of latitude. The variation in temperature corresponds to variation in illumination of the surface. The error in brightness temperature is derived from the square root of the variance, provided by SOFIA, converted to brightness temperature. The brightness temperature that we calculate is higher than the estimated kinetic temperature, there are two possible explanation for this. First, while observing the Moon, we could not perform nodding of the telescope (repositioning of the instrument slit to a slightly different location to remove residual telescope emission) due to the spatial extent of the Moon. This may have resulted in some residual telescope emission which was not fully removed in the chopping technique. To understand if there was residual telescope emission we inspected portions of the slit that fell on the sky, these did not contain enough residual brightness. Therefore, the amount of residual thermal emission from the telescope should be small and within our error. The second cause is window degradation of SOFIA during our observations. The window had artifacts that could have affected the flux calibration causing higher flux values, and, therefore, temperature. Data obtained in imaging mode was greatly affected by the window, however, we collected data in grism mode that only occupied a small portion of the detector array. The adverse effects of this

is unknown. For the purpose of further discussion, we will use the brightness temperature of 310 K to determine how much H_2O is on the surface and free to migrate.

4.9.2 Estimating the Abundance of H_2O Available to Migrate

At temperatures derived from SOFIA spectra, ~310 K, only ~10% of a monolayer (a layer one molecule thick) is permitted on the surface of silicate grains (Figure 4.19) (methods of Jones et al., 2019). To estimated how much of the water can be due to migratory H_2O with a 10% monolayer we first find the amount of H_2O the surface of an average lunar grain can contain. We calculate the mass per unit area of a monolayer of water (M_{mono}), for that we need the molar mass of water (M_{H_2O}, 18 g/mol) and the area of a water molecule (A_{mono}). This gives:

$$M_{mono} = \frac{M_{H_2O}}{A_{mono}} = \frac{M_{H_2O}}{d_{H_2O}^2 * N_0} = 3.95x10^{-4}\ g/m^2/mol, \quad (5.4)$$

where d_{H_2O} is the diameter of a water molecule (0.275 nm), and N_0 is Avogadro's number. We then find the mass of a 10% monolayer, which is $3.95x10^{-5}\ g/m^2/mol$. To get the abundance of H_2O this 10% monolayer can hold, we multiply M_{mono} by the surface area of lunar soils which we take to be on average $0.5\ m^2/g$ [Cadenhead et al., 1977; Robens et al., 2007]. From this, we find that the lunar surface can only hold ~20 ± 4 ppm H_2O in the form of water trapped on the surface of a grain in a 10% monolayer. This abundance is, on average, about 20 times less than the total abundance of water that we measured with SOFIA.

This result has implications for the storage and migration of H_2O. First, if the temperatures are low enough to support a 100% monolayer, the surface of grains can hold ~198 ppm H_2O. At low enough temperatures, the surface could hold most of the water observed by SOFIA. However, most of the water we observed is likely trapped within the grains, allowing only a small amount of H_2O available to migrate at high latitudes, even given the uncertainties in temperature estimates. By implication, most of the water observed must be contained within the lunar grains. If we further assume that the molecular water is confined to agglutinate glass, then the abundance of water in the glasses ranges from 810 to 2,416 ppm H_2O with an average of 1,647 ppm H_2O (0.3 wt. %) as typical lunar soils contain about 30% glass by weight originating from micrometeorite impact [McKay et al., 1991]. Stolper (1982) found that at low abundances of hydration in glass, H was speciated as OH rather than H_2O. He found that at abundances less than 2,000 ppm H_2O equivalent,

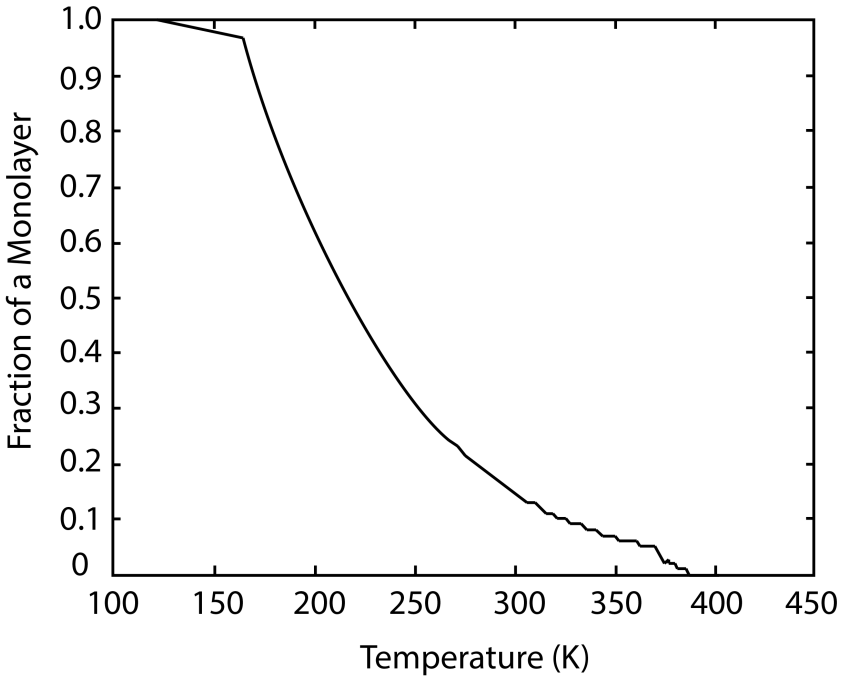

Figure 4.19: Fraction of a monolayer available to cover the lunar surface at specific temperatures for southern latitudes. Temperature was calculated based on Hurley et al., 2015. (Personal communication, Thomas Orlando and Brant Jones]

molecular water was not present. Our abundances of molecular water, however, are lower than Stolper (1982) claimed are stable. We point out that Daly and Schulz (2018) found molecular water in their samples, produced in impact experiments, at far lower abundances than Stolper (1982). The lower limit defined by Stolper (1982) may, therefore, not apply in all cases, and our observations and abundances are in agreement with Daly and Schultz (2018).

Our mean abundance of water is twenty times higher than Liu et al. (2012), who measured 70 ppm H_2O equivalent, or total water, in agglutinate glasses originating from Apollo lunar soil samples taken near the equator. This is consistent with more total water at high latitudes relative to the equator, as shown in M^3 and IRTF data. Li and Milliken 2017 measured ~500 ppm H_2O in M^3 data at high southern latitudes while at the equator they measured less than 100 ppm H_2O. Our abundances from SOFIA are in agreement with total water abundances measured in Chapter 3. Lastly, the low abundance of water that the surface of grains can hold means there is little available to migrate, therefore, we expect that there is little variation in the 6 μm band occurring at high latitudes. This would be consistent with Li and Milliken (2017) and our observations in the previous chapter where little variation of the 3 μm band is observed above 60° latitude in M^3, IRTF, and FUV LAMP data. Finally, the water contained in the agglutinate impact glass can be

remobilized by micrometeoroid impact as Farrell et al., 2019 pointed out regarding impacts into permanent shadow. Therefore, water stored in agglutinates is not a permanent sink isolated from the lunar atmosphere and poles.

4.10 Conclusions

We have successfully detected H_2O on the illuminated lunar surface using the SOFIA FORCAST instrument. This is the first direct, unambiguous detection of molecular water. We measured lower limit abundances ranging from 243 to 725 ppm H_2O in the Clavius region located at high southern latitudes. Of this estimated H_2O abundance, we calculate that ~96% of the observed water is stored within the lunar grains based on temperature and surface area estimates. These estimates only allow a small amount of H_2O to be available to migrate at high southern latitudes. Any variation due to migration with diurnal cycles is expected to be small and possibly undetectable.

CHAPTER 5: CONCLUSIONS AND FUTURE WORK

5.1 Summary

In this dissertation, we explored the remote measurements of volatiles components on the Earth and Moon using infrared wavelengths. In Chapter 2, we built, tested, and deployed a light weight instrument (MIDAS) operating in the MWIR that is attractive for small satellite platforms to monitor and study high temperature phenomena on the Earth. MIDAS employs a Sagnac interferometer married to an uncooled microbolometer to keep the weight, volume, and power consumption low. MIDAS is capable of providing measurements of high temperature targets with signal-to-noise ratios in the hundreds. At the former Kīlauea lava lake, we demonstrated the MIDAS instrument's ability to conduct field observations of the volcanic gas plume using the lava lake as the hot source of radiance. MIDAS was able to produce spectral radiance and brightness temperature maps. Using line-by-line radiative transfer modeling, we modeled the spectra and map the abundances of volcanic CO_2 within the plume. From this work, we conclude that MWIR measurements with a light-weight instrument are possible for high temperature phenomena. While we only looked at CO_2, MIDAS is capable of measuring H_2O, CH_4, and, if extended to longer wavelengths, SO_2 and the chemical composition of solid targets.

In Chapters 3 and 4, we investigated the hydration of the Moon using two new observatories and new wavelength ranges for the Moon. We investigated the variability of the 3 μm band using the groundbased IRTF, which provides wavelengths beyond 3 μm. Using these longer wavelengths, we are able to strongly constrain thermal models out to 4 μm. This work demonstrates the utility of the longer wavelengths to accurately remove the lunar thermal component from 3 μm data. Thermally corrected data provided a view of the variability of the 3 μm band, attributed to OH + H_2O, using observations of the same location at different lunar times of day. We found that the band variation is due to changes in abundance of total water and that it varies with lunar time of day, latitude, and composition. This confirms that the variation is due to either migrating H_2O or to the diffusion of H through lunar grains forming transient OH.

Using new remote sensing techniques and a new data set from SOFIA, we reported the first direct unambiguous detection of molecular water on the illuminated lunar surface in Chapter 4. Use of 6 μm spectroscopy of the lunar surface has revealed the presence of H_2O at high southern

latitudes. Prior to this detection, it had been theorized that H_2O could form on the Moon, but all detections were indirect or ambiguous. Using 6 μm emission bands to detect H_2O is new to remote sensing, and provides a definitive detection. With a single observing run on SOFIA, we collected data at high southern latitudes and observed the 6 μm band attributed to H_2O. Using water bearing glasses with known abundances of H_2O, we derived an empirical relationship to estimate a lower limit abundance of H_2O present. We estimate approximately 28 to 368 ppm H_2O is present in the high southern region of Clavius. Based on the calculated brightness temperature and the abundance measured, we estimate that, on average, 85.2% of the water observed resides in the lunar agglutinate grains formed from micrometeoroid impacts. From our observations, this gives a lower limit abundances of 3 to 1137 ± 267 ppm H_2O within the agglutinate glasses.

5.2 Future work

5.2.1 Determining the use of MIDAS for Lunar Field Work

Instruments like MIDAS are attractive for use in the field, like at the Kīlauea lava lake, but also for lunar exploration. With the Remote In Situ and Synchrotron Studies for Science and Exploration 2 (RISE2) team, an instrument similar to, if not MIDAS, will be used to simulate astronauts working on the lunar surface during an Extra Vehicular Activity (EVA). MIDAS will be set up in the field as if it was mounted onto a lunar rover. Once at a new location, MIDAS will scan the location collecting data to be processed in real time and creating spectral maps of the scene looking for spectral anomalies. Scientists and astronauts can then examine the spectral maps and plan the upcoming EVA to sample specific locations that show interesting composition in the spectral maps. This work has already been started using a LWIR instrument, but we hope to extend to the MWIR so that hydration features such as the 3 and 6 μm bands can be observed as well.

5.2.2 Connecting IRTF and SOFIA Observations

We will continue to observe the lunar surface with both the IRTF and SOFIA. Observations with the IRTF have been conducted for two years. Our complete data set has not been fully processed and examined due to the vast amount of data collected. One project is to process the maps of pyroclastic deposits. Using our long wavelengths, we can constrain the thermal models and provide better estimate of total water abundance at pyroclastic deposits. These estimates are

important because hydration observed at these geologically interesting locations provides information about the hydration of the lunar interior and its formation history.

Now that the presence of H_2O on the Moon is confirmed, we will continue to make observations with SOFIA looking at how water behaves on a global scale. We will look at the 6 μm feature in the same way we have the 3 μm band with the IRTF by observing the same location at multiple lunar times of day to look at the diurnal variability of water or to constrain the water to the interior of grains. We will also map the same pyroclastic deposits as we did with the IRTF to see if H_2O is present in the glass beads of the deposits. Currently, we have additional observing time on SOFIA on October 14th, 2019. We are also working on proposals for a 6 μm instrument to orbit the Moon either as a CubeSat or on a larger platform.

Our observations of the lunar surface at both 3 and 6 μm greatly improves our knowledge of the surface and internal processes that have occurred, and are occurring, on the Moon. The maps we produce from both the IRTF and SOFIA can be used for future exploration of the Moon. They can be used to locate large reservoirs of water on the Moon for *in-situ* resource utilization and for sustaining life on the surface long term.

APPENDIX

Moon				Meteorite			
Centers	**Widths**	**Depths**	**ppm H_2O**	**Centers**	**Widths**	**Depths**	**ppm H_2O**
6.072	0.062	0.030	299.662	6.088	0.204	0.199	2281.853
6.082	0.058	0.030	299.662	6.052	0.138	0.070	722.808
6.074	0.070	0.032	313.230	6.072	0.118	0.099	1042.422
6.078	0.066	0.032	320.027	6.080	0.202	0.199	2281.853
6.080	0.066	0.032	320.027	**MORB**			
6.076	0.070	0.030	292.890	**Centers**	**Widths**	**Depths**	**ppm H_2O**
6.078	0.066	0.031	306.442	6.119	0.088	0.015	2146.000
6.080	0.074	0.028	279.371	6.119	0.087	0.012	2032.000
6.078	0.074	0.028	279.371	6.121	0.086	0.011	1813.000
6.078	0.066	0.031	306.442	6.120	0.086	0.009	1033.000
6.074	0.078	0.030	292.890	6.124	0.086	0.008	865.000
6.068	0.082	0.028	279.371	**Moon**			
6.072	0.078	0.028	279.371	**Centers**	**Widths**	**Depths**	**ppm H_2O**
6.066	0.078	0.028	272.625	6.092	0.194	0.016	159.208
6.064	0.078	0.029	286.126	6.092	0.186	0.016	152.612
6.074	0.070	0.030	292.890	6.114	0.186	0.014	132.873
6.078	0.070	0.030	292.890	6.104	0.182	0.015	146.024
6.080	0.066	0.029	286.126	6.100	0.194	0.018	172.426
6.084	0.066	0.028	272.625	6.086	0.182	0.018	179.047
6.084	0.066	0.029	286.126	6.090	0.162	0.020	198.962
6.076	0.074	0.027	265.886	6.094	0.166	0.020	198.962
6.058	0.086	0.026	259.156	6.088	0.150	0.024	239.016
6.064	0.086	0.026	252.435	6.086	0.154	0.023	225.631
6.062	0.090	0.026	252.435	6.122	0.226	0.019	185.677
6.064	0.082	0.026	259.156	6.122	0.210	0.020	198.962
6.058	0.094	0.023	225.631	6.122	0.206	0.018	172.426

6.068	0.086	0.023	225.631	6.102	0.186	0.015	146.024
6.066	0.082	0.022	218.952	6.122	0.214	0.012	119.755
6.070	0.082	0.023	225.631	6.116	0.198	0.013	126.310
6.082	0.062	0.026	252.435	6.088	0.198	0.014	139.444
6.086	0.070	0.024	239.016	6.102	0.226	0.015	146.024
6.088	0.070	0.026	252.435	6.102	0.246	0.016	159.208
6.078	0.082	0.024	239.016	6.100	0.198	0.021	205.617
6.080	0.074	0.026	252.435	6.084	0.158	0.024	232.320
6.064	0.082	0.026	252.435	6.072	0.178	0.020	198.962
6.064	0.078	0.026	259.156	6.084	0.142	0.022	212.280
6.070	0.074	0.024	239.016	6.100	0.182	0.024	232.320
6.078	0.070	0.026	252.435	6.112	0.178	0.030	292.890
6.082	0.066	0.027	265.886	6.104	0.170	0.029	286.126
6.084	0.074	0.026	259.156	6.088	0.154	0.028	272.625
6.086	0.070	0.029	286.126	6.122	0.230	0.024	232.320
6.082	0.070	0.028	279.371	6.122	0.222	0.026	259.156
6.078	0.070	0.026	259.156	6.122	0.202	0.024	239.016
6.076	0.074	0.025	245.721	6.122	0.218	0.020	198.962
6.068	0.078	0.026	259.156	6.122	0.226	0.020	192.315
6.072	0.074	0.026	252.435	6.122	0.270	0.020	198.962
6.080	0.074	0.026	252.435	6.122	0.270	0.022	212.280
6.078	0.078	0.026	252.435	6.122	0.270	0.022	212.280
6.070	0.082	0.025	245.721	6.122	0.222	0.022	218.952
6.070	0.082	0.025	245.721	6.114	0.218	0.020	198.962
6.076	0.086	0.023	225.631	6.122	0.210	0.018	179.047
6.070	0.090	0.022	212.280	6.118	0.230	0.020	192.315
6.074	0.078	0.024	239.016	6.116	0.206	0.020	198.962
6.068	0.082	0.023	225.631	6.088	0.134	0.016	159.208
6.070	0.082	0.022	212.280	6.088	0.134	0.018	172.426

6.072	0.086	0.021	205.617	6.082	0.130	0.017	165.813
6.068	0.086	0.021	205.617	6.084	0.114	0.017	165.813
6.068	0.086	0.021	205.617	6.090	0.122	0.016	152.612
6.066	0.090	0.020	192.315	6.078	0.122	0.016	159.208
6.058	0.090	0.021	205.617	6.082	0.110	0.017	165.813
6.064	0.086	0.023	225.631	6.076	0.142	0.018	179.047
6.062	0.086	0.022	212.280	6.072	0.146	0.016	159.208
6.058	0.090	0.020	198.962	6.032	0.154	0.014	132.873
6.060	0.086	0.021	205.617	6.054	0.130	0.013	126.310
6.062	0.086	0.021	205.617	6.062	0.122	0.015	146.024
6.060	0.090	0.020	192.315	6.064	0.142	0.014	139.444
6.062	0.090	0.020	198.962	6.082	0.150	0.015	146.024
6.064	0.094	0.022	218.952	6.070	0.134	0.016	152.612
6.066	0.098	0.023	225.631	6.052	0.134	0.015	146.024
6.070	0.094	0.024	232.320	6.074	0.126	0.014	139.444
6.070	0.094	0.022	218.952	6.084	0.158	0.017	165.813
6.062	0.090	0.023	225.631	6.076	0.142	0.020	192.315
6.060	0.102	0.022	212.280	6.086	0.126	0.020	198.962
6.066	0.102	0.020	192.315	6.072	0.134	0.020	198.962
6.072	0.102	0.021	205.617	6.078	0.142	0.019	185.677
6.074	0.114	0.021	205.617	6.086	0.146	0.018	172.426
6.072	0.118	0.020	198.962	6.080	0.142	0.018	172.426
6.066	0.138	0.019	185.677	6.080	0.146	0.018	172.426
6.072	0.118	0.022	218.952	6.082	0.142	0.018	179.047
6.076	0.118	0.022	218.952	6.086	0.158	0.016	152.612
6.068	0.122	0.022	212.280	6.086	0.134	0.018	172.426
6.074	0.126	0.021	205.617	6.080	0.166	0.018	179.047
6.072	0.130	0.020	198.962	6.110	0.202	0.016	152.612
6.076	0.118	0.022	212.280	6.108	0.186	0.017	165.813

6.074	0.122	0.022	212.280	6.102	0.202	0.017	165.813
6.074	0.126	0.021	205.617	6.110	0.198	0.016	159.208
6.070	0.118	0.022	212.280	6.104	0.186	0.018	172.426
6.072	0.118	0.020	198.962	6.096	0.158	0.019	185.677
6.064	0.114	0.021	205.617	6.092	0.162	0.019	185.677
6.070	0.114	0.020	192.315	6.118	0.202	0.016	159.208
6.074	0.118	0.020	198.962	6.104	0.202	0.018	172.426
6.076	0.130	0.020	198.962	6.090	0.230	0.017	165.813
6.072	0.130	0.020	192.315	6.090	0.178	0.018	172.426
6.076	0.130	0.020	192.315	6.068	0.082	0.022	218.952
6.076	0.138	0.018	179.047	6.066	0.082	0.022	212.280
6.078	0.130	0.018	179.047	6.064	0.086	0.020	192.315
6.076	0.134	0.020	198.962	6.064	0.086	0.021	205.617
6.078	0.134	0.020	198.962	6.064	0.082	0.024	232.320
6.076	0.134	0.020	198.962	6.066	0.078	0.022	218.952
6.066	0.134	0.020	192.315	6.068	0.082	0.021	205.617
6.072	0.134	0.018	179.047	6.070	0.082	0.022	212.280
6.070	0.126	0.019	185.677	6.072	0.082	0.022	218.952
6.070	0.122	0.020	192.315	6.064	0.086	0.021	205.617
6.066	0.126	0.021	205.617	6.066	0.086	0.022	218.952
6.068	0.126	0.020	192.315	6.068	0.082	0.022	218.952
6.064	0.130	0.018	172.426	6.070	0.082	0.021	205.617
6.064	0.134	0.016	159.208	6.064	0.086	0.019	185.677
6.062	0.134	0.016	159.208	6.056	0.078	0.020	192.315
6.068	0.150	0.014	132.873	6.052	0.078	0.014	132.873
6.062	0.138	0.014	132.873	6.054	0.070	0.016	159.208
6.066	0.130	0.015	146.024	6.066	0.082	0.015	146.024
6.050	0.146	0.014	132.873	6.072	0.090	0.018	179.047
6.072	0.130	0.016	152.612	6.084	0.090	0.024	232.320

6.086	0.146	0.018	179.047	6.080	0.098	0.022	212.280
6.082	0.138	0.020	192.315	6.076	0.114	0.020	198.962
6.080	0.130	0.020	198.962	6.070	0.110	0.021	205.617
6.076	0.142	0.021	205.617	6.068	0.106	0.021	205.617
6.080	0.134	0.021	205.617	6.072	0.106	0.020	198.962
6.074	0.166	0.019	185.677	6.068	0.110	0.020	192.315
6.080	0.154	0.017	165.813	6.072	0.110	0.020	192.315
6.082	0.142	0.018	172.426	6.072	0.102	0.020	192.315
6.074	0.146	0.019	185.677	6.076	0.110	0.020	192.315
6.084	0.166	0.016	152.612	6.074	0.130	0.018	179.047
6.084	0.134	0.018	172.426	6.074	0.118	0.020	198.962
6.082	0.150	0.020	198.962	6.072	0.122	0.020	192.315
6.086	0.170	0.019	185.677	6.082	0.130	0.020	192.315
6.092	0.154	0.020	192.315	6.090	0.138	0.020	192.315
6.098	0.190	0.018	179.047	6.084	0.138	0.020	192.315
6.082	0.166	0.020	192.315	6.082	0.134	0.018	179.047
6.088	0.158	0.020	192.315	6.078	0.142	0.016	159.208
6.082	0.146	0.020	192.315	6.078	0.154	0.016	152.612
6.084	0.154	0.018	172.426	6.078	0.122	0.016	152.612
6.098	0.194	0.016	159.208	6.080	0.114	0.014	139.444
6.088	0.182	0.018	179.047	6.076	0.070	0.032	320.027
6.080	0.186	0.018	179.047	6.070	0.074	0.032	313.230
6.070	0.146	0.016	159.208	6.070	0.078	0.029	286.126
6.070	0.146	0.014	139.444	6.072	0.078	0.029	286.126
6.080	0.162	0.014	132.873	6.068	0.078	0.028	272.625
6.098	0.182	0.014	139.444	6.068	0.078	0.029	286.126
6.082	0.186	0.016	152.612	6.062	0.082	0.027	265.886
6.070	0.178	0.017	165.813	6.058	0.086	0.026	259.156
6.072	0.182	0.016	152.612	6.066	0.082	0.027	265.886

6.090	0.174	0.016	152.612	6.060	0.086	0.024	239.016
6.072	0.162	0.018	179.047	6.070	0.082	0.027	265.886
6.074	0.150	0.023	225.631	6.084	0.066	0.028	279.371
6.082	0.158	0.025	245.721	6.068	0.086	0.028	272.625
6.084	0.150	0.025	245.721	6.068	0.082	0.030	292.890
6.108	0.174	0.023	225.631	6.072	0.078	0.030	292.890
6.118	0.198	0.022	212.280	6.066	0.082	0.028	279.371
6.100	0.186	0.021	205.617	6.068	0.082	0.030	292.890
6.118	0.222	0.018	172.426	6.072	0.074	0.031	306.442
6.112	0.214	0.018	179.047	6.064	0.082	0.030	299.662
6.110	0.198	0.018	179.047	6.060	0.082	0.029	286.126
6.116	0.206	0.018	172.426	6.068	0.082	0.027	265.886
6.122	0.202	0.018	179.047	6.068	0.078	0.028	272.625
6.116	0.202	0.019	185.677	6.068	0.074	0.026	259.156
6.112	0.226	0.019	185.677	6.068	0.074	0.027	265.886
6.114	0.222	0.018	179.047	6.074	0.074	0.027	265.886
6.104	0.182	0.020	192.315	6.076	0.070	0.028	279.371
6.112	0.194	0.020	192.315	6.080	0.070	0.029	286.126
6.118	0.206	0.021	205.617	6.078	0.078	0.028	279.371
6.108	0.218	0.022	212.280	6.076	0.078	0.028	279.371
6.120	0.222	0.022	212.280	6.082	0.066	0.027	265.886
6.122	0.210	0.020	198.962	6.074	0.074	0.026	252.435
6.122	0.206	0.021	205.617	6.078	0.074	0.024	232.320
6.122	0.206	0.022	218.952	6.076	0.074	0.024	232.320
6.122	0.202	0.024	232.320	6.074	0.078	0.024	232.320
6.122	0.210	0.024	232.320	6.068	0.086	0.022	218.952
6.122	0.218	0.024	232.320	6.068	0.086	0.022	218.952
6.122	0.226	0.024	232.320	6.072	0.082	0.022	218.952
6.122	0.218	0.024	239.016	6.074	0.082	0.022	218.952

6.122	0.210	0.024	239.016	6.066	0.086	0.022	212.280
6.122	0.226	0.024	239.016	6.068	0.082	0.021	205.617
6.122	0.222	0.023	225.631	6.062	0.150	0.014	132.873
6.122	0.230	0.024	239.016	6.076	0.166	0.013	126.310
6.122	0.218	0.023	225.631	6.118	0.234	0.014	139.444
6.074	0.062	0.035	347.298	6.102	0.202	0.020	192.315
6.066	0.082	0.032	320.027	6.092	0.158	0.022	218.952
6.082	0.074	0.032	313.230	6.088	0.178	0.021	205.617
6.082	0.070	0.032	313.230	6.096	0.198	0.021	205.617
6.080	0.070	0.032	313.230	6.106	0.214	0.020	192.315
6.078	0.078	0.026	259.156	6.122	0.202	0.022	218.952
6.074	0.082	0.027	265.886	6.122	0.222	0.028	272.625
6.078	0.078	0.027	265.886	6.122	0.190	0.029	286.126
6.080	0.074	0.027	265.886	6.122	0.194	0.024	232.320
6.082	0.066	0.029	286.126	6.122	0.198	0.021	205.617
6.074	0.078	0.028	279.371	6.122	0.222	0.022	218.952
6.066	0.082	0.028	272.625	6.122	0.210	0.025	245.721
6.072	0.078	0.028	272.625	6.122	0.230	0.026	252.435
6.064	0.078	0.028	279.371	6.122	0.234	0.024	239.016
6.064	0.078	0.029	286.126	6.122	0.234	0.024	232.320
6.074	0.070	0.030	299.662	6.122	0.226	0.022	218.952
6.080	0.070	0.030	299.662	6.122	0.230	0.022	212.280
6.074	0.074	0.030	299.662	6.122	0.234	0.020	192.315
6.084	0.066	0.029	286.126	6.122	0.230	0.020	192.315
6.078	0.074	0.029	286.126	6.122	0.234	0.023	225.631
6.078	0.078	0.028	272.625	6.122	0.226	0.022	218.952
6.068	0.086	0.027	265.886	6.090	0.058	0.032	313.230
6.072	0.082	0.027	265.886	6.090	0.062	0.027	265.886
6.068	0.086	0.028	272.625	6.088	0.066	0.024	239.016

6.078	0.082	0.028	272.625	6.084	0.058	0.022	218.952
6.084	0.074	0.029	286.126	6.060	0.074	0.022	218.952
6.066	0.090	0.026	259.156	6.046	0.078	0.021	205.617
6.088	0.062	0.030	299.662	6.050	0.074	0.024	239.016
6.088	0.062	0.031	306.442	6.062	0.066	0.026	259.156
6.060	0.090	0.027	265.886	6.064	0.062	0.029	286.126
6.072	0.086	0.026	252.435	6.068	0.062	0.033	326.832
6.070	0.082	0.026	259.156	6.064	0.074	0.030	292.890
6.068	0.086	0.024	232.320	6.062	0.082	0.028	279.371
6.076	0.070	0.024	239.016	6.068	0.078	0.028	279.371
6.074	0.066	0.026	252.435	6.060	0.078	0.030	299.662
6.054	0.086	0.023	225.631	6.062	0.074	0.032	320.027
6.076	0.070	0.024	239.016	6.066	0.074	0.032	313.230
6.080	0.066	0.028	272.625	6.048	0.146	0.014	132.873
6.074	0.074	0.028	272.625	6.054	0.166	0.014	139.444
6.080	0.066	0.032	320.027	6.066	0.190	0.016	152.612
6.082	0.066	0.032	313.230	6.080	0.170	0.018	179.047
6.080	0.066	0.032	313.230	6.066	0.150	0.020	198.962
6.082	0.066	0.030	299.662	6.080	0.162	0.018	179.047
6.082	0.066	0.031	306.442	6.086	0.162	0.018	179.047
6.074	0.086	0.028	272.625	6.080	0.150	0.019	185.677
6.080	0.070	0.028	279.371	6.072	0.142	0.020	192.315
6.072	0.074	0.028	279.371	6.078	0.158	0.018	179.047
6.072	0.074	0.024	239.016	6.080	0.142	0.016	159.208
6.070	0.082	0.022	218.952	6.084	0.142	0.016	159.208
6.066	0.086	0.022	218.952	6.078	0.162	0.019	185.677
6.072	0.082	0.023	225.631	6.092	0.186	0.018	172.426
6.070	0.086	0.023	225.631	6.102	0.182	0.018	172.426
6.070	0.082	0.025	245.721	6.082	0.210	0.017	165.813

6.076	0.078	0.025	245.721	6.092	0.190	0.017	165.813
6.070	0.086	0.022	212.280	6.100	0.182	0.018	172.426
6.068	0.086	0.022	218.952	6.096	0.178	0.018	172.426
6.070	0.078	0.024	239.016	6.110	0.202	0.016	159.208
6.066	0.082	0.024	232.320	6.104	0.226	0.017	165.813
6.064	0.086	0.022	212.280	6.080	0.214	0.016	159.208
6.064	0.090	0.022	218.952	6.082	0.206	0.016	152.612
6.056	0.086	0.024	239.016	6.090	0.206	0.016	152.612
6.062	0.086	0.023	225.631	6.096	0.214	0.018	179.047
6.064	0.086	0.022	212.280	6.098	0.202	0.021	205.617
6.064	0.090	0.021	205.617	6.100	0.198	0.018	179.047
6.070	0.090	0.022	212.280	6.078	0.182	0.014	139.444
6.066	0.086	0.022	218.952	6.104	0.202	0.012	119.755
6.066	0.094	0.022	212.280	6.122	0.230	0.014	132.873
6.070	0.098	0.023	225.631	6.122	0.206	0.018	172.426
6.072	0.094	0.024	239.016	6.104	0.206	0.018	179.047
6.072	0.086	0.025	245.721	6.116	0.202	0.018	179.047
6.070	0.086	0.025	245.721	6.122	0.218	0.018	179.047
6.064	0.090	0.024	239.016	6.116	0.214	0.020	192.315
6.062	0.094	0.024	239.016	6.122	0.214	0.021	205.617
6.060	0.094	0.021	205.617	6.122	0.182	0.020	198.962
6.054	0.090	0.022	212.280	6.122	0.206	0.018	179.047
6.062	0.098	0.023	225.631	6.122	0.218	0.018	172.426
6.066	0.106	0.022	218.952	6.082	0.202	0.015	146.024
6.068	0.110	0.022	218.952	6.072	0.082	0.028	272.625
6.074	0.102	0.023	225.631	6.072	0.078	0.028	272.625
6.070	0.106	0.023	225.631	6.068	0.082	0.028	272.625
6.072	0.106	0.024	232.320	6.062	0.086	0.027	265.886
6.076	0.114	0.021	205.617	6.074	0.078	0.025	245.721

6.070	0.110	0.022	212.280	6.084	0.070	0.025	245.721
6.074	0.110	0.022	212.280	6.090	0.066	0.026	259.156
6.070	0.110	0.021	205.617	6.084	0.070	0.027	265.886
6.066	0.110	0.021	205.617	6.086	0.074	0.028	272.625
6.064	0.114	0.020	192.315	6.080	0.074	0.028	279.371
6.064	0.110	0.018	179.047	6.080	0.074	0.027	265.886
6.064	0.106	0.020	192.315	6.070	0.086	0.026	252.435
6.072	0.110	0.020	198.962	6.070	0.082	0.026	252.435
6.070	0.110	0.021	205.617	6.080	0.074	0.024	239.016
6.074	0.118	0.021	205.617	6.072	0.074	0.024	239.016
6.076	0.118	0.022	212.280	6.072	0.078	0.022	218.952
6.074	0.122	0.022	212.280	6.068	0.082	0.022	212.280
6.070	0.130	0.020	198.962	6.068	0.082	0.022	212.280
6.066	0.118	0.018	179.047	6.072	0.082	0.022	218.952
6.068	0.118	0.020	198.962	6.070	0.082	0.023	225.631
6.072	0.118	0.020	192.315	6.074	0.078	0.023	225.631
6.074	0.118	0.021	205.617	6.078	0.074	0.024	232.320
6.068	0.114	0.022	212.280	6.072	0.086	0.020	198.962
6.068	0.122	0.018	179.047	6.072	0.082	0.021	205.617
6.062	0.118	0.018	179.047	6.070	0.082	0.023	225.631
6.068	0.114	0.018	172.426	6.068	0.082	0.022	212.280
6.066	0.118	0.018	172.426	6.064	0.086	0.019	185.677
6.060	0.118	0.016	159.208	6.060	0.086	0.020	198.962
6.062	0.130	0.016	159.208	6.068	0.082	0.023	225.631
6.068	0.118	0.018	179.047	6.072	0.078	0.022	212.280
6.068	0.126	0.020	192.315	6.066	0.082	0.020	198.962
6.070	0.134	0.018	172.426	6.068	0.086	0.020	198.962
6.070	0.122	0.019	185.677	6.072	0.082	0.021	205.617
6.070	0.130	0.018	179.047	6.066	0.086	0.020	198.962

6.080	0.134	0.020	192.315	6.064	0.086	0.022	218.952
6.084	0.142	0.020	192.315	6.068	0.090	0.023	225.631
6.078	0.134	0.021	205.617	6.072	0.090	0.024	232.320
6.074	0.142	0.017	165.813	6.070	0.086	0.024	232.320
6.078	0.158	0.016	159.208	6.070	0.082	0.024	239.016
6.080	0.146	0.019	185.677	6.066	0.086	0.023	225.631
6.072	0.154	0.018	172.426	6.062	0.086	0.024	239.016
6.074	0.154	0.018	172.426	6.064	0.094	0.021	205.617
6.074	0.146	0.018	172.426	6.056	0.086	0.022	212.280
6.086	0.146	0.016	159.208	6.062	0.090	0.021	205.617
6.086	0.150	0.018	179.047	6.060	0.098	0.021	205.617
6.092	0.154	0.018	179.047	6.062	0.098	0.021	205.617
6.084	0.130	0.019	185.677	6.066	0.094	0.021	205.617
6.080	0.142	0.021	205.617	6.070	0.094	0.021	205.617
6.084	0.162	0.018	172.426	6.068	0.094	0.023	225.631
6.094	0.154	0.018	179.047	6.070	0.106	0.020	198.962
6.092	0.182	0.018	172.426	6.072	0.106	0.020	198.962
6.082	0.162	0.019	185.677	6.070	0.098	0.022	212.280
6.094	0.154	0.019	185.677	6.072	0.106	0.021	205.617
6.080	0.134	0.019	185.677	6.070	0.110	0.020	198.962
6.080	0.154	0.015	146.024	6.066	0.110	0.020	192.315
6.106	0.202	0.014	132.873	6.074	0.106	0.020	192.315
6.094	0.182	0.018	172.426	6.074	0.110	0.020	192.315
6.080	0.178	0.018	172.426	6.076	0.106	0.021	205.617
6.068	0.142	0.017	165.813	6.074	0.102	0.022	218.952
6.078	0.130	0.017	165.813	6.074	0.110	0.021	205.617
6.078	0.142	0.015	146.024	6.076	0.110	0.022	218.952
6.082	0.138	0.016	152.612	6.072	0.110	0.021	205.617
6.070	0.134	0.016	152.612	6.058	0.122	0.018	172.426

6.080	0.158	0.016	159.208	6.052	0.110	0.016	159.208
6.092	0.158	0.017	165.813	6.068	0.110	0.016	152.612
6.090	0.166	0.019	185.677	6.076	0.102	0.014	139.444
6.078	0.138	0.022	212.280	6.078	0.110	0.015	146.024
6.080	0.146	0.025	245.721	6.064	0.130	0.014	139.444
6.086	0.154	0.024	239.016	6.068	0.118	0.014	139.444
6.088	0.154	0.024	232.320	6.064	0.102	0.018	179.047
6.096	0.162	0.022	212.280	6.064	0.110	0.019	185.677
6.110	0.194	0.019	185.677	6.054	0.122	0.018	179.047
6.106	0.174	0.020	198.962	6.064	0.094	0.016	152.612
6.120	0.202	0.018	179.047	6.068	0.114	0.013	126.310
6.110	0.202	0.018	179.047	6.068	0.138	0.016	159.208
6.106	0.198	0.019	185.677	6.056	0.150	0.016	159.208
6.104	0.194	0.019	185.677	6.054	0.138	0.016	159.208
6.116	0.210	0.018	172.426	6.058	0.146	0.016	159.208
6.118	0.190	0.020	198.962	6.058	0.146	0.017	165.813
6.100	0.202	0.021	205.617	6.054	0.138	0.018	172.426
6.102	0.202	0.020	192.315	6.076	0.138	0.020	192.315
6.102	0.182	0.020	198.962	6.074	0.134	0.020	192.315
6.104	0.194	0.020	198.962	6.078	0.138	0.018	179.047
6.106	0.198	0.020	198.962	6.094	0.178	0.016	152.612
6.106	0.202	0.022	212.280	6.102	0.206	0.016	152.612
6.116	0.210	0.022	218.952	6.088	0.194	0.017	165.813
6.116	0.206	0.022	212.280	6.094	0.186	0.016	152.612
6.122	0.202	0.022	218.952	6.086	0.170	0.016	152.612
6.122	0.222	0.022	212.280	6.096	0.194	0.016	152.612
6.120	0.206	0.023	225.631	6.088	0.170	0.017	165.813
6.122	0.218	0.023	225.631	6.090	0.146	0.016	152.612
6.122	0.222	0.023	225.631	6.082	0.154	0.015	146.024

6.122	0.226	0.024	232.320	6.088	0.170	0.017	165.813
6.122	0.214	0.025	245.721	6.096	0.178	0.018	172.426
6.118	0.214	0.024	232.320	6.098	0.190	0.018	179.047
6.122	0.218	0.024	232.320	6.086	0.162	0.020	192.315
6.118	0.202	0.023	225.631	6.100	0.186	0.020	198.962
6.118	0.234	0.022	218.952	6.096	0.182	0.021	205.617
6.122	0.218	0.022	218.952	6.088	0.158	0.022	218.952
6.094	0.070	0.030	299.662	6.106	0.174	0.021	205.617
6.106	0.054	0.030	292.890	6.118	0.198	0.020	198.962
6.102	0.062	0.027	265.886	6.116	0.198	0.019	185.677
6.090	0.070	0.023	225.631	6.116	0.202	0.019	185.677
6.082	0.070	0.026	252.435	6.114	0.198	0.019	185.677
6.074	0.074	0.022	218.952	6.094	0.210	0.018	179.047
6.066	0.078	0.025	245.721	6.106	0.218	0.017	165.813
6.066	0.086	0.023	225.631	6.112	0.242	0.017	165.813
6.064	0.086	0.025	245.721	6.110	0.198	0.019	185.677
6.076	0.066	0.030	292.890	6.096	0.218	0.019	185.677
6.070	0.074	0.030	299.662	6.088	0.214	0.019	185.677
6.064	0.082	0.028	279.371	6.094	0.190	0.020	192.315
6.068	0.082	0.027	265.886	6.104	0.202	0.020	198.962
6.064	0.078	0.029	286.126	6.096	0.202	0.020	198.962
6.062	0.078	0.030	299.662	6.112	0.198	0.021	205.617
6.072	0.070	0.033	326.832	6.112	0.210	0.020	192.315
6.074	0.070	0.032	320.027	6.116	0.198	0.020	198.962
6.070	0.074	0.032	320.027	6.122	0.194	0.022	218.952
6.070	0.078	0.031	306.442	6.118	0.206	0.022	218.952
6.074	0.074	0.032	313.230	6.120	0.190	0.024	232.320
6.072	0.078	0.030	292.890	6.122	0.206	0.023	225.631
6.066	0.078	0.030	292.890	6.122	0.210	0.024	232.320

6.064	0.078	0.031	306.442	6.118	0.218	0.024	239.016
6.068	0.082	0.030	292.890	6.122	0.206	0.025	245.721
6.070	0.086	0.029	286.126	6.122	0.206	0.024	239.016
6.060	0.094	0.027	265.886	6.122	0.222	0.024	232.320
6.066	0.090	0.027	265.886	6.120	0.222	0.022	218.952
6.058	0.086	0.029	286.126	6.112	0.226	0.023	225.631
6.056	0.094	0.028	272.625	6.122	0.214	0.022	218.952
6.056	0.090	0.028	272.625	6.074	0.062	0.030	299.662
6.074	0.082	0.026	259.156	6.066	0.074	0.028	279.371
6.072	0.078	0.027	265.886	6.074	0.070	0.031	306.442
6.074	0.090	0.024	239.016	6.076	0.070	0.030	299.662
6.082	0.070	0.025	245.721	6.058	0.086	0.028	272.625
6.084	0.058	0.028	272.625	6.060	0.086	0.026	252.435
6.084	0.062	0.026	252.435	6.060	0.090	0.024	239.016
6.078	0.066	0.024	232.320	6.066	0.090	0.024	232.320
6.088	0.054	0.026	252.435	6.054	0.090	0.021	205.617
6.082	0.058	0.027	265.886	6.078	0.066	0.026	252.435
6.078	0.066	0.028	279.371	6.072	0.074	0.027	265.886
6.082	0.066	0.030	292.890	6.066	0.082	0.024	239.016
6.066	0.082	0.028	279.371	6.072	0.078	0.025	245.721
6.086	0.062	0.031	306.442	6.062	0.078	0.026	259.156
6.068	0.082	0.029	286.126	6.062	0.078	0.028	272.625
6.074	0.086	0.028	272.625	6.070	0.070	0.029	286.126
6.088	0.058	0.028	279.371	6.072	0.070	0.030	299.662
6.072	0.082	0.027	265.886	6.070	0.074	0.030	292.890
6.076	0.082	0.026	252.435	6.070	0.078	0.029	286.126
6.072	0.086	0.024	232.320	6.070	0.074	0.030	292.890
6.074	0.082	0.023	225.631	6.066	0.074	0.028	279.371
6.074	0.078	0.024	232.320	6.066	0.078	0.028	279.371

6.074	0.078	0.024	232.320	6.062	0.078	0.028	272.625
6.078	0.074	0.024	239.016	6.062	0.086	0.027	265.886
6.078	0.074	0.024	232.320	6.066	0.082	0.028	272.625
6.070	0.086	0.021	205.617	6.056	0.090	0.026	252.435
6.072	0.082	0.022	218.952	6.062	0.082	0.027	265.886
6.078	0.074	0.023	225.631	6.062	0.082	0.028	272.625
6.072	0.082	0.022	212.280	6.060	0.082	0.029	286.126
6.068	0.086	0.021	205.617	6.058	0.078	0.028	279.371
6.064	0.090	0.022	218.952	6.064	0.078	0.028	279.371
6.066	0.086	0.023	225.631	6.070	0.082	0.027	265.886
6.072	0.078	0.024	232.320	6.070	0.082	0.022	218.952
6.070	0.086	0.022	218.952	6.066	0.082	0.022	218.952
6.068	0.086	0.022	218.952	6.066	0.082	0.022	218.952
6.070	0.082	0.024	232.320	6.068	0.086	0.022	218.952
6.066	0.078	0.025	245.721	6.072	0.078	0.023	225.631
6.062	0.078	0.025	245.721	6.076	0.078	0.024	232.320
6.062	0.074	0.026	252.435	6.070	0.082	0.022	212.280
6.058	0.078	0.025	245.721	6.072	0.078	0.023	225.631
6.058	0.082	0.022	218.952	6.072	0.078	0.024	239.016
6.054	0.078	0.021	205.617	6.068	0.082	0.023	225.631
6.062	0.074	0.020	198.962	6.068	0.086	0.021	205.617
6.062	0.082	0.024	232.320	6.068	0.086	0.022	218.952
6.064	0.086	0.024	232.320	6.062	0.086	0.024	239.016
6.060	0.090	0.023	225.631	6.068	0.082	0.024	232.320
6.064	0.094	0.025	245.721	6.070	0.082	0.022	218.952
6.064	0.102	0.023	225.631	6.066	0.078	0.021	205.617
6.064	0.106	0.024	232.320	6.064	0.082	0.020	192.315
6.066	0.106	0.023	225.631	6.044	0.082	0.017	165.813
6.072	0.102	0.022	218.952	6.056	0.098	0.016	152.612

6.066	0.114	0.020	198.962	6.064	0.106	0.020	198.962
6.068	0.110	0.020	192.315	6.078	0.094	0.022	212.280
6.076	0.110	0.021	205.617	6.078	0.094	0.023	225.631
6.070	0.106	0.022	212.280	6.076	0.082	0.024	232.320
6.064	0.106	0.020	198.962	6.074	0.086	0.023	225.631
6.066	0.106	0.020	192.315	6.070	0.090	0.026	252.435
6.068	0.110	0.020	192.315	6.072	0.098	0.024	239.016
6.072	0.106	0.021	205.617	6.068	0.090	0.024	239.016
6.072	0.110	0.020	198.962	6.072	0.098	0.024	232.320
6.078	0.110	0.021	205.617	6.072	0.110	0.022	218.952
6.076	0.122	0.021	205.617	6.070	0.106	0.023	225.631
6.070	0.130	0.019	185.677	6.070	0.102	0.022	218.952
6.076	0.122	0.020	192.315	6.074	0.106	0.022	212.280
6.074	0.126	0.019	185.677	6.070	0.110	0.020	198.962
6.074	0.130	0.020	192.315	6.068	0.106	0.020	192.315
6.076	0.126	0.020	192.315	6.074	0.106	0.020	192.315
6.076	0.130	0.021	205.617	6.070	0.098	0.021	205.617
6.082	0.122	0.022	212.280	6.068	0.110	0.021	205.617
6.082	0.122	0.023	225.631	6.068	0.114	0.020	198.962
6.076	0.106	0.024	239.016	6.068	0.114	0.020	198.962
6.070	0.102	0.024	232.320	6.070	0.110	0.020	198.962
6.078	0.114	0.022	212.280	6.068	0.110	0.020	198.962
6.074	0.110	0.020	192.315	6.068	0.118	0.020	192.315
6.078	0.122	0.020	192.315	6.072	0.122	0.020	192.315
6.070	0.122	0.018	179.047	6.072	0.122	0.020	192.315
6.070	0.122	0.017	165.813	6.074	0.114	0.020	198.962
6.082	0.138	0.017	165.813	6.074	0.122	0.020	192.315
6.086	0.146	0.018	172.426	6.080	0.122	0.020	198.962
6.084	0.146	0.018	172.426	6.080	0.118	0.021	205.617

6.084	0.134	0.018	172.426	6.078	0.114	0.021	205.617
6.056	0.138	0.016	159.208	6.078	0.122	0.022	212.280
6.052	0.154	0.014	139.444	6.076	0.114	0.020	198.962
6.064	0.142	0.014	139.444	6.072	0.106	0.020	198.962
6.064	0.130	0.016	152.612	6.076	0.114	0.019	185.677
6.072	0.146	0.016	159.208	6.074	0.118	0.019	185.677
6.082	0.146	0.017	165.813	6.076	0.114	0.019	185.677
6.074	0.154	0.019	185.677	6.076	0.126	0.019	185.677
6.060	0.150	0.018	179.047	6.072	0.134	0.018	172.426
6.068	0.138	0.018	172.426	6.066	0.122	0.016	159.208
6.080	0.138	0.018	179.047	6.058	0.118	0.015	146.024
6.088	0.146	0.020	192.315	6.056	0.134	0.015	146.024
6.082	0.134	0.021	205.617	6.062	0.146	0.014	139.444
6.084	0.130	0.020	192.315	6.070	0.134	0.015	146.024
6.082	0.130	0.018	179.047	6.070	0.130	0.016	152.612
6.082	0.150	0.020	192.315	6.070	0.142	0.016	159.208
6.084	0.158	0.018	179.047	6.074	0.142	0.017	165.813
6.086	0.162	0.018	172.426	6.076	0.134	0.017	165.813
6.094	0.178	0.017	165.813	6.072	0.146	0.017	165.813
6.080	0.150	0.018	172.426	6.076	0.138	0.017	165.813
6.082	0.138	0.019	185.677	6.082	0.150	0.018	179.047
6.082	0.138	0.020	198.962	6.084	0.138	0.020	192.315
6.084	0.150	0.019	185.677	6.082	0.142	0.020	198.962
6.096	0.186	0.017	165.813	6.078	0.134	0.020	192.315
6.092	0.178	0.018	179.047	6.082	0.142	0.019	185.677
6.094	0.186	0.017	165.813	6.082	0.138	0.020	192.315
6.076	0.162	0.016	152.612	6.080	0.142	0.018	179.047
6.080	0.150	0.014	139.444	6.080	0.130	0.018	179.047
6.090	0.150	0.015	146.024	6.080	0.146	0.020	192.315

6.094	0.150	0.016	159.208	6.086	0.166	0.016	159.208
6.080	0.146	0.018	179.047	6.098	0.166	0.016	159.208
6.078	0.154	0.019	185.677	6.094	0.182	0.017	165.813
6.070	0.154	0.019	185.677	6.070	0.066	0.033	326.832
6.076	0.142	0.019	185.677	6.072	0.066	0.034	333.646
6.076	0.142	0.019	185.677	6.068	0.074	0.033	326.832
6.072	0.146	0.022	212.280	6.064	0.082	0.030	299.662
6.086	0.150	0.020	198.962	6.070	0.078	0.030	299.662
6.096	0.162	0.022	218.952	6.062	0.078	0.031	306.442
6.094	0.166	0.023	225.631	6.062	0.078	0.032	313.230
6.096	0.174	0.023	225.631	6.070	0.070	0.033	326.832
6.094	0.166	0.024	232.320	6.074	0.070	0.032	320.027
6.110	0.214	0.020	198.962	6.070	0.070	0.033	326.832
6.110	0.190	0.020	198.962	6.068	0.074	0.031	306.442
6.102	0.190	0.020	198.962	6.068	0.074	0.030	299.662
6.102	0.194	0.019	185.677	6.066	0.074	0.030	299.662
6.114	0.214	0.018	179.047	6.058	0.082	0.029	286.126
6.106	0.190	0.022	212.280	6.062	0.082	0.029	286.126
6.102	0.190	0.023	225.631	6.064	0.086	0.030	299.662
6.100	0.190	0.020	198.962	6.062	0.086	0.028	272.625
6.096	0.182	0.020	192.315	6.058	0.090	0.027	265.886
6.100	0.194	0.018	179.047	6.062	0.082	0.030	292.890
6.108	0.210	0.020	192.315	6.064	0.082	0.031	306.442
6.112	0.194	0.022	218.952	6.060	0.090	0.030	292.890
6.114	0.202	0.022	212.280	6.058	0.086	0.030	292.890
6.114	0.190	0.021	205.617	6.066	0.086	0.028	279.371
6.122	0.194	0.022	218.952	6.072	0.082	0.029	286.126
6.116	0.218	0.022	212.280	6.072	0.086	0.026	259.156
6.120	0.194	0.024	232.320	6.072	0.082	0.026	252.435

6.122	0.206	0.023	225.631	6.082	0.066	0.029	286.126
6.122	0.222	0.023	225.631	6.078	0.070	0.027	265.886
6.122	0.218	0.024	239.016	6.078	0.066	0.026	259.156
6.120	0.214	0.024	239.016	6.082	0.066	0.027	265.886
6.120	0.210	0.024	232.320	6.086	0.062	0.028	279.371
6.120	0.210	0.023	225.631	6.084	0.070	0.029	286.126
6.114	0.198	0.022	218.952	6.086	0.070	0.029	286.126
6.122	0.214	0.023	225.631	6.082	0.070	0.030	299.662
6.114	0.202	0.023	225.631	6.080	0.074	0.030	299.662
6.048	0.070	0.024	232.320	6.070	0.082	0.030	292.890
6.060	0.062	0.029	286.126	6.070	0.086	0.027	265.886
6.064	0.062	0.031	306.442	6.078	0.074	0.026	259.156
6.068	0.058	0.030	299.662	6.072	0.078	0.025	245.721
6.066	0.062	0.033	326.832	6.072	0.078	0.024	232.320
6.050	0.074	0.030	299.662	6.068	0.070	0.031	306.442
6.054	0.082	0.030	299.662				

REFERENCES

Alain, F. (1994). Simulation of Imaging Fourier Transform Spectrometers Using DIRSIG, MS Thesis.

Arnold, J. R. (1979). Ice in the lunar polar regions. *Journal of Geophysical Research: Solid Earth (1978–2012)*, *84*(B10), 5659-5668.

Bandfield, J. L., Glotch, T. D., & Christensen, P. R. (2003). Spectroscopic Identification of Carbonate Minerals in the Martian Dust. *Science*, *301(5636)*, 1084–1087.

Bandfield, J. L., Hayne, P. O., Williams, J.-P., Greenhagen, B. T., & Paige, D. A. (2015). Lunar surface roughness derived from LRO Diviner Radiometer observations. Icarus, 248, 357–372.

Bandfield, J. L., Poston, M. J., Klima, R. L., & Edwards, C. S. (2018). Widespread distribution of OH/H 2 O on the lunar surface inferred from spectral data. *Nature Geoscience*, 11(3), 173–177.

Barducci, A., De Cosmo, V., Marcoionni, P., & Pippi, I. (2004). ALISEO: a new stationary imaging interferometer. In S. S. Shen & P. E. Lewis (Eds.), (Vol. 5546, pp. 262–9). Presented at the Optical Science and Technology, the SPIE 49th Annual Meeting, SPIE.

Bartholomew, R. F., Butler, B. L., Hoover, H. L., And Wu, C. K. (1980). Infrared Spectra of a Water-Containing Glass. *Journal of the American Ceramic Society, 63(9-10)*, 481–485.

Becklin E. E. and Moon L.J. (2001). Stratospheric Observatory for Infrared Astronomy (SOFIA). *Advances in Space Research 33rd COSPAR Scientific Assembly, Elsevier Science Ltd.,* 30(9), 357-363.

Benna, M., Hurley, D. M., Stubbs, T. J., Mahaffy, P. R., & Elphic, R. C. (2019). Lunar soil hydration constrained by exospheric water liberated by meteoroid impacts. *Nature Geoscience*, 12(5), 333–338.

Bradley, J. P., Ishii, H. A., Gillis-Davis, J. J., Ciston, J., Nielsen, M. H., Bechtel, H. A., & Martin, M. C. (2014). Detection of solar wind-produced water in irradiated rims on silicate minerals. *Proceedings of the National Academy of Sciences*, *111*(5), 1732–1735.

Briottet, X., Boucher, Y., Dimmeler, A., Malaplate, A., Cini, A., Diani, M., et al. (2006). Military applications of hyperspectral imagery. In W. R. Watkins & D. Clement (Eds.), *Targets and Backgrounds XII: Characterization and Representation* (Vol. 6239, p. 62390B). International Society for Optics and Photonics.

Bruno, N., Caltabiano, T., Giammanco, S., & Romano, R. (2001). Degassing of SO2 and CO2 at Mount Etna (Sicily) as an indicator of pre-eruptive ascent and shallow emplacement of magma. *Journal of Volcanology and Geothermal Research*, *110*, 137–153.

Bufton, Daniel, and Harold Yorke. "Water Vapor Monitor." *SOFIA Science Center*, NASA/DLR SOFIA, 2018, www.sofia.usra.edu/science/instruments/water-vapor-monitor.

Bufton, Daniel, and Harold Yorke. "Why Chop and Nod with FORCAST." *SOFIA Science Center*, NASA/DLR SOFIA, 2016, www.sofia.usra.edu/science/proposing-and-observing/proposal-calls/cycle-4/cycle-4-phase-ii/why-chop-and-nod-forcast.

Cadenhead, D. A., Brown, M. G., Rice, D. K., & Stetter, J. R. (1977). Some surface area and porosity characterization of lunar soils. *Proc. Lunar Sci. Conf. 8th,* 1291–1303.

Campbell J.B. and. Wynne R.H. (2011). "History and Scope of Remote Sensing." *Introduction to Remote Sensing*, Guilford Press, 2011, p. 4.

Caulfield, H. J. (1979). Spectroscopy. Handbook of Optical Holography, Academic, 587–594.

Clark, R. N. (2009). Detection of Adsorbed Water and Hydroxyl on the Moon. *Science*, *326*(5952), 562-564.

Crites, S. T., Lucey, P. G., Wright, R., Chan, J., Garbeil, H., Horton, K. A., et al. (2014). Design and operation of SUCHI: the space ultra-compact hyperspectral imager for a small satellite, (012506), 908505.

Crites, S. T., Lucey, P. G., Wright, R., Garbeil, H., Horton, K. A., & Wood, M. (2012). A low cost thermal infrared hyperspectral imager for small satellites. *SPIE Sensors and Systems for Space Applications V*, 838509.

Cushing, M. C., Vacca, W. D., & Rayner, J. T. (2004). Spextool: A Spectral Extraction Package for SpeX, a 0.8–5.5 Mm Cross-Dispersed Spectrograph. Publications of the Astronomical Society of the Pacific, 116(818), 362–376.

Daily CO2. https://www.co2.earth/daily-co2

Daly, R. T., & Schultz, P. H. (2018). The delivery of water by impacts from planetary accretion to present. *Science Advances*, 4(4), 1–11.

Dyar, M. D., Hibbitts, C. A., Orlando, T. M. (2010). Mechanisms for incorporation of hydrogen in and on terrestrial planetary surfaces. *Icarus 208*, 425–437.

Evans, R. (2015). Three Types of Spectrums (Spectra). *Thecuriousastronomer*. thecuriousastronomer.wordpress.com/2013/07/09/three-types-of-spectrums-spectra/.

Falk, M. (1984). The frequency of the H-O-H bending fundamental in solids and liquids. Spectrochimica Acta, 40A, 43-48.

Farrell, W. M., Hurley, D. M., Esposito, V. J., McLain, J. L., & Zimmerman, M. I. (2017). The statistical mechanics of solar wind hydroxylation at the Moon, within lunar magnetic anomalies, and at Phobos. *Journal of Geophysical Research: Planets*, 122(1), 269–289.

Feldman, W. C., Maurice, S., Binder, A. B., Barraclough, B. L., Elphic, R. C., & Lawrence, D. J. (1998). Fluxes of Fast and Epithermal Neutrons from Lunar Prospector: Evidence for Water Ice at the Lunar Poles. *Science*, 281(5382), 1496–1500.

Gabrieli, A., Wright, R., Lucey, P. G., Porter, J. N., Garbeil, H., Pilger, E., & Wood, M. (2016). Characterization and initial field test of an 8–14 μm thermal infrared hyperspectral imager for measuring SO2 in volcanic plumes. *Bulletin of Volcanology*, *73*(78), 1–13.

Gladstone, G. R., Stern, S. A., Retherford, K. D., Black, R. K., Slater, D. C., Davis, M. W., et al. (2010). LAMP: The Lyman Alpha Mapping Project on NASA's Lunar Reconnaissance Orbiter Mission. *Space Science Reviews*, 150(1-4), 161–181.

Glew, D. N., & Rath, N. S. (1971). H2O, HDO, and CH3OH Infrared Spectra and Correlation with Solvent Basicity and Hydrogen Bonding. *Canadian Journal of Chemistry,* 837-856.

Goetz, A. F. H., Vane, G., Solomon, J. E., & Rock, B. N. (1985). Imaging Spectrometry for Earth Remote Sensing. *Science*, *228*, 1147–1153.

Griffiths, P. R. and de Haseth, J. A. (1986). Fourier Transform Infrared Spectroscopy, Vol. 83 of Chemical Analysis, Wiley.

Gruen, D.M., Wright, R.B., McBeth, R.L., Sheft, I. (1975). Hydroxyl formation accompanying defect center production in proton and deuteron bombarded aluminum oxide. J. Chem. Phys. 62 (3), 1192–1193.

Grumpe, A., Wöhler, C., Berezhnoy, A. A., & Shevchenko, V. V. (2019). Time-of-day-dependent behavior of surficial lunar hydroxyl/water: Observations and modeling. *Icarus*, 321, 486–507.

Guermazi, M., Thevenard, P., Brenier, R. (1987). Ion implantation effects in TiO_2 bombarded with protons and deuterons. Nucl. Instrum. Methods Phys. Res. B19/20, 912–916.

Hapke, B. (1965), Effects of a simulated solar wind on the photometric properties of rocks and powders. *Ann. NY Acad. Sci. 123*, 711–721.

Hapke, B. (1981). Bidirectional reflectance spectroscopy: 1. Theory. Journal of Geophysical Research: Planets, 86(B4), 3039–3054. http://doi.org/10.1029/JB086iB04p03039Heiken etal., 1991

Hapke, B. (1993). Theory of Reflectance and Emittance Spectroscopy. *Cambridge Univ. Press.*

Harmon, J. K., and Slade, M. A. (1992). Radar Mapping of Mercury: Full-Disk Images and Polar Anomalies. *American Association for the Advancement of Science*, 258, 640–643.

Hayne, P. O., Hendrix, A., Sefton-Nash, E., Siegler, M. A., Lucey, P. G., Retherford, K. D., et al. (2015). Evidence for exposed water ice in the Moon's south polar regions from Lunar Reconnaissance Orbiter ultraviolet albedo and temperature measurements. *Icarus*, 255, 58–69.

Hendrix, A. R., Hurley, D. M., Farrell, W. M., Greenhagen, B. T., Hayne, P. O., Retherford, K. D., et al. (2019). Diurnally Migrating Lunar Water: Evidence From Ultraviolet Data. *Geophysical Research Letters*, 46(5), 2417–2424.

Hendrix, A. R., Retherford, K. D., Gladstone, G. R., Hurley, D. M., Feldman, P. D., Egan, A. F., et al. (2012). The lunar far-UV albedo: Indicator of hydration and weathering. J*ournal of Geophysical Research: Planets*, 117(E12).

Herter, T. L. *et al.* (2013). Data reduction and early science calibration for FORCAST, a mid-infrared camera for SOFIA. *Publications of the Astronomical Society of the Pacific*, *125*, 1393–1404.

Herter, T. L., Adams, J. D., Gull, G. E., Schoenwald, J., Keller, L. D., Pirger, B. E., et al. (2018). FORCAST: A Mid-Infrared Camera for SOFIA. *Journal of Astronomical Instrumentation*, 7, 1–13.

Hibbitts, C. A., G. A. Grieves, M. J. Poston, M. D. Dyar, A. B. Alexandrov, M. A. Johnson, and T. M. Orlando. (2011). Thermal stability of water and hydroxyl on the surface of the Moon from temperature-programmed desorption measurements of lunar analog materials, *Icarus*, *213*(1), 64-72.

Honniball, C. I., Wright, R., and Lucey, P. G. (2017). Spectral response of microbolometers for hyperspectral imaging. MS Thesis, University of Hawaii.

Horton, R.F., (1996). Optical design for a high Etendue imaging Fourier transform spectrometer. in Proc. SPIE 2819, 300–315.

Housley, R.M.. Cirlin, E.H., Paton, N.E., and Goldberg, I.B. (1974). Solar wind and micrometeorite alteration of the lunar regolith. *In Lunar and Planetary Science Conference Proceedings,* 5, 2623-2642.

Howell, R. R. (1997). Thermal Emission from Lava Flows on Io. *Icarus*, *127*, 394–407.

ASTM E490-00a(2014), Standard Solar Constant and Zero Air Mass Solar Spectral Irradiance Tables, ASTM International, West Conshohocken, PA, 2014, www.astm.org

Hurley, D. M., Sarantos, M., Grava, C., Williams, J.-P., Retherford, K. D., Siegler, M., et al. (2015). An analytic function of lunar surface temperature for exospheric modeling. *Icarus*, 255, 159–163. http://doi.org/10.1016/j.icarus.2014.08.043

Ichimura, A. S., Zent, A. P., Quinn, R. C., Sanchez, M. R., & Taylor, L. A. (2012). Hydroxyl (OH) production on airless planetary bodies: Evidence from H+/D+ ion-beam experiments. *Earth and Planetary Science Letters,* 345-348, 90–94.

Jones, B. M., Aleksandrov, A., Hibbitts, K., Dyar, M. D., & Orlando, T. M. (2018). Solar Wind-Induced Water Cycle on the Moon. *Geophysical Research Letters*, 45(20), 10,959–10,967.

Khayat, A. SJ., Villanueva, G. L., Mumma, M. J., and Tokunaga, A. T. (2017). A deep search for the release of volcanic gases on Mars using ground-based high-resolution infrared and submillimeter spectroscopy: Sensitive upper limits for OCS and SO_2. *Icarus*, 296: 1-14.

Khayat, A. SJ., Villanueva, G., Mumma, M., and Tokunaga, A. (2015). A search for SO_2, H_2S and SO above Tharsis and Syrtis volcanic districts on Mars using ground-based high-resolution submillimeter spectroscopy. *Icarus*, 253: 130-141.

King, P. L., McMillan, P. F., and Moore, G. M. (2004). Chapter 4. Infrared Spectroscopy Of Silicate Glasses With Application To Natural Systems. *Mineralogical Association of Canada*, 93–134.

Kruse, P.W. (2002). Uncooled Thermal Imaging, Vol. TT51 of Tutorial Texts in Optical Engineering, A. R. Weeks.

Kumar, K. A., Thapa, N., & Kuriakose, S. A. (2015). Advances in spaceborne hyperspectral imaging systems, *Current Science*, *108*(5), 826–832.

Lawrence, D. J., Feldman, W. C., Goldsten, J. O., Maurice, S., Peplowski, P. N., Anderson, B. J., et al. (2012). Evidence for Water Ice Near Mercury's North Pole from MESSENGER Neutron Spectrometer Measurements. *Science*, 1-6. http://doi.org/10.1126/science.1229953

Lawson, S. L., & Jakosky, B. M. (1999). Brightness temperatures of the lunar surface: the clementine long-wave infrared global data set. *Lunar and Planetary Science abstract*, XXX, 1–2.

Lebofsky, L. A. (1978). Asteroid 1 Ceres: evidence for water of hydration. Mon. Not. R. Astr. Soc., 182, 17–21.

Li S., Lucey, P.G., Sun., V.Z., Fraeman, A.A. (2019). Detection of a 850 nm absorption feature at high latitudes on the moon: possible presence of hematite**.** *Lunar and Planetary Science abstract*, 2320.

Li, S. (2017). Water on the Lunar Surface as Seen by the Moon Mineralogy Mapper: Distribution, Abundance, and Origins. *Brown University,* PhD Dissertation (pp. 1–311).

Li, S. & Milliken, R. E. (2017). Water on the surface of the Moon as seen by the Moon Mineralogy Mapper: Distribution, abundance, and origins. *Science Advances*, 3(9), e1701471.

Liu, Y., Guan, Y., Zhang, Y., Rossman, G. R., Eiler, J. M., & Taylor, L. A. (2012). Direct measurement of hydroxyl in the lunar regolith and the origin of lunar surface water. *Nature Geoscience,* 5(11), 779.

Lord, S. D., 1992, NASA Technical Memorandum 103957

Lucey, P. G., & Wilcox, B. B. (2003). Mini-SMIFTS: an uncooled LWIR hyperspectral sensor. In S. S. Shen & P. E. Lewis (Eds.), (Vol. 5159, pp. 275–8). Presented at the Optical Science and Technology, SPIE's 48th Annual Meeting, SPIE.

Lucey, P. G., Hinrichs, J. L., & Akagi, J. (2012). A compact LWIR hyperspectral system employing a microbolometer array and a variable gap Fabry-Perot interferometer employed as a Fourier transform spectrometer. In S. S. Shen & P. E. Lewis (Eds.), (pp. 83900R–83900R–8). Presented at the SPIE Defense, Security, and Sensing, SPIE.

Lucey, P. G., Horton, K. A., & Williams, T. (2008). Performance of a long-wave infrared hyperspectral imager using a Sagnac interferometer and an uncooled microbolometer array. *Applied Optics*, *47*, 107–113.

Lucey, P. G., Horton, K. A., Williams, T. J., Hinck, K., Budney, C., Rafert, B., & Rusk, T. B. (1993). SMIFTS: a cryogenically cooled, spatially modulated imaging infrared interferometer spectrometer, *1937*, 130–142.

Makki, I., Younes, R., Francis, C., Bianchi, T., & Zucchetti, M. (2017). A survey of landmine detection using hyperspectral imaging. *ISPRS Journal of Photogrammetry and Remote Sensing*, *124*, 40–53.

Marchis, F., Enriquez, J. E., Emery, J. P., Mueller, M., Baek, M., Pollock, J., et al. (2012). Multiple asteroid systems: Dimensions and thermal properties from Spitzer Space Telescope and ground-based observations. *Icarus*, 221(2), 1130–1161.

Mattern, P.L., Thomas, G.J., Bauer, W., 1976. Hydrogen and helium implantation in vitreous silica. J. Vac. Sci. Technol. 13 (1), 430–436.

McClanahan, T. P., Mitrofanov, I. G., Boynton, W. V., Chin, G., Parsons, A., Starr, R. D., et al.(2014). Epithermal Neutron Evidence for a Diurnal Surface Hydration Process in the Moon's High Latitudes.

McCord, T. B., Taylor, L. A., Combe, J. P., Kramer, G., Pieters, C. M., Sunshine, J. M., & Clark, R. N. (2011). Sources and physical processes responsible for OH/H2O in the lunar soil as revealed by the Moon Mineralogy Mapper (M3). *Journal of Geophysical Research: Planets*, *116*, 1–22.

McIntosh, I. M., Nichols, A. R. L., Tani, K., and Llewellin, E. W. (2017). Accounting for the species-dependence of the 3500 cm^{-1} H_2O infrared molar absorptivity coefficient: Implications for hydrated volcanic glasses. *American Mineralogist*, 102, 8, 1677–1689.

McKay D.S., Heiken, G., Basu, A., Blanford, G., Simon, S., Reedy, R., French, B.M., and Papike, J. (1991) The Lunar Regolith, in The Lunar Sourcebook, Heiken G. H, Vaniman D. T. and French B. M., eds. Cambridge University Press, New York NY, 285-356.

Minnett, P. J. , and Sellar, R. G. (2005). The High Efficiency Hyperspectral Imager—a new instrument for measurements of the Arctic surface. presented at the Eighth Conference on Polar Meteorology and Oceanography, American Meteorological Society, poster presentation P1.3, 11.

Mitchell, J., W. Houston, R. Scott, N. Costes, W. Carrier III, and L. Bromwell. (1972). Mechanical properties of lunar soil: Density, porosity, cohesion and angle of internal friction, *Lunar and Planetary Science Conference Proceedings*.

Mori, T., Hashimoto, T., Terada, A., Yoshimoto, M., Kazahaya, R., Shinohara, H., & Tanaka, R. (2016). Volcanic plume measurements using a UAV for the 2014 Mt. Ontake eruption. *Earth, Planets and Space*, *68*(1), 1–18.

Newman, S., Stolper, E. M., & Epstein, S. (1986). Measurement of water in rhyolitic glasses; calibration of an infrared spectroscopic technique. *American Mineralogist*, 71, 1527–1541.

Nozette, S., Lichtenberg, C. L., Spudis, P., Bonner, R., Ort, W., Malaret, E., et al. (1996). The Clementine Bistatic Radar Experiment. *Science*, 274(5292), 1495–1498.

Okamoto, T., Kawata, S., & Minami, S. (1984). Fourier transform spectrometer with a self-scanning photodiode array. *Applied Optics*, *23*(2), 269–273.

Patrick, M. R., Orr, T., Sutton, A. J., Lev, E., Thelen, W., & Fee, D. (2016). Shallowly driven fluctuations in lava lake outgassing (gas pistoning), Kīlauea Volcano. *Earth and Planetary Science Letters*, *433*, 326–338.

Peale, S. J., Cassen, P., & Reynolds, R. T. (2008). Melting of Io by Tidal Dissipation. *Science*, *203*, 892–894.

Pettit, E., and Nicholson, S. B. (1930). Lunar radiation and temperatures. *American Astronomical Society*, 102–135.

Pieters, C. M., Goswami, J. N., Clark, R. N., Annadurai, M., Boardman, J., Buratti, B., et al. (2009). Character and Spatial Distribution of OH/H2O on the Surface of the Moon Seen by M3 on Chandrayaan-1. *Science*, 326(5952), 568–572.

Pignatti, S., Lapenna, V., Palombo, A., Pascucci, S., Pergola, N., & Cuomo, V. (n.d.). An advanced tool of the CNR IMAA EO facilities: Overview of the TASI-600 hyperspectral thermal spectrometer (pp. 1–4). Presented at the 2011 3rd Workshop on Hyperspectral Image and Signal Processing: Evolution in Remote Sensing (WHISPERS), IEEE.

Poston, M. J., Grieves, G. A., Aleksandrov, A. B., Hibbitts, C. A., Dyar, M. D., & Orlando, T. M. (2015). Temperature programmed desorption studies of water interactions with Apollo lunar samples 12001 and 72501. *Icarus*, 255, 24–29.

Prettyman, T. H., Yamashita, N., Toplis, M. J., McSween, H. Y., Schörghofer, N., Marchi, S., et al. (2017). Extensive water ice within Ceres' aqueously altered regolith: Evidence from nuclear spectroscopy. *Science*, 355(6320), 55–59.

Rafert, B., Sellar, R. G., Holbert, E., Blatt, J. H., Tyler, D. W., Durham, S. E., and Newby, H. D. (1994). Hyperspectral imaging Fourier transform spectrometers for astronomical and remote sensing observations. Proc. SPIE 2198, 338–349.

Rayner, J. T., Cushing, M. C., and Vacca, W. D. (2009). The Infrared Telescope Facility (Irtf) Spectral Library: Cool Stars. *The Astrophysical Journal Supplement Series*, 185(2), 289–432.

Rayner, J. T., Toomey, D. W., Onaka, P. M., Denault, A. J., Stahlberger, W. E., Watanabe, D. Y., & Wang, S.-I. (1998). SpeX: a medium-resolution IR spectrograph for IRTF. In Infrared Astronomical Instrumentation (Vol. 3354, pp. 468–480). International Society for Optics and Photonics.

Reddy, V., Emery, J.P., Gaffey, M.J., Bottke, W.F., Cramer, A., Kelley, M.S., 2009. Composition of 298 Baptistina: Implications for the K/T impactor link. *Meteor. Planet. Sci.* 44, 1917–1927.

Rinker, J. N. (1990). Hyperspectral Imagery: A New Technique for Targeting and Intelligence. *U.S. Army Topographic Engineering Center*, 1–16.

Rivkin, A., Binzel, R., and Bus, S. (2005). Constraining near-Earth object albedos using near-infrared spectroscopy. Icarus, 175(1), 175–180.

Robens, E., Bischoff, A., Schreiber, A., Dąbrowski, A., & Unger, K. K. (2007). Investigation of surface properties of lunar regolith: Part I. *Applied Surface Science*, *253*(13), 5709–5714.

Rogalski, A. (2002). Infrared detectors: an overview. *Infrared Physics & Technology*, *43*(3-5), 187–210. http://doi.org/10.1016/S1350-4495(02)00140-8

Rogalski, A. (2017). Next decade in infrared detectors. *Electro- Optical and Infrared Systems Technology and Applications XIV*, *10433*, 104330L.

Rothman et al., (2013). The HITRAN2012 molecular spectroscopic database. *Journal of Quantitative Spectroscopy and Radiative Transfer*, 130, 4–50.

Schörghofer, N. (2014). Migration calculations for water in the exosphere of the Moon: Duskdawn asymmetry, heterogeneous trapping, and D/H fractionation. *Geophysical Research Letters*, 41, 1–6.

Schott, J. R. (2007). Remote Sensing: The Image Chain Approach. Oxford University Press.

Sellar and Boreman, G. D. (2003). Limiting aspect ratios of Sagnac interferometers. Opt. Eng, 42, 3320–3325.

Shukla, A., & Kot, R. (2016). An Overview of Hyperspectral Remote Sensing and its applications in various Disciplines. *International Journal of Applied Sciences*, *5*(2), 85–90.

Siskind, B., Gruen, D.M., Varma, R. (1977). Chemical implantation of 10-keV Hþ and Dþ in rutile. *J. Vac. Sci. Technol.* 14, 537–542.

Smith W.H and Hammer, P.D. (1996). Digital array scanned interferometer: Sensor and Results, Applied Optics 35(16), 2902-2909.

Smith,W.H., and Schemp, W.V. (1991). Digital aray scaned interferometers for astronomy, Exp.Astron.1, 389-405.

Spampinato, L., Oppenheimer, C., Calvari, S., Cannata, A., and Montalto, P. (2008). Lava lake surface characterization by thermal imaging: Erta 'Ale volcano (Ethiopia). *Geochemistry, Geophysics, Geosystems*, 9(12), 326-338.

Starukhina, L. (2001). Water detection on atmosphereless celestial bodies: Alternative explanations of the observations. Journal of Geophysical Research, 106, 701–710.

Starukhina, L. V. (2006). Polar regions of the moon as a potential repository of solar-wind-implanted gases. *Advances in Space Research*, 37(1), 50–58.

Stolper, E. (1982). Water in silicate glasses: An infrared spectroscopic study. *Contributions to Mineralogy and Petrology*, 81, 1–17.

Sunshine, J. M., Farnham, T. L., Feaga, L. M., Groussin, O., Merlin, F., Milliken, R. E., & A'Hearn, M. F. (2009). Temporal and Spatial Variability of Lunar Hydration As Observed by the Deep Impact Spacecraft. *Science*, 326(5952), 565–568.

Sutton, A. J., & Elias, T. (2014). One hundred volatile years of volcanic gas studies at the Hawaiian Volcano Observatory: Chapter 7 in Characteristics of Hawaiian volcanoes (pp. 295–320). Professional Paper.

Takir, D., & Emery, J. P. (2012). Outer Main Belt asteroids: Identification and distribution of four 3-μm spectral groups. Icarus, 219(2), 641–654.

Takir, D., Stockstill-Cahill, K. R., Hibbitts, C. A., & Nakauchi, Y. (2019). 3-μm reflectance spectroscopy of carbonaceous chondrites under asteroid-like conditions. *Icarus*, 333, 243–251.

Thompson, W. K. (1965). Infra-red spectroscopic studies of aqueous systems. Part 1.—Molar extinction coefficients of water, deuterium oxide, deuterium hydrogen oxide, aqueous sodium chloride and carbon disulphide. *Transactions of the Faraday Society*, 61(0), 2635–2640.

Thorpe, A. K., Roberts, D. A., Bradley, E. S., Funk, C. C., Dennison, P. E., & Leifer, I. (2013). High resolution mapping of methane emissions from marine and terrestrial sources using a Cluster-Tuned Matched Filter technique and imaging spectrometry. *Remote Sensing of Environment*, *134*(C), 305–318.

Tucker, O. J., Farrell, W. M., Killen, R. M., & Hurley, D. M. (2019). Solar Wind Implantation Into the Lunar Regolith: Monte Carlo Simulations of H Retention in a Surface With Defects and the H2 Exosphere. *Journal of Geophysical Research: Planets*, 124(2), 278–293.

van der Meer, F. D., van der Werff, H. M. A., van Ruitenbeek, F. J. A., Hecker, C. A., Bakker, W. H., Noomen, M. F., et al. (2012). Multi- and hyperspectral geologic remote sensing: A review. *International Journal of Applied Earth Observation and Geoinformation*, *14*(1), 112–128.

Vaughan, G., Calvin, W., Taranik. (2003). SEBASS hyperspectral thermal infrared data: surface emissivity measurement and mineral mapping. *Remote Sensing of Environment*, *85*(1), 48–63.

Watson, K., B. C. Murray, and H. Brown (1961), The behavior of volatiles on the lunar surface, *Journal of Geophysical Research*, *66*(9), 3033-3045.

Werner, C., Evans, W. C., Kelly, P. J., McGimsey, R., Pfeffer, M., Doukas, M., & Neal, C. (2012). Deep magmatic degassing versus scrubbing: Elevated CO 2emissions and C/S in the lead-up to the 2009 eruption of Redoubt Volcano, Alaska. *Geochemistry, Geophysics, Geosystems*, *13*(3), n/a–n/a.

Wöhler, C., Grumpe, A., Berezhnoy, A. A., & Shevchenko, V. V. (2017). Time-of-day–dependent global distribution of lunar surficial water/hydroxyl. *Science Advances*, 3(9).

Wooster, M. J. (2002). Small-scale experimental testing of fire radiative energy for quantifying mass combusted in natural vegetation fires. *Geophysical Research Letters*, *29*(21), 5–4.

Wright, R., Lucey, P., Crites, S., Garbeil, H., Wood, M., Pilger, E., et al. (2016). TIRCIS: thermal infrared compact imaging spectrometer for small satellite applications, (012506), 100000M.

Zeller, E. J., & Ronca, L. B. (1967). Space weathering of lunar and asteroidal surfaces. *Icarus*, 7(1-3), 372–379.

Zeller, E.J., Ronca, L.B., Levy, P.W. (1966). Proton-induced hydroxyl formation on the lunar surface. *J. Geophys. Res.* 71, 4855–4860.

Zhu C, Crandall P. B., Gillis-Davis J. .J., Ishii H. A., Bradley J. P., Corley L. M., Kaiser R. I., (2019), Untangling the formation and liberation of water in the lunar regolith. *Proceedings of the National Academy of Sciences.* 116(23), 11165-70.